Ion Transport in Semicrystalline Solid Polymer Electrolytes

A Thesis

Submitted to the Faculty

of

Drexel University

By

Shan Cheng

in partial fulfillment of the

requirements for the degree

of

Doctor of Philosophy

August 2014

Dedications

To my dear parents Jun Cheng and Zhaoming Luo

My husband Sen Xu

Acknowledgements

I would like to thank my advisor, Dr. Christopher Y. Li for offering me the opportunity to work in the Soft Materials Lab and guiding me through this long journey. I'm always impressed and motivated by his knowledge, creativity and critical thinking to the research field. It's his enthusiasm and dedication that drive me to make continuous progress. I also would like to thank my co-advisor, Dr. Grace Y. Hsuan for the kind support during the first three years in not only the cross-discipline project but also many other activities. Thanks to Dr. Caroline Schauer, Dr. Kenneth Lau and Dr. Stephanie Wunder for serving as my thesis committee members. The dissertation would not be completed without their valuable advice.

I would like to extend my thanks to all my colleagues in the Soft Materials Lab at Drexel University: Dr. Bin Dong for sharing me with his research experiences and helping me with all the lab work; Dr. Eric Laird, Dr. Xi Chen and Frida Qi for helping me with the SEM measurements; Wenda Wang and Tian Zhou for helping me with the TEM measurements. Special thank to Derrick Smith for making the sandwich electrode and 4-parallel-electrode cells for EIS measurement and setting up the glovebox and for many useful discussions and suggestions. I wouldn't complete this project without his help. And thanks to all the past and current group members for their kind help during the past five years. Moreover, I would like to thank Dr. Volker Presser for training me the 2D SAXS/WAXD instrument and his patience in the trouble shooting with me. Thanks Dr. Craig Johnson for the TEM measurement during my first two years and Dr. Edward Basgall for helping me with the ultra microtome.

In addition, I would like to thank my manager Max (Xiao) Mo at BD who helped me go through the transition from academia to industry and I'm grateful for his full support on my dissertation writing.

Last but not least, I would like to express my big "thank you" to my dear parents for their unconditional love and encouragement over years. And specially thank to my husband Sen Xu for his sacrifice and dedications.

Table of Contents

LIST OF TABLES

LIST OF FIGURES

LIST OF EQUATIONS

ABSTRACT
Ion Transport in Semicrystalline Solid Polymer Electrolytes
Shan Cheng
Advisor: Christopher Y. Li, Ph.D.

Solid polymer electrolytes (SPEs) with both high room temperature ionic conductivity and mechanical integrity are highly desirable for all-solid-state lithium batteries. Linear polyethylene oxide (PEO) represents the simplest yet most attractive solvating polymer due to its capability to form complex with a selected number of alkali metal salt, especially lithium salt. The ether oxygen on PEO backbone coordinates with Li^+ and the transport of the latter is facilitated through segmental motion of the polymer chain. However, the highly crystalline nature due to stereoregularity and flexibility of the polymer chain complicate the ion transport mechanism. PEO crystallization has been long considered to be detrimental to ion transport as it results in a decrease of the effective fraction of amorphous conducting phase, slower polymer chain dynamics and more tortuous pathways for ion transport. However, a quantitative analysis of crystallization effect on the ionic conductivity is challenging since these factors are always coupled.

In this dissertation, we demonstrated that the two factors, namely tethered chain/dynamic and tortuosity/structural effects can be decoupled by preparing polymer membranes with controlled crystal orientation and measuring the in-plane and through-plane conductivity of the orientated membrane. Moderate conductivity anisotropy as a result of PEO lamellar orientation was first observed in a solution cast PEO SPE. We

further used graphene oxide to enhance the crystal orientation, hence the conductivity anisotropy.

To quantitatively characterize the crystallization effect, a model electrolyte system consists of PEO single crystals with well controlled crystal structure, size, crystallinity and orientation were fabricated. Ion conduction was confined within the chain fold region, and guided by the crystalline lamellae. We demonstrated that at low ion content, the in-plane conductivity was 1000-2000 times greater than through-plane one due to the tortuosity effect, which was described using Nielsen's permeability model. Contradictory to the general view, the dynamic effect was negligible at moderate ion contents and the overall conductivity was mainly controlled by crystal orientation, strong Li–PEO interaction and Li^+ aggregation. Our results demonstrated that semicrystalline polymer can be viewed as a two phase model which morphologically mimicking the popular systems such as block copolymers and polyolefin porous membranes. By controlling crystallization behavior, mechanically robust semi-crystalline SPE with high room temperature conductivity is feasible.

CHAPTER 1: **INTRODUCTION**

1.1 Background/ Motivations

Modern development of batteries has been greatly accelerated by the demand from multiple factors/industries. One big drive is from the practical requirement in the exponential growing electronics industry (e.g., personal computers, portable electronics, and telecommunications, etc.), in which compact and light-weight power source is a necessity for performance. In addition, the rapid consumption of finite fossil fuel (one of the biggest consumptions is from the internal combustion engine vehicles) and concerns on carbon dioxide emissions lead to a global desire for more sustainable and efficient energy sources. Adaptation of (hybrid) electric vehicles has been greatly advocated and it is another motivation of developing safe and high performance batteries.

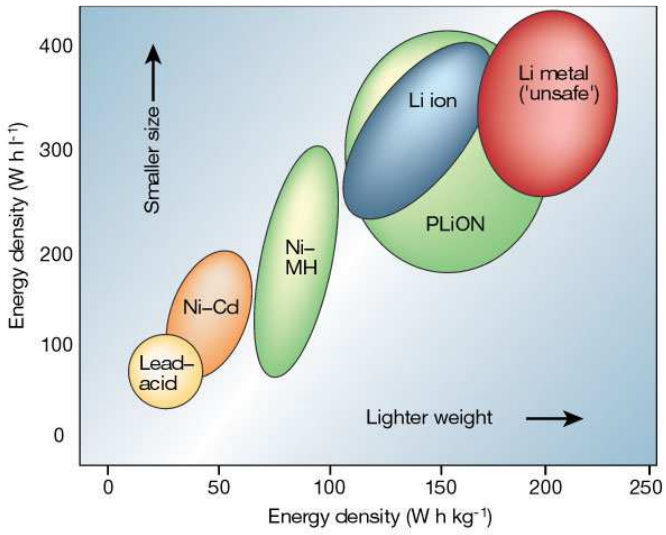

Figure 1.1 Comparison of volumetric and gravimetric energy density of different battery technologies, plot reproduced from ref. [1]

Lithium batteries stand out among all battery technologies simply because of the fact that lithium is the lightest metal (density of 0.534 g/cm^3) and exhibits the highest oxidation potential (-3.04 V relative to standard H electrode), which results in high volumetric and gravimetric energy density as shown in Figure 1.1. A typical battery consists of an anode and a cathode that are separated by an ionic conductive electrolyte material (Figure 1.2). The charge and discharge process of the battery involves electron flow through an external circuit and the lithium ion migration between anode and cathode through an electrolyte media. The overall performance of the battery strongly depends on the structure and chemistry of the system. While cathode and anode materials determine the cell potential and the capacity of the batteries, appropriate electrolytes are crucial to the current density, cyclability and more importantly, safety of the batteries.

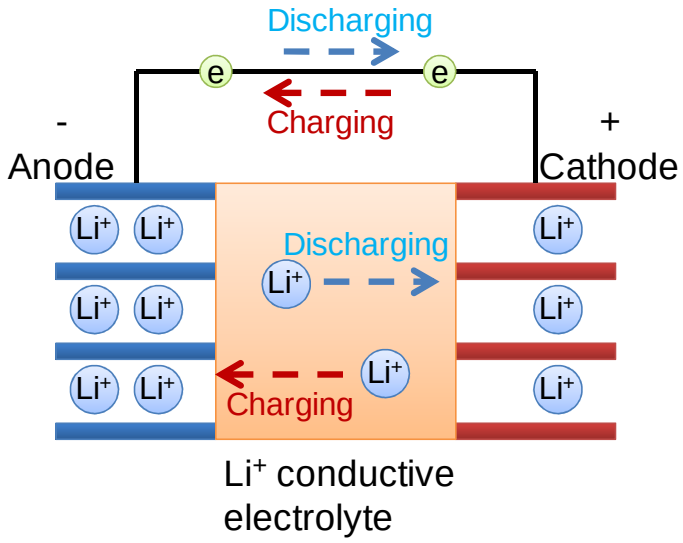

Figure 1.2 Schematics of a rechargeable Li-ion battery.

Li metal is the most promising candidate as anode material to yield a high energy density of the battery, particularly if appropriate cathode material is chosen to increase the cell voltage to 4 volts or more. However, the major issue for lithium-metal system is the Li dendrite formation at the anode surface after several charge-discharge cycles, which leads to serious safety hazard[1-2]. One approach to mitigate this problem is to replace the liquid electrolyte with a mechanically strong dry polymer electrolyte, although it is at the expense of ionic conductivity decrease, which limits the Li-metal/polymer battery from practical applications[1, 3] .

The development of so-called “rocking chair” or Li-ion technology is another solution to address the safety issue of the Li-metal battery[1, 3-6]. In this case, Li dendrite growth can be circumvented by substituting the negative Li metal electrode with an intercalated compound. In order to achieve the same level of potential difference as in the Li-metal system, new cathode materials with higher oxidation potential are required in order to compensate the increasing potential of the negative inserted compound electrode as illustrated in Figure 1.3. The upper shift of the operating voltage may cause decomposition of the current liquid electrolyte and therefore an electrolyte with a wider electrochemical window is recommended.

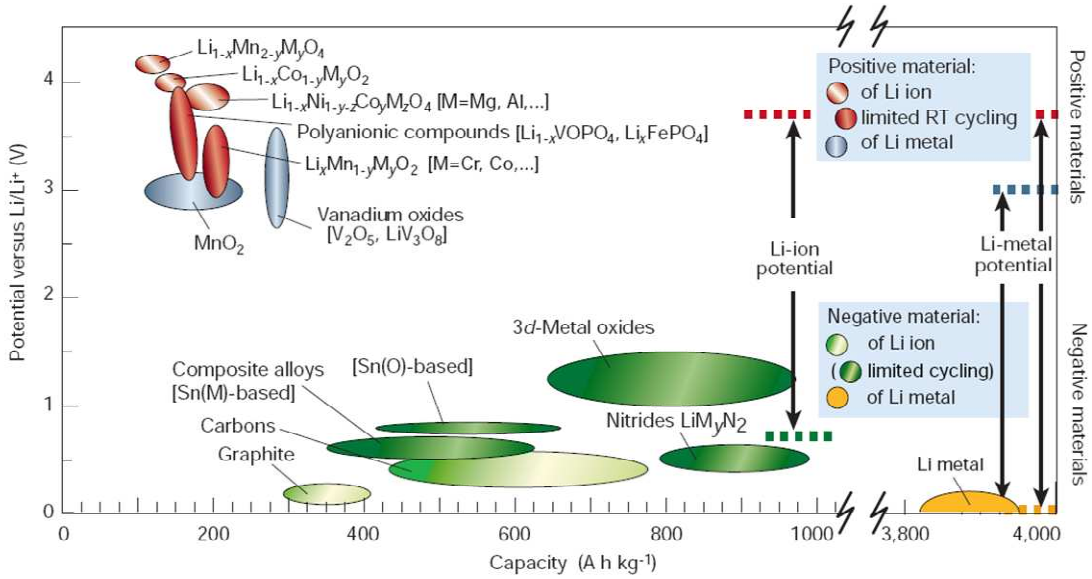

Figure 1.3 Potential versus capacity for a series of positive and negative electrode candidates for rechargeable Li batteries, reproduced from ref. [1].

In both Li-metal and Li-ion systems, replacing the volatile, flammable liquid organic electrolyte with solid polymer electrolytes (SPEs) having adequate ionic conductivity, high cation mobility, sufficient mechanical properties and wide electrochemical window is critical to addressing the safety concerns without sacrificing the life cycle and power density of the batteries. PEO with a glass transition temperature well below zero (around -60°C) has been demonstrated as a strong candidate as a solid polymer electrolyte due to its high dielectric constant and strong lithium ion solvating ability[7-11]. The ion conduction mechanism is considered as the ion hopping along the polymer chain assisted by the ether oxygen and in most of the cases it takes place in the amorphous region along with the long range segmental motion of the polymer chain. However, linear PEO homopolymer tends to crystallize with 60-70% crystallinity due to

the regularity of the backbone and the ionic conductivity of the SPEs at room temperature is far below the required value (>10^{-4} S/cm) in battery applications.

The general rule of SPE design is to suppress PEO crystallinity in order to maximize the mobile phase for ion conduction. Such strategies include grafting short PEO oligomers onto polymer backbones, or cross linking PEO-based polymers[12-14]. However, increasing the amorphous PEO fraction would inevitably compromise mechanical strength of the SPE. This problem can be mitigated by decoupling ion conduction and mechanical properties in the materials design. Early attempts had been made by blending high molecular weight PEO with polymers having a high glass transition temperature, such as polystyrene[15], poly(methyl methacrylates) [16-19], polyacryloamides[20-21] and so on. Although the introduction of these rigid phases improved the mechanical performances of the electrolyte, the morphologies of these blend systems were very difficult to control and the continuity of ion conducting pathways were strongly affected by the materials preparation techniques[15].

In contrary, PEO based block-copolymer (BCP) electrolytes appear to be more advantageous over blends system in terms of morphology control[22-46]. The hard non-conducting segment and flexible conducting segment are covalently bonded and phase separated into nanoscale domains. The structure can be readily tuned from cylinder, gyroid or lamellae by varying the molecular weight of each block. Extensive efforts have been made to understand the salt doping effect on the phase behavior of the BCPs and its impact on the ionic conductivity and mechanical properties of the SPEs. Although significant improvements have been achieved on the thermal, mechanical and

electrochemical stability, most of the current BCP SPEs suffer from low room temperature ionic conductivities.

Another solution to enhance both conductivity and mechanical property is based on PEO-ceramic nanocomposites. Ceramic nanoparticles such as TiO_2, SiO_2 and Al_2O_3 with large surface area and Lewis acid characteristic have been demonstrated to retard PEO recrystallization, create specific conducting pathways along PEO-ceramic interface and enhance the lithium interfacial stability while the high modulus of the nanoparticles compensated for the mechanical strength loss due to the decrease of crystallinity[4, 11, 47-48]. The ionic conductivity at ambient temperature stayed stable within the time frame of the test (several days) yet evaluation of the long-term stability of these amorphous structures had not been reported[48-50]. The specific role of ceramic fillers is still under debate since contradictory results had been found elsewhere[51-55]. Recent years a few other studies had been focused on polymer/CNT or polymer/clay nanocomposites, but only moderate improvement has been reported so far[56-58].

Despite the direct linkage between ion conduction and polymer dynamics had been highly appreciated and it has been widely accepted that cation transport is confined only in the amorphous PEO/lithium phase, there are still a few limited studied highlighted the merits of crystallization. Bruce *et al.* first reported that certain 6:1 crystalline complexes (for example, $P(EO)_6$:$LiAsF_6$) can offer even greater ion conductivity than its amorphous equivalence in the late 1990s[59-61], which was some twenty years later since crystalline polymer electrolyte had been treated as insulators. More recently, Fullerton-Shirey *et al.* observed the highest conductivity in PEO/$LiClO_4$ blend electrolytes at a

moderate crystallinity instead of completely amorphous state; and speculated that PEO crystallization might have some templating effect that promoted the ion transport[62]. However, no detailed explanation had been further explored.

In general, to obtain a comprehensive understanding of the crystallization effect on ion conduction is challenging. The multiple-phase morphologies are typically too complicated for conducting a quantitative analysis to correlate structure and ion transport in semicrystalline SPEs due to the ambiguities introduced by the salt concentration, anions, and thermal history[62-67]. Since semicrystalline polymers provide the much needed mechanical properties for device applications, if the ion conduction can be better understood and controlled, it would offer an alternative solution to develop high performance SPEs that competes with the most popularly studied BCP and nanocomposite SPEs.

1.2 Objectives

The objective of the dissertation study is to have an in-depth understanding on the fundamentals of ion conduction in semicrystalline PEO based SPEs, and this understanding would provide insights in the design and development of high performance polymer electrolytes for energy related applications.

1.3 Contributions

This thesis is divided into 9 chapters. Chapter 1 describes the general background, motivation and objective of this research. Chapter 2 gives a detailed literature review on the history, ion conduction mechanism and state-of-art development of SPEs. Chapter 3

discusses all the materials and methods, characterization techniques, and experimental setups employed in this dissertation study. Chapters 4 to 8 cover detailed results and discussions on the three above-mentioned semicrystalline SPE systems. Chapter 9 includes conclusion of the outcomes from this dissertation and recommendations for future work.

The main contributions of this thesis include:

- Identified that PEO crystal orientation was a critical factor for ion conduction using a solution cast PEO/$LiClO_4$ SPE prepared by slow solvent evaporation. Correlation between PEO crystal alignment and the ionic conductivity anisotropy had been established. Detailed morphology characterization and electrochemical impedance measurements will be described in Chapter 4.
- Developed a graphene oxide-PEO nanocomposite SPE system to further tune the ion conduction pathways and the conductivity anisotropy was improved. The structure, crystallization behavior and ion conduction of the nanocomposite SPE were thoroughly studied and will be discussed in Chapter 5.
- Designed a unique SPE consists of PEO single crystals with precisely controlled size, thickness and orientation as a model electrolyte system. Two prototype lithium salts: $LiClO_4$ and LiTFSI were selected and the anion effects on the structure and ionic conductivities of the polymer single crystal SPEs were compared. The structural analysis and ion conduction behavior of the single cystal-$LiClO_4$ SPEs will be described in Chapter 6 and the LiTFSI system will be discussed in Chapter 7.

- The two critical factors that strongly affect ion conductivity: namely tortuosity and dynamic effect were completely decoupled and quantified using these PEO single crystal model SPEs. The ion conducting mechanism was quantitatively explained using both permeability model and molecular structure model and a generic ionic conductivity expression for semicrystalline SPE with well-defined structures had been proposed at the end in Chapter 8.

Related publications include:

1. Cheng, S.; Smith, D. M.; Li, C. Y., How Does Nanoscale Crystalline Structure Affect Ion Transport in Solid Polymer Electrolytes? *Macromolecules* **2014,** *47* (12), 3978-3986.
2. Cheng, S.; Smith, D. M.; Li, C. Y., Enhanced ion transport in a PEO single crystal model electrolyte containing LiTFSI. *In preparation*
3. Cheng, S.; Smith, D. M.; Li, C. Y., Conductivity anisotropy in a graphene oxide/polyethylene oxide nanocomposite electrolyte. *In preparation*

CHAPTER 2: **AN OVERVIEW OF SOLID POLYMER ELECTROLYTES**

2.1 History of solid polymer electrolytes

The development of solid polymer electrolytes (SPEs) has experienced four stages. The 1970s was marked as "a period of significant change". The discovery of SPEs was facilitated by the significant progress in polymer science. Shortly after Wright *et al.* reported the semicrystalline structure of complexes between PEO and alkali salts in 1973[68] and the following study on its electrical properties[69-70], Armand proposed to use these polymer-alkali salt complexes as solid electrolyte for the high-energy-density battery application since they combined solid-state electrochemistry and the advantage of flexible, easy processing nature of plastics[71]. Interests in this emerging area started to span worldwide since then. Early investigations focused on understanding the correlation between morphology and conductivity of these complexes. It was initially speculated that ion transport through the polymer helices in the crystalline phase, similar to inorganic ion conductors. However, it was soon demonstrated that only the amorphous phase accounts for ion conduction[72-75].

The linkage between polymer segmental dynamics and ion transport in early 1980s largely determined the direction of SPE development during the second decade. Tremendous efforts were devoted to inhibiting polymer crystallization in SPEs. The strategies that have been developed include modification of the polymer structure with different architectures, such as comb-like type with short PEO chain and cross-linked network polymers[12-14, 76]. However, the major issue with these approaches is that

reducing the crystallinity of the polymer would inevitably sacrifice the mechanical integrity, which contradicts the original intention of using mechanically robust polymer membranes for safer battery applications. To find a balance between fast ion transport and high mechanical property, several approaches were developed during the middle to late 1980s, including polymer blends SPEs, block copolymer SPEs and ceramic reinforced SPEs[47, 77]. Development of single ion conductors started in the middle of 1980s in recognisation of the importance of high cation transference number for the battery performance. Progress had been made in understanding of the SPE structure: Crystallographic structure of a PEO:NaI 3:1 crystalline complex was fully determined using X-ray diffraction method for the first time by Chatani *et al.* in 1987[78]. Meanwhile, several theoretical models had been developed in this period to describe the ion transport properties in SPEs[79-85]. Significant contributions had been made during the second decade as clearly suggested by the exponential growth of publications in Figure 2.1.

Development of "classic" PEO-based SPEs continued in the 1990s with efforts on decoupling ion transport from the mechanical support and increasing the charge carrier density. Besides the conventional SPE systems such as amorphous SPE, multiphase SPE and single ion conductors, Angell *et al.* showed the advantage of using a novel "polymer-in-salt" electrolyte with superior performance[86].

Lastly, great innovations and breakthroughs have been witnessed during the last decade. A class of nanocomposite SPEs developed by Scrosati *et al.* appears to be promising candidates for high performance lithium battery applications due to their enhanced mechanical, thermal, and electrochemical stability, as well as room temperature

conductivity[48-49, 87]. The discovery of fast ion transport in some $P(EO)_6LiX$ crystalline complexes by Bruce *et al.* has led to a reconsideration of the fundamental ion conduction mechanism in polymer electrolytes[59-61]. Decoupling of ion conductivity from polymer segmental relaxation is observed in some fragile systems, which provides a novel concept for new SPE design[88-89]. With the aid of computer modeling, the polymer dynamics and ion association in both polymer/salt blends and single ion conductors have been systematically studied[90-97]. Figure 2.2 gives a general summary of the development of the SPE systems during the last four decades.

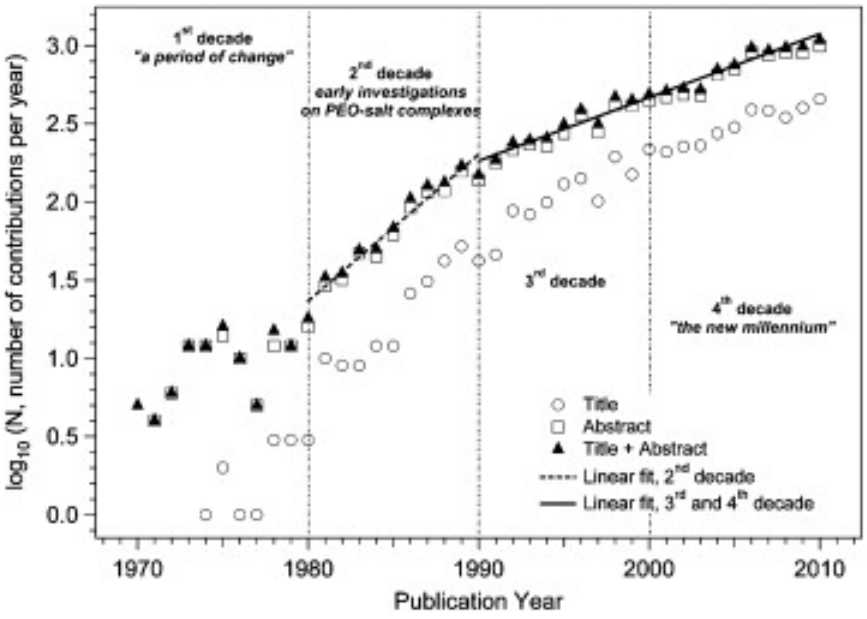

Figure 2.1 Number of publications related to polymer electrolytes in the past forty years. The growth of publications was in an almost log-liner fashion. Adopted from ref.[11]

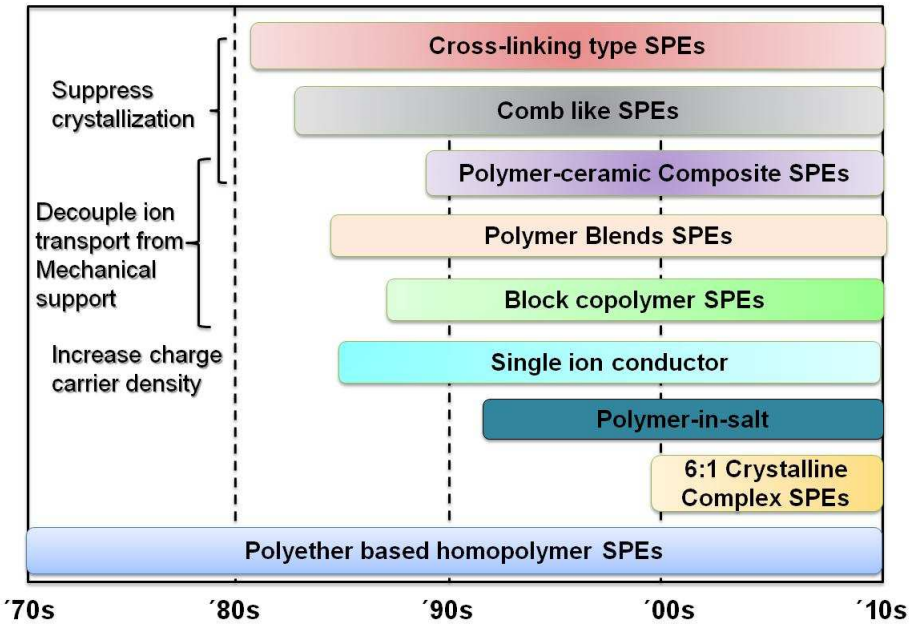

Figure 2.2 Summary of solid polymer electrolyte development during the last four decades.

2.2 Fundamentals of SPEs

2.2.1 Formation of polymer- lithium salt complex

In order to effectively solvate the salt and form polymer-lithium complex, the following basic criteria need to be satisfied for the host polymers: (i) high dielectric constant (ε); (ii) high electron-donor characteristics, polymers with high concentration of sequential polar groups on their backbone such as ether (-O-), sulfide (-S-), amine (-N-), phosphine (-P-), carbonyl (C=O) and cyano (C=N) are good candidates for complex formation[8, 13]; (iii) appropriate distance between coordinating centers, which is best illustrated by crown ethers[98-99]; (iv) flexible backbone and low steric hindrance for bond rotation; (v) easy to synthesize and process. PEO is one of the most popularly selected candidate since it exhibits strong ability to form complexes with a variety of metal salts[7-

[9, 76, 100]. The ethylene oxide unit (CH_2CH_2O) has both strong electron donor characteristics and an optimal heteroatom spacing that facilitates the dissociation of the salt. And the high flexibility of the PEO chain indicated by a low glass transition temperature allows the reorganization of the chain for cation coordination. Polypropylene oxide (PPO) is another candidate as an ion-hosting polymer. Although it remains amorphous at room temperature that favors ion mobility, the solvation ability is less effective compared with PEO due to its low dielectric constant and the stereo hindrance imposed by the additional methyl groups[7-8]. Other polymers such as polysiloxanes, poly(ethylene succinate) and poly(ethylene imine) all have shown certain capacity of complex formation with alkali metal salts but are far less competitive with PEO based polyethers[7-8].

On the other hand, only salt with low lattice energy has been demonstrated to form complex with given polymer host[8]. These salts are usually characteristic of large anions with negative charges well dispersed by the electron withdrawing ligands. The higher degree of charge delocalization the better solvation of the salt in a given host. The dissociation constant for commonly used anions follows the order below[7, 100-102]:

$$(CF_3SO_2)_2N^-, AsF_6^- > PF_6^- > ClO_4^- > BF_4^- > CF_3SO_3^- > CF_3CO_2^-$$

Other factors that need to be taken into considerations for the salt to be used as solute in the electrolyte include: high solubility and conductivity, inert against electrode, wide electrochemical window, good thermal stability and minimum toxicity. Summaries on the property and performance of different types of salts can be found in several reviews[47, 101, 103].

2.2.2 Ion conduction mechanism in SPEs

The structure of polymers determines the unique ion conduction mechanism. Unlike any liquid electrolyte system in which the small molecules can reorient themselves and accompany the diffusion and migration of the solvated ions, the long range movement of the polymer is restricted due to entanglement. The ion conduction in polymers is through a unique segmental motion assisted ion hopping mechanism as illustrated in Figure 2.3. Li^+ cation forms complex with approximately four to five ether oxygen on the PEO backbone. The movement of the Li^+ cations involves breaking bonds and form new bonds with neighboring coordination sites assisted by the local reorganization of the PEO segments. And it was first demonstrated by Berthier *et al.* using NMR technique that ion mobility only existed in amorphous phase of the polymer above its T_g where the chain mobility is highest[8, 75].

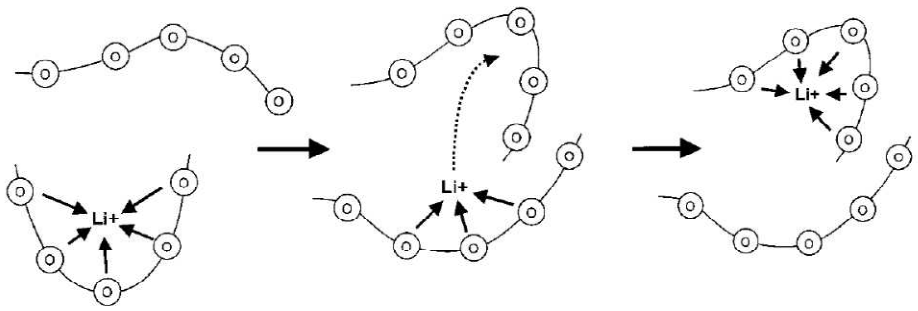

Figure 2.3 Schematics of segmental motion assisted Li^+ cation conduction in a polymer electrolyte, circles represent ether oxygen on PEO backbone, reproduced from ref.[13]

The ionic conductivity of SPEs can be expressed using a general equation as follows:

$$\sigma = \mu \times n \times q \tag{2.1}$$

Where σ is the ionic conductivity of the SPE, μ is the mobility of the charge carrier, n is the concentration of charge carrier and q is the charge of the conducting species. In the case of PEO-lithium SPEs, q equates to 1. The number of charge carriers depends on the degree of salt dissociation while the ion mobility is associated with the host polymer mobility.

Temperature dependent ionic conductivity curves are commonly used to interpret the ion conduction mechanism in polymer electrolyte by fitting the logσ vs. 1/T plot into appropriate models[71]. The Arrhenius behavior of the ionic conductivity can be described by equation (2.2):

$$\sigma = \sigma_0 exp\left(\frac{-E_a}{kT}\right) \tag{2.2}$$

Where the pre-exponential factor σ_0 is related to the number of charge carriers, k is Boltzmann's constant and E_a is the activation energy for conductivity. For amorphous SPEs, the temperature dependent conductivity plot often exhibited curvature that deviated from typical Arrhenius behavior, and this phenomenon can be better described using a Vogel-Tamman-Fulcher (VTF) equation[104-106] as follows:

$$\sigma = \sigma_0 T^{-\frac{1}{2}} exp\left(\frac{-B}{T - T_0}\right) \tag{2.3}$$

Where B is the pseudo-activation energy for conductivity and can be expressed as E_a/k, T_0 is considered as an equilibrium glass transition temperature and is normally 10-50K below the experimentally measured kinetic T_g. The VTF equation are derived from the quasi-thermodynamic models such as free volume[107] or configurational entropy[108] and is more relevant for amorphous polymer electrolyte in which the ion motion is related to the long range polymer segment motion.

Another phenomenal model based on the WLF (Williams, Landel and Ferry) scaling law[7, 9, 76, 109-110] that commonly used in polymer science to discuss the viscosity and glass transition temperature correlations has also been modified and applied to SPE systems:

$$log\left[\sigma(T)/\sigma(T_s)\right] = log\alpha_T = \frac{-C_1(T-T_s)}{C_2+(T-T_s)} \tag{2.4}$$

Where T_s is an arbitrary reference temperature, α_T is called the mechanical shift factor and C_1 and C_2 are universal constants. The two expressions (2.3 and 2.4) are essentially the same when $C_1C_2 = B/k$ and $C_2 = T_s - T_0$. Both VTF and WLF are empirical models that fit very well for a variety of amorphous SPE systems and indicate that ion conduction in SPEs is largely determined by the chain mobility. Although one drawback is that these models do not take into account for the ion-ion interaction and ion associations, which may introduce errors especially at higher ion concentrations.

2.2.3 Phase diagrams of PEO based SPEs

The phase behavior and crystalline morphology of PEO-lithium salt SPEs had been extensively studied since 1980s[63-64, 67, 74-75, 111-113]. Several phases are defined in PEO-lithium salt SPEs: crystalline PEO phase, amorphous PEO-lithium complex phase, and stoichiometric crystalline PEO-lithium complex phases. The number and type of phases depend on the anion identity, salt concentration as well as thermal history and can be determined by X-ray diffraction, nuclear magnetic resonance spectroscopy, thermal analysis or polarized light microscopy[111]. We define three regions of semicrystalline SPEs based on the type of phases present in the electrolyte at room temperature in this thesis. Dilute electrolytes (typically at O/Li molar ratio less than 20) consist of only two phases: crystalline PEO phase and amorphous PEO-lithium complex phase. Semi-dilute electrolytes (O/Li molar ratio around 8-20) have the most complicated morphology where multiple phases co-exist, including crystalline PEO, amorphous PEO-lithium complex phase and crystalline PEO-lithium complex phases. Concentrated SPEs (or polymer in salt) only consist of crystalline complexes with stoichiometry of 6:1, 4:1, 3:1 or 2:1 depending on the type of anion.

Figure 2.4 shows the phase diagrams of a few commonly studied PEO-lithium salt SPEs[111, 114]. Stoichiometric compound of 6:1 and 3:1 are found in SPEs containing $LiClO_4$, $LiAsF_6$ and LiTFSI, while only PEO-lithium 3:1 complex is identified in PEO-$LiCF_3SO_3$ SPEs. A eutectic with melting temperature of 50-55 °C is observed for all types of SPEs at composition range from 10< O/Li molar ratio< 100 expect for low M_w PEO-LiTFSI SPEs, in which a crystallinity gap between 6< O/Li molar ratio< 12 is

observed due to the plasticizing effect of $TFSI^-$ anion. $P(EO)_6LiAsF_6$ has a melting temperature of 136 °C, which is 70 °C higher than that of $P(EO)_6LiClO_4$. Most $P(EO)_3LiX$ complexes have melting temperatures above 100 °C.

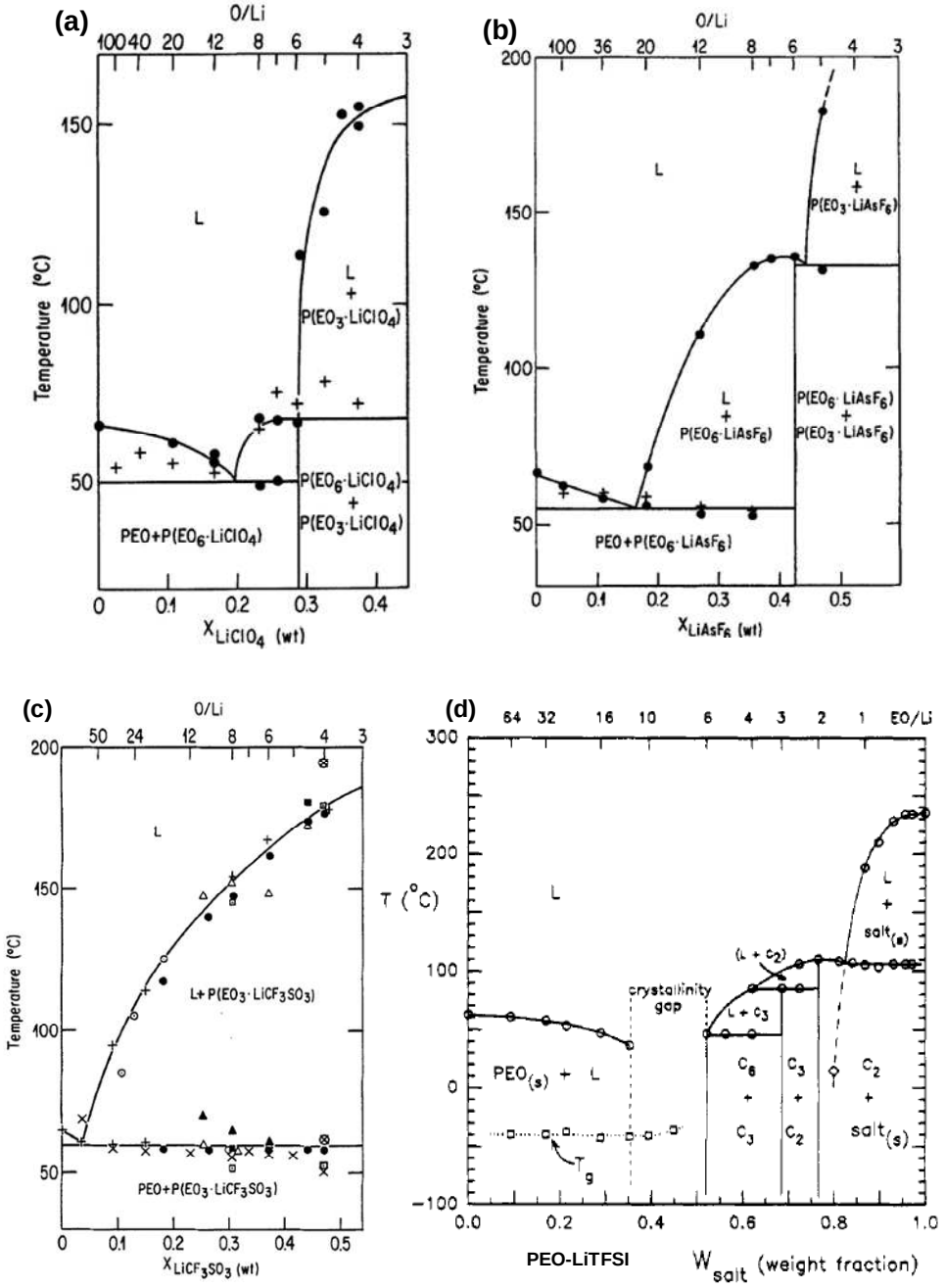

Figure 2.4 Phase diagrams of a series PEO-LiX electrolytes: (a) PEO-$LiClO_4$; (b) PEO-$LiAsF_6$; (c) PEO-$LiCF_3SO_3$; (d) PEO-LiTFSI. Figures (a-c) are reproduced from ref [111] and figure (d) is reproduced from ref [114].

Polarized light microscopy experiments reveals that PEO crystallizes into fringed spherulite in dilute SPEs, due to the strong interference with lithium salts[66, 115-116]. During the crystallization process, lithium salts are expelled from the crystals and enriched in the amorphous phase between adjacent spherulites as well as in the amorphous inter-lamellar region. The inhomogeneity of the SPEs can be probed using impedance spectroscopy[65]. In semi-dilute electrolytes, both PEO-lithium complex (salt-rich) phase and PEO (salt-poor) phases crystallize into spherulitic morphology[63, 112]. SEM along with EDX analysis in Figure 2.5 clearly reveal the morphology and salt distribution in a $P(EO)_{20}LiCF_3SO_3$ SPE[112]. Those salt-rich crystalline complexes also exhibit regular and densely packed spherulitic morphology but with higher melting temperatures[74-75, 117].

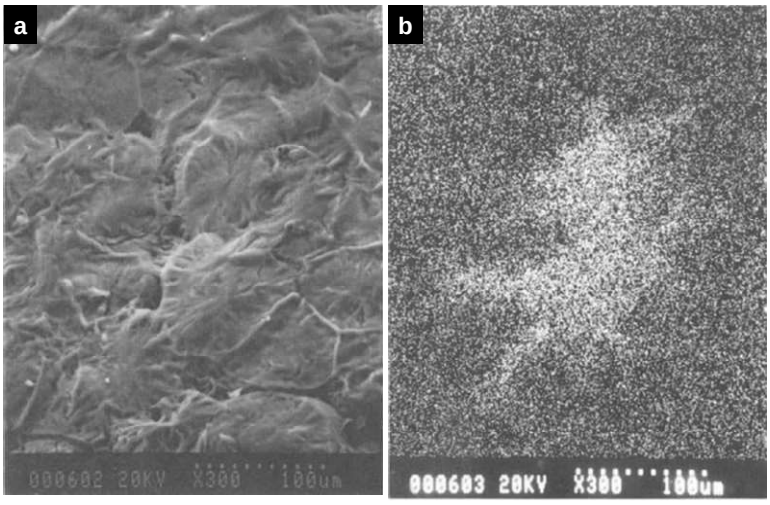

Figure 2.5 (a) SEM micrograph and (b) EDX sulfur map of a $P(EO)_{20}LiCF_3SO_3$ SPE, reproduced from ref.[112]

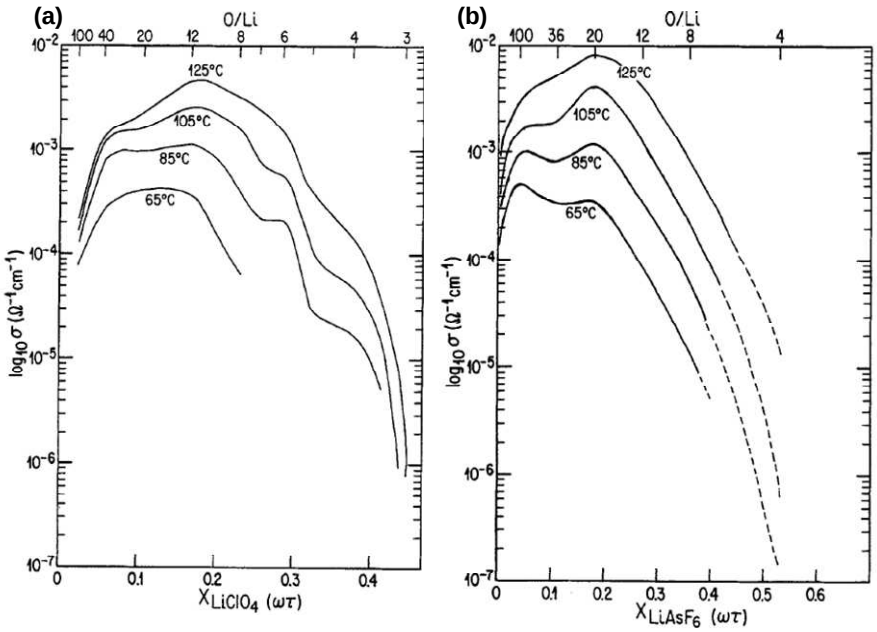

Figure 2.6 Ionic conductivity as a function of salt content at various temperatures for (a) PEO-$LiClO_4$ system; (b) PEO-$LiAsF_6$ system. (Adapted from ref. [111])

The overall conductivity of the polymer electrolytes is determined by (i) the number of charge carriers; (ii) degree of charge dissociation and (iii) the interaction between the ions and the polymer chain, all of which are strongly affected by the ion concentration. For most of the SPE systems, the optimized ionic conductivity is around O/Li molar ratio of 8~ 20 above PEO melting temperature as shown in Figure 2.6. In dilute region, the ionic conductivity increases monotonically with ion concentration due to the increased number of charge carriers. Above an optimal concentration, ionic conductivity begins to decrease as a result of significant ion pairing and physical cross-linking between polymer chain and Li^+, as well as the formation of PEO-Li crystalline complex that restricts the ion mobility. At temperatures below T_m, the concentration dependence on ionic conductivity is complicated by PEO crystallization.

2.2.4 Ion conduction in semi-crystalline SPEs

The crystallization of linear PEO has been long viewed as unfavorable for ion conduction. Generally speaking, the detrimental impact of crystallization can be categorized into three aspects as illustrated in Figure 2.7: (i) decrease the effective fraction of amorphous conducting phase; (ii) restrict chain mobility (dynamic/tethered chain effect) and (iii) introduce more tortuous pathways for ion transport (tortuosity effect). Although extensive studied had been conducted to understand the correlation between crystallization and ionic conductivity reduction, obtaining a quantitative analysis is challenging since those three factors are usually intertwined.

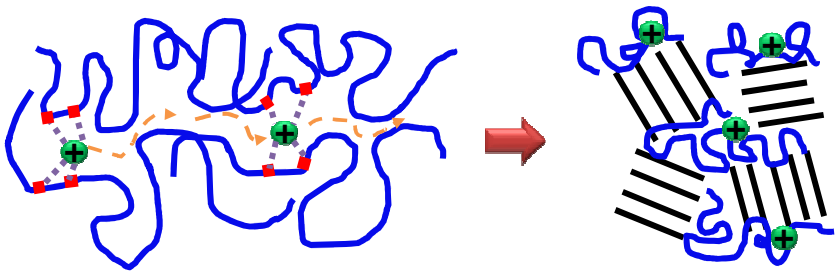

Figure 2.7 Schematic illustration of amorphous to crystalline transition in PEO based SPEs.

The temperature dependent conductivity plots of semicrystalline PEO SPEs provide some useful information on the degree of conductivity reduction due to PEO crystallization. Figure 2.8 shows the conductivity plots of a series of $P(EO)_nLiClO_4$ electrolytes as an example. A conductivity "Knee" is observed for electrolytes at all concentration range around PEO melting temperature T_m (~60 to 70 °C), below which

temperature the conductivity quickly drops to below 10^{-7} S/cm. This 2-3 order of magnitude conductivity reduction at room temperature results from the decrease of the conducting phase volume fraction, restriction of chain mobility and the increased tortuosity as mentioned earlier, whereas the contributions from each factor cannot be quantitatively decoupled. All SPEs follow a typical Arrhenius behavior below the T_m of PEO, suggesting that the long term polymer segmental motion is restricted and ion hopping is the major ion conducting mechanism. The steeper slop at low temperatures indicates a higher energy barrier for ion transport in semicrystalline SPEs.

Figure 2.8 Temperature dependent ionic conductivity for solution cast $P(EO)_nLiClO_4$ electrolytes, reproduced from ref.[111]

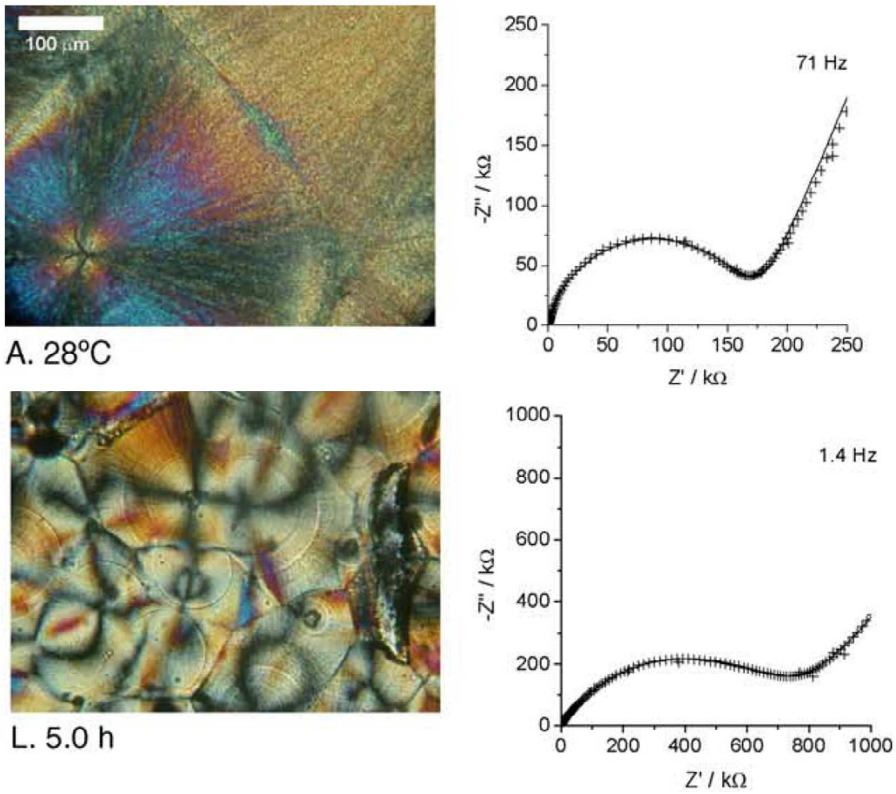

Figure 2.9 Polarized light microscope images (left) and the corresponding impedance spectrum (right) of a $P(EO)_6$: LiTFSI SPE under different thermal conditions, selectively reproduced from ref.[64]

Although the highest ionic conductivity is expected in the completely amorphous state where the chain mobility is highest as opposed to the corresponding semicrystalline SPE with equivalent ion concentration, contradictory observation had been reported by Fullerton-Shirey *et al.* on solution cast PEO-$LiClO_4$ SPE systems[62]. The plot in Figure 2.10 shows that the 14:1 (O/Li molar ratio) sample with 31% crystallinity has comparable and even higher ionic conductivity than the 8:1 sample that is completely amorphous at 22 °C and 50 °C, respectively, although the effective Li^+ concentration (normalized by PEO crystallinity) and the T_g of the two SPEs are the same. Apparently the ion conduction is decoupled from chain mobility in this case and the enhanced ionic

conductivity in semicrystalline SPEs indicates that there might be a fast ion transport in the amorphous conducting phase confined by PEO crystalline lamellae.

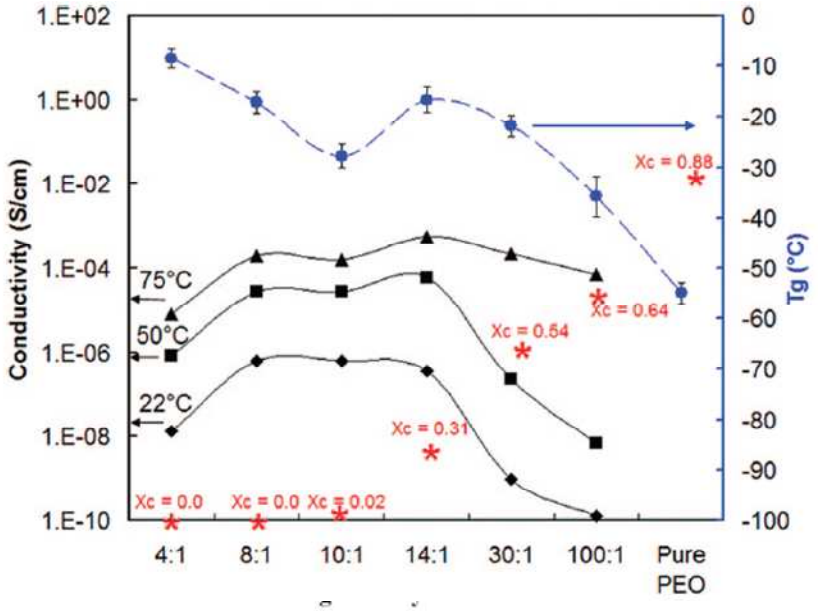

overall EO:Li	X_c (%)	T_g (°C)	effective EO:Li
8:1	0	−17	8:1
10:1	2	−28	10:1
14:1	31	−16.5	8:1

Figure 2.10 Ionic conductivities, glass transition temperatures (T_g) and crystallinity (*) as a function of $LiClO_4$ concentration at different temperatures for PEO-$LiClO_4$ SPEs, reproduced from ref.[62]

2.2.5 Ion conduction in some Crystalline $P(EO)_6$:LiX SPEs

At high concentrations, PEO forms stoichiometric crystalline compounds with Li^+ cation. These crystalline compounds are generally believed to be insulating expect for certain $P(EO)_6$:$LiXF_6$ crystalline complexes (X= P, As, Sb) that were first discovered by Bruce *et al.*[59, 118-119]. The structure of these 6:1 crystalline electrolyte was solved *ab initio* from powder diffraction data for the first time, which ultimately boosts the new

breakthrough of understanding the ion conduction in crystalline SPEs[120]. The structure of $P(EO)_6$:$LiAsF_6$ crystalline complex is illustrated in Figure 2.11. The crystalline complex adopts a monoclinic unit cell. Two PEO chains interlock to form a cylinder with Li^+ cations reside inside the cylinder in a row. Each PEO chain adopts a non-helix conformation of *ctgḡtgcḡtcttgtḡcgt.* The anions are located between the cylinders and do not coordinate with Li^+. The crystalline structures of all three complexes are essentially the same, but as the anion size increases from PF_6^- to AsF_6^- to SbF_6^-, the volume of the unit cell does expand by pushing the cylinders apart along *b* and *c* axis and stretching the polymer chain along *a* axis. Nevertheless, the Li^+ coordination number and Li-O bond strength remain unchanged for all three crystalline complexes.

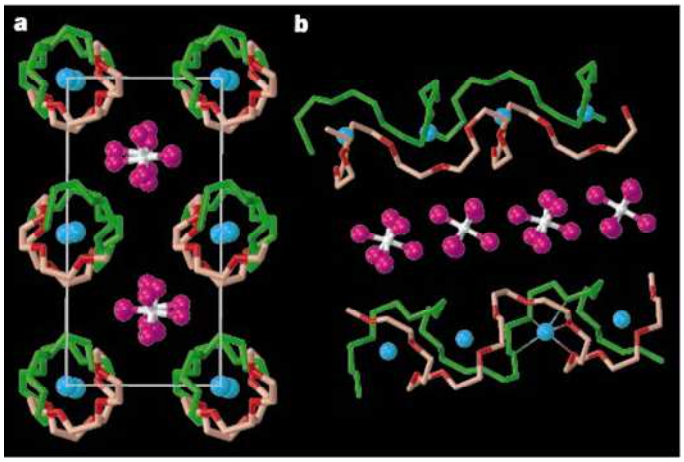

Figure 2.11 crystal structure of $P(EO)_6$:$LiAsF_6$ crystalline complex, reproduced from ref. [59].

The temperature dependent ionic conductivity of crystalline $P(EO)_6$:$LiSbF_6$ as shown in Figure 2.12 suggests that ion conduction not only takes place in crystalline phases but also is faster compared with that in more mobile amorphous phases. The

conductivity plot of $P(EO)_6$:$LiSbF_6$ exhibits typical Arrhenius behavior, indicating an ion hopping mechanism is dominating for the ion conduction. The Li^+ diffusion pathways within the cylinder is also proposed based on the crystal structure and is illustrated in Figure 2.13. Since no crystalline solid is perfect, the migration of Li^+ from one site to the neighboring site is facilitated by the presence of vacancy defects.

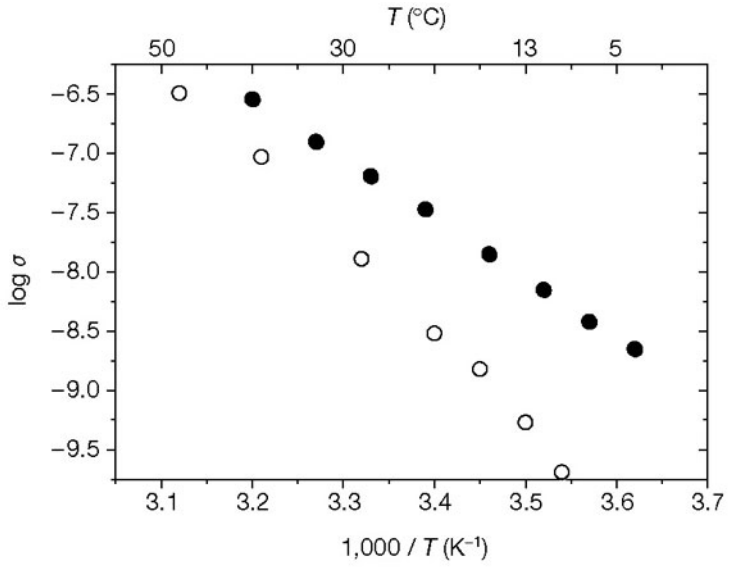

Figure 2.12 Temperature dependent ionic conductivity of crystalline (solid circle) and amorphous (open circle) P(EO)6:$LiSbF_6$, reproduced from ref.[59, 121]

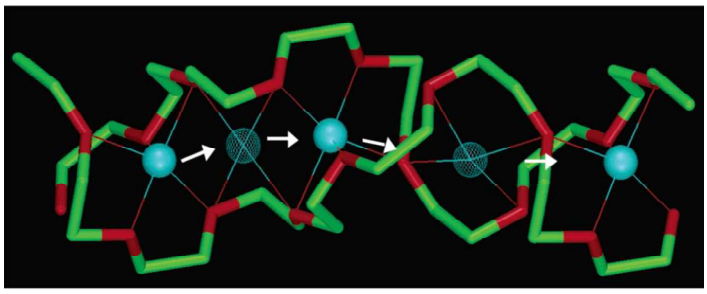

Figure 2.13 Schematic illustration of Li+ diffusion pathways in a $P(EO)_6LiPF_6$ crystalline complex, adopted from ref.[60]

Despite promising ion conduction had been demonstrated in these $P(EO)_6$:$LiXF_6$ crystalline complexes, the room temperature conductivities (10^{-7}~10^{-8} S/cm) are still far less than satisfactory for any applications. Substituting $LiXF_6$ with salt bearing large delocalized anion such as $TFSI^-$ improves the conductivity by one to two order of magnitude due to the disruption of the potential around Li^+ in the region of $TFSI^-$ anion[61]. Increasing the PEO polydispersity or replacing the methoxy capped chain end with $-OC_2H_5$ group may further improve the conductivity by one order of magnitude by introducing more defects that leads to an increased concentration of charge carriers[122]. Another limitation for these crystalline SPEs is that the optimal ionic conductivity is at M_w of 1000 Da, further increasing the M_w significantly reduces ion conductivity due to the increase of grain boundaries and misalignment of the crystallites that impedes ion transport.

In summary, the ion conduction in linear PEO based SPEs is complicated by crystallization. Although there is a direct correlation between polymer dynamics and ion transport in most of the SPEs, cautions need to be taken when interpreting the ionic conductivity in a specific SPE system. The segmental motion along cannot fully explain the ion conduction phenomenon in crystalline SPEs. The structures of the electrolyte, the organization of the polymer chain and the alignment of the conducting channels are also important factors that contribute to the overall ionic conductivity.

2.2.6 Effect of molecular weight on ion conduction

The dependence of molecular weight on the glass transition temperature T_g can be described by the following Fox and Flory equation based on the free volume theory[123]:

$$T_g = T_g^{\infty} - \frac{K}{M_n} \tag{2.5}$$

Where T_g^{∞} is glass transition temperature for an infinitely long polymer chain and K is a constant that related to the excess free volume. According to the theory, the end groups are relatively more mobile compared with the middle segment, which leads to a larger excess of free volume. Increasing the molecular weight will decrease the fraction of end groups, resulting in a reduced free volume, therefore a higher T_g. But this effect is diminished above the critical entanglement molecular weight (M_c), and the T_g becomes nearly constant afterwards.

In amorphous homopolymer electrolyte, the ion conductivity is correlated to the segmental motion of the polymer, which increases with the decrease of T_g. Therefore the effect molecular weight on ion conduction follows the same relationship. Shi and Vincent reported that the cation mobility in PEO host decreases with increasing molecular weight up to a critical molecular weight of 3200 g/mol, above which the molecular weight has little effect on the cation mobility[124]. But it needs to be noticed that of the molecular weight dependence on the conductivity only apply to high temperature situation where the homopolymer is in the molten state, and does not stand for low temperature since the crystallization of the polymer will also have great influence on the conductivity.

In the case of low molecular weight PEO electrolyte, the end group effect also plays an important role to the overall conductivity. Devaux *et al.* had reported that the ionic conductivity for a poly(ethylene glycol dimethyl ether (PEGDM)/LiTFSI electrolyte is higher than that of a poly(ethylene glycol) (PEG) electrolyte with -OH end

groups at 60 °C below M_c of PEO[125]. And the phenomenon is explained as that the polar -OH group has stronger interactions with the anions and cations, which reduces the free volume that is critical to the polymer segmental dynamics.

2.3 State of art development of current SPE systems

As it is mentioned earlier in Chapter 1, the largest challenge for solid polymer electrolyte development is to improve the current room temperature conductivity to at least 10^{-4} S/cm while the shear modulus of the electrolyte needs to maintain sufficiently high (~7GPa by computational simulation[126]) in order to address the lithium dendrite formation problem. During the last few decades, tremendous efforts have been made to develop novel SPE systems that can meet the desired performance requirement; these strategies generally fall into the following three scenarios:

(i) Design of multiphase SPEs to decouple ion transport from mechanical support;

(ii) Improve conductivity anisotropy, optimize ion conducting pathways by creating directional and continuous conducting channels;

(iii) Develop single ion conductor to increase charge carrier density.

Table 2.1 summarizes the properties of current development of SPEs and detailed discussion on each type of SPE system will be discussed in the following sections.

Table 2.1 Summary of the current SPE systems.

Type of SPEs	Category	Examples	σ (S/cm) @ T(°C)	Mechanical strength (Pa)	Ref.
BCP SPEs	(i)	PS-P(S-g-EO)-PS+LiTFSI (O/Li=20)	$2x10^{-5}$ @ RT	10^8 *(1)*	127
		PSt-*b*-PPME-*b*-PSt (80% PEO content)	$\sim10^{-4}$ @ RT	$5x10^6$	38
		PS-*b*-PEO+LiTFSI (O/Li=50)	$\sim10^{-3}$ @ 90	$\sim10^8$ @ 90 *(2)*	22
LC-BCP SPEs	(i), (ii)	PEO-*b*-PMA/CB+$LiClO_4$ (O/Li=120)	$2x10^{-7}$ @ 20 *(3)*	N/A	128
		2/$LiCF_3SO_3$	$1.5x10^{-6}$ @ 35 *(4)*	N/A	129
PEO-ceramic nanofiller	(i), (iii)	PEG(M_n 250 Da)/LiTFSI (O/Li=20) + 20wt% fumed silica	10^{-3} @ RT	10^5 @ RT	130
		$P(EO)_8LiClO_4$ + 10wt% TiO_2 (13nm)	$1.75x10^{-5}$ @ RT	N/A	49
Stretched SPEs	(ii)	$P(EO)_7LiI$	$\sim10^{-4}$ @ RT *(5)*	N/A	131
HP	(i), (ii)	Norland 65+ PEG(400 Da)+LiTFSI (O/Li=19) @ 45 v/v %	$1.93x10^{-5}$ @ RT	N/A	132
Single ion conductor	(iii)	PCHFEM-Li/PEO (M_w 400 kDa) blend	$\sim10^{-5}$ @ 100	N/A	133
		P(MEO-MALi)	$2x10^{-7}$ @ RT	N/A	134
		P(STFSILi)-*b*-PEO-*b*-P(STFSILi) @ O/Li=27	$\sim10^{-5}$ @ 60	$\sim9x10^6$ *(6)*	135

Note:

(1): Dynamic Young's modulus was measured at 1 Hz.

(2): Shear modulus was measured using parallel plate rheometer.

(3): Ionic conductivity was measured parallel to PEO cylinder long axis.

(4): Ionic conductivity was measured parallel to the smectic layer.

(5): d.c. conductivity was measured along the stretching direction using four-probe-electrode setup.

(6): Tensile strength was measured at 40°C on a DMA at 0.1N/min ramp force.

2.4 Decouple ion conduction from mechanical support

2.4.1 Block copolymer (BCP) SPEs

Due to the unique micro-phase separated structure, block copolymer SPEs containing rigid reinforcing segment and soft ion conducting segment provides a decent solution for the decoupling of mechanical properties and ionic conductivity[22-24, 38-46]. The phase separation of the BCPs is governed by the Flory-Huggins interaction parameter (χ). Depending on the degree of polymerization (N) and the volume fraction (f) of each block, the morphology of a linear AB diblock copolymer could change from spherical (S), cylindrical (C), gyroid (G) to lamellar (L) as illustrated in Figure 2.14[136]. To effectively address the lithium dendrite formation problem, BCP with 3D gyroid, 2D cylindrical or lamellar morphologies are more beneficial over the 1D spherical morphology in terms of maximizing mechanical property enhancement[137]. Therefore, most of the BCP SPEs studies have been focused on higher dimensional morphologies.

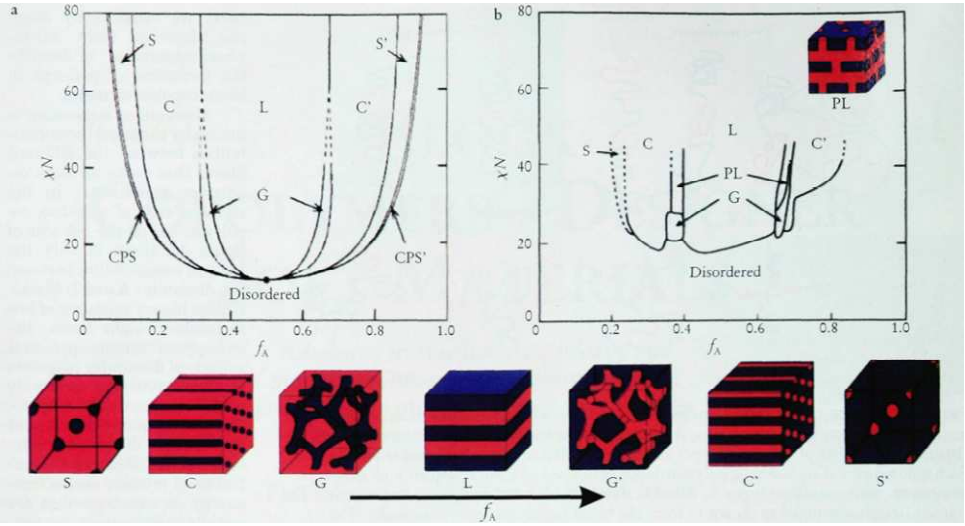

Figure 2.14 Theoretical (a) and experimental (b) phase diagrams for linear AB diblock copolymers, adopted from ref.[136]

2.4.1.1 Effect of salt-doping on the phase behavior and conductivity of BCP SPEs

The most commonly studied BCP SPEs are based on polymer/salt blends in which the salt is preferentially dissolved in the PEO solvating block. Introduction of lithium salt into the conducting domain significantly influences the phase behavior of the BCPs and ultimately impacts the ionic conductivity of the SPEs[22, 25, 29, 39, 138-147]. For example, poly(methyl methacrylate-b-oligooxyethylene methacrylate) (PMMA-*b*-POEM) exhibits a disordered phase at all temperatures due to the thermodynamic compatibility of the two blocks and the order-disorder transition (ODT) temperature is well below its T_g. Doping with appropriate amount of $LiCF_3SO_3$ (O/Li molar ratio of 20:1) dramatically enhanced the phase segregation and shifted the ODT to above 200 °C. Due to resultant phase-separated structure, the ionic conductivity increased one to two order of magnitude compared with the random copolymer P(MMA-*r*-OEM)[39]. Young *et al.* studied the phase

behavior of a PS-PEO diblock copolymer doped with different lithium salt. The morphology changed from hexagonally packed cylinders to lamellar morphologies when the salt concentrations increased from 48:1 to 3:1 (O/Li molar ratio) as shown in Figure 2.15 along with an increased domain spacing[144]. More complicated phase behavior had been studied on some triblock copolymer SPEs. In a $LiClO_4$-doped poly(styrene-b-isoprene-b-ethylene oxide) (PS-PI-PEO) triblock copolymer SPE system studied by Epps et al., two phases (core-shell gyroid and semiperforated lamellae) present in the neat BCP were replaced by the core-shell cylinder phase in the SPEs. Salt doping also led to an expansion of the domain spacing and significant increase of T_{ODT}[138, 141]. The modification of the phase behaviors in these BCP SPE systems is attributed to the change of Flory-Huggins interaction parameter (χ) due to the introduction of the salt. The complexation between PEO chain and lithium ions results in an increased incompatibility between the PEO domain and the non-conducting domain, driving the phase separation towards the strong segregation region.

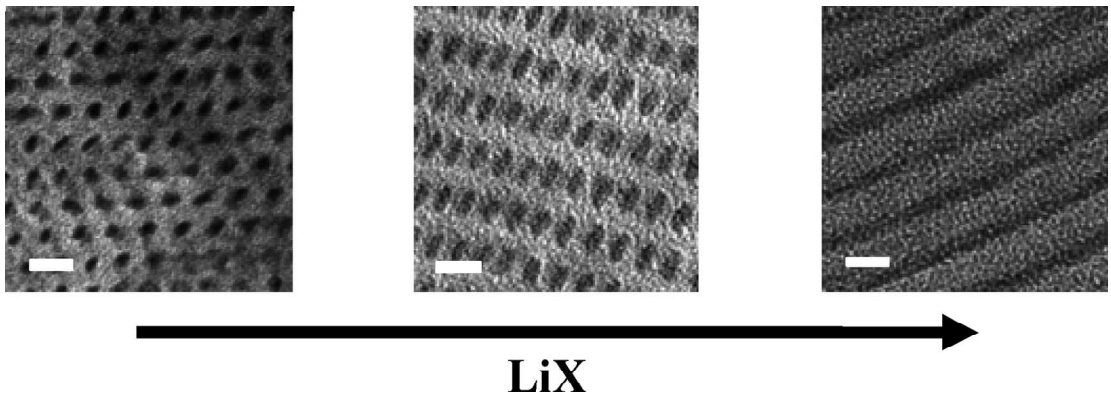

Figure 2.15 TEM micrograph of PS-PEO neat BCP (left), PS-PEO BCP doped with $LiClO_4$ with [EO] to [Li] molar ratio of 6:1 (middle) and 3:1 (right), reproduced from ref.[144]

The local stress induced by phase segregation can also result in a non-uniform distribution of Li^+ ions in the conducting phase. Gomez *et al.* had studied the Li^+ distribution in a PS-PEO BCP SPE with lamellar morphology using energy-filtered transmission electron microscopy[24]. The elemental mapping of the BCP SPE cross-section reveals that lithium ions are preferentially located at the center region of the PEO domains. This is because the PEO chains are stretched at the interface and this extended conformation is unfavorable for EO/Li^+ coordination, leading to an exclusion of the ions away from the PEO-PS interfacial region.

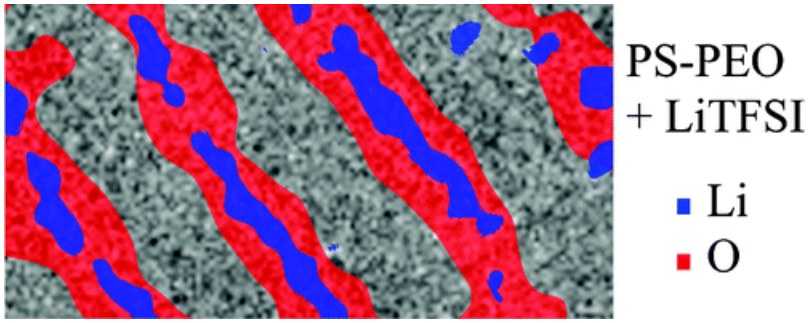

Figure 2.16 Elemental mapping of a PS-PEO BCP SPE doped with LiTFSI. Adopted from ref.[24]

The chain stretching effect at the interface of the two blocks and uneven ion distribution suggest a fundamental difference in ion conduction mechanism between BCP SPEs and homopolymer SPEs. As discussed earlier, the ion conduction mechanism in homopolymer electrolyte system is mainly governed by the polymer segmental motion. The cation mobility initially decreases with the increase of M_w and becomes nearly independent of M_w above the M_c (3200 g/mol for PEO), which is consistent with the molecular weight dependence on T_g. However, the ionic conductivity shows a complex

dependence on the M_w in the BCP SPE case. Balsara and co-workers had systematically studied the M_w effect in a lamellar forming PEO-PS BCP electrolyte doped with LiTFSI[22-24, 148]. In the low molecular weight region where M_{SEO} is below 10 kg/mol, all the ions are confined in the interfacial zone, and the ion conduction is affected by at least two competing factors: T_g of the PS block and the width of the conducting PEO channel, the net effect results in a weak linear declining trend of the normalized conductivity as a function of M_{SEO} (shown in Figure 2.17). When M_{SEO} is above 10 kg/mol, the interfacial effect becomes negligible and the normalized conductivity exhibits a sigmoidal increase with increasing molecular weight due to the increased fraction of the "free" PEO conducting channel.

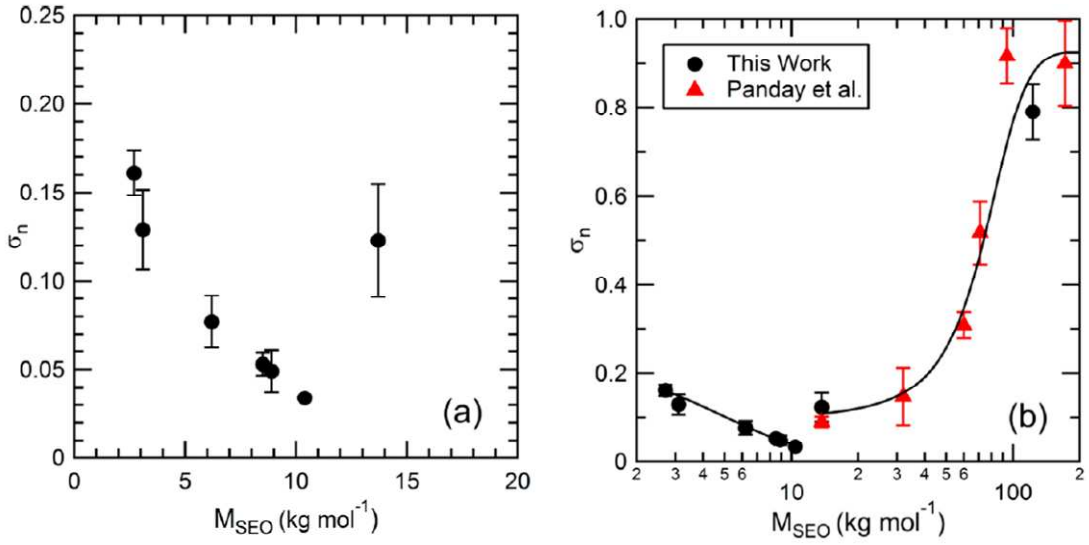

Figure 2.17 Normalized conductivity as a function of M_{PEO} at 90 °C, reproduced from ref.[148]

2.4.1.2 Effect of salt-doping on mechanical properties of BCP SPEs

While extensive interests have been focused on understanding the morphology and ion conduction in BCP SPEs, a limited number of literatures have covered the mechanical property measurements using different characterization techniques. The mechanical integrity of BCP SPEs is largely contributed from the non-conducting glassy phase, in most of the cases, PS or PMMA block. Wang *et al.* reported dynamic Young's modulus on the order of 10^8 Pa between 0 to 100 °C in a microphase-separated poly(styrene-*b*-(styrene-*g*-ethylene oxide)-*b*-styrene) (PS-P(S-g-EO)-PS) graft copolymer SPE doped with LiTFSI, while the room temperature ionic conductivity of the SPE remained ~ $2x10^{-5}$ S/cm, which is 2 order of magnitude higher than its homopolymer counterpart SPE due to the inhibition of PEO crystallization of the BCP[127]. Niitani studied a BAB block copolymer containing polystyrene and poly(ethylene glycol) methyl ether methacrylate (PSt-*b*-PPME-*b*-PSt) prepared by living polymerization. The triblock copolymer doped with $LiClO_4$ exhibited gyroid morphology with a continuous PEO network formation above 70% PEO content. The ionic conductivity reached ~ 10^{-4} S/cm above the percolation of PEO phase whereas the tensile strength dropped below 10^7 Pa at room temperature[38]. Balsara and co-workers had demonstrated that the shear modulus remains unaffected by addition of LiTFSI throughout the entire frequency range for randomly orientated lamellar PS-*b*-PEO diblock copolymer SPEs. And the storage modulus measured using a parallel plate rheometer reached ~ 10^8 Pa at 90 °C for BCP SPE with high molecular weight[22]. Although the reported mechanical properties of current BCP SPEs are still below the 7 GPa shear moduli that is required to completely prevent lithium dendrite formation by computational modeling[126], considerable

improvement on the interfacial stability between the lithium electrode, electrochemical stability window and cycle life of these BCP SPEs had been achieved[30, 38, 127, 149].

2.4.2 Nanocomposite SPEs

Another widely studied approach to address both conductivity and mechanical properties is based on PEO-ceramic nanocomposite SPEs. The incorporation of certain ceramic fillers with Lewis acid characteristic such as TiO_2, SiO_2, or Al_2O_3 are shown to effectively enhance both ionic conductivity and the mechanical properties of the SPEs[48-50, 52-53, 77, 87, 130, 150-162]. During the early investigations, Scrosati and co-workers had found that the addition of micro-sized ceramic particles γ-$LiAlO_2$ into a $P(EO)_8LiClO_4$ SPE improved the mechanical property, interfacial stability and ionic conductivity[150]. However, the mechanism of this enhancement was not well understood. Follow up studies suggests that ceramic particles with nanoscale particle size can result in even better performance, and the ion conduction mechanism in these nanocomposite SPEs had been systematically studied[48-50, 87, 155, 157].

The ion conduction in $P(EO)_8LiClO_4$ nanocomposite SPEs was studied by Scrosati's group[49]. Figure 2.8 compares the temperature dependent conductivity curves of ceramic-free SPE with nanocomposite SPEs containing 10wt% TiO_2 (13 nm) and Al_2O_3 (5.8 nm) nanoparticles, respectively. The as-cast composite SPE containing Al_2O_3 nanoparticles exhibits similar curve as the ceramic-free SPE. However, subsequent cooling curves show completely different behaviors. The conductivity "knee" around 60 °C that commonly observed for neat PEO SPEs disappeared for both TiO_2 and Al_2O_3 nanocomposite SPEs. The room temperature conductivities of the nanocomposite SPEs

were over 2 orders of magnitude higher than that of ceramic-free SPE and remained stable for a few days. The mechanism of this enhancement was explained as the Lewis-acid interactions among the surface of the nanoparticles, the anions and the ether oxygen on PEO chains. The ceramic nanoparticles with Lewis acid characteristic are competing with lithium cations to form complex with PEO segment and anions, which act as cross-linking centers to inhibit polymer re-crystallization. This was confirmed by the absence of melting peaks even after a few days annealing measured by differential scanning calorimetry (DSC)[50].

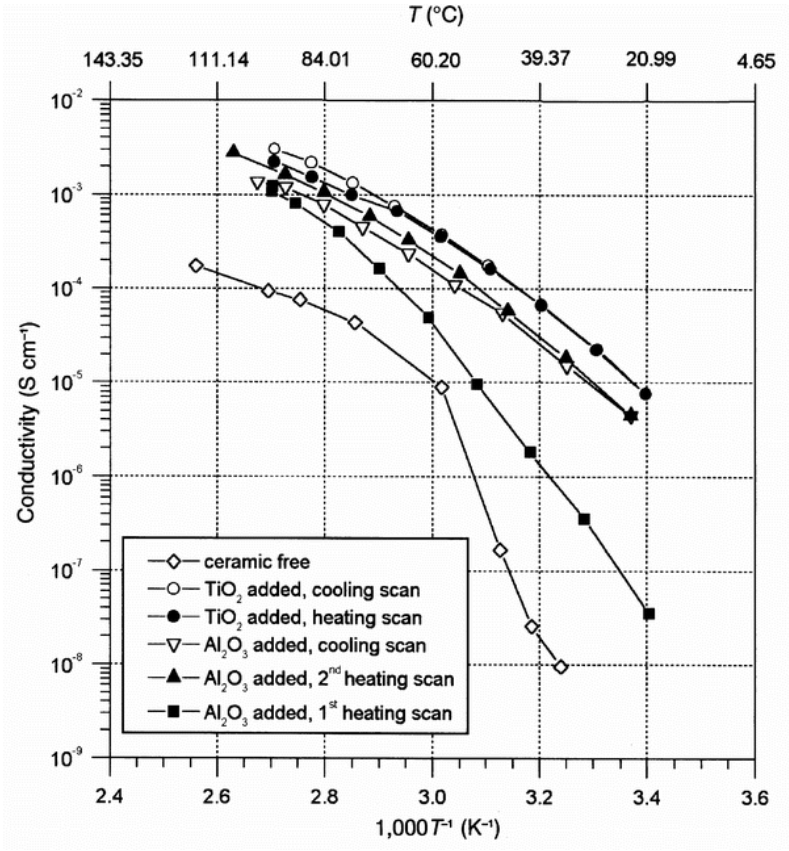

Figure 2.18 Temperature dependent ionic conductivity of PEO-$LiClO_4$ ceramic-free and nanocomposite SPEs, adopted from ref.[49]

However, the theory alone cannot explain the enhanced ionic conductivity above the T_m of PEO, where PEO remains in amorphous state in both systems. Additional mechanisms of the ceramic particle surface effect were further investigated. Chung *et al.* reported that the cation transference number t^+ for the nanocomposite SPEs (0.5-0.6 for SPE containing TiO_2) was considerably higher than the ceramic-free SPEs (usually 0.2-0.3). And the cation diffusivity measured by NMR methods was nearly one order of magnitude higher in the nanocomposite SPEs[87]. These evidences likely suggest that the specific Lewis acid-base interactions among the ceramic surface groups, lithium salt and the polymer segments facilitate the ion dissociation and possibly create preferential conducting pathways at the boundaries of the ceramic particles to promote Li^+ transport.

The type of the functional groups on the surface of the ceramic particles plays a critical role to the ion conduction in nanocomposite SPEs. In a study conducted by Croce *et al*., Al_2O_3 nanoparticles with different surface characteristics: acidic, neutral and basic had been incorporated into a $P(EO)_{20}LiSO_3CF_3$ SPE[157]. The acidic/neutral Al_2O_3 based SPEs showed higher degree of conductivity enhancement over basic Al_2O_3 SPE. The author proposed the mechanism to be the specific Lewis-acid interactions as illustrated in Figure 2.19. Acidic/neutral Al_2O_3 formed hydrogen bonding with the anions as well as the ether oxygen on PEO chain, promoting the salt dissociation and weakening the cation-polymer coordination; while the basic Al_2O_3 can only interact with Li^+. However, the study conducted by Jayathilaka *et al.* on a $P(EO)_9LiTFSI$ SPE system suggests that there is no direct interaction between the filler particles and the polymer chain. The Al_2O_3 particles interact with both cations and anions, providing additional sites for ion hopping. The degree of conductivity improvement by the nanoparticles followed the order: acidic

> basic > neutral > weakly acidic > filler free[53]. Other study on low M_w PEG-$LiClO_4$-Al_2O_3 system showed that the neutral fillers gave higher conductivity compared with acidic and basic fillers[52]. There is no clear trend of role of surface groups and it seems the specific interactions also depend on the type of anions and the polymer matrix being used.

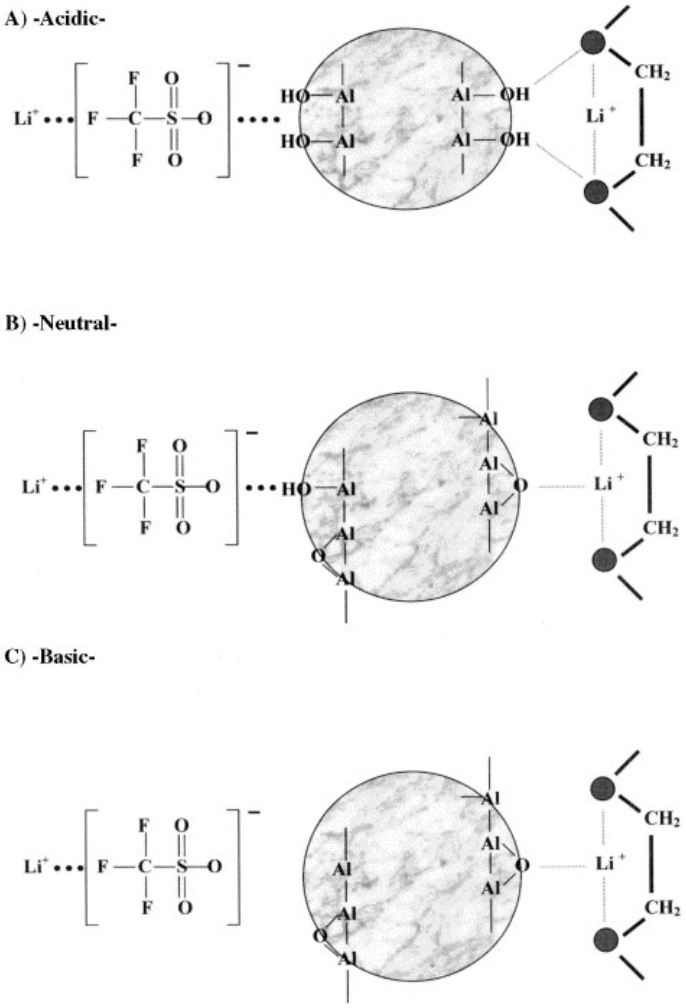

Figure 2.19 Illustration of the surface interaction between Al_2O_3 nanoparticles with different surface characteristics and the PEO-$LiSO_3CF_3$ complex. (cited from ref [157])

Although the nanocomposite approach for novel SPE development appears to be promising, the enhancement of conductivity due to the nanoparticles is not universal and contradictory results had been found in other SPEs. Best *et al.* found no improvement and even a decrease of conductivity in some fully amorphous polyether based SPEs with the addition of TiO_2 or Al_2O_3 nanoparticles[51]. Johansson *et al.* reported no significant influence of the SiO_2 fillers on the amorphous PEO-LiTFSI SPEs[54]. Xie *et al.* studied a PEO-LiTFSI SPE containing fumed silica nanoparticles and conductivity of the composite SPE was found to be decreased above T_m compared with ultra pure PEO SPEs[55]. Depending on the type of anions, the nature of the nanoparticles and the structure and M_w of the polymer, different ion conduction mechanisms may be proposed. A better understanding on the fundamentals of ion transport in these multiphase SPE systems needs to be promoted.

2.5 Improve conductivity anisotropy

2.5.1 Alignment of BCP SPEs

Self-assembled BCP electrolyte membranes with 1D cylindrical forming or 2D lamellar forming morphologies often consist of randomly orientated grains. Based on the effective medium theory[163], a morphological factor (*f*) has been introduced to count for the tortuosity effect on the conductivity of BCP SPEs. And *f* equals to 1/3 for cylindrical BCPs and 2/3 for lamellar forming BCPs. Alignment of the micro-domains leads to an improvement of the conductivity by creating continuous conducting pathways for directional ion transport. Park *et al*. studied the alignment of a hydrated poly(styrenesulfonate-*b*-methylbutylene) (PS-PMB) BCP film with lamellar morphology

using several approaches, including hot press, applying external forces such as electric field or mechanical shear force[164]. In this study, the highest conductivity anisotropy was reported to be 75 in the hot pressed sample. And only 30% conductivity improvement after alignment was achieved.

Liquid crystal (LC) directed BCP alignment appears to be a more efficient approach to enhance the conductivity anisotropy[128-129, 165-169]. Kishimoto first reported a macroscopically oriented LC polymeric film with layered nanostructure prepared by in-situ photopolymerization. The ethylene oxide segment was selectively doped with $LiSO_3CF_3$ for ion conduction and the mesogenic core induced the self-assembly[129]. The electrolyte membrane was spontaneously aligned perpendicular to the glass or ITO substrate when cooled from the isotropic to smectic A phases. And conductivity anisotropy of $4.5x10^3$ was observed at 35 °C, indicating that the ion conduction is efficiently confined within the layer. Li *et al.* reported an anisotropy factor of 450 for a LC-BCP SPE PEO_{114}-*b*-$PMA(Az)_{47}$ at [EO] to $LiCF_3SO_3$ molar ratio of 20[166]. However, the degree of alignment of both two systems is limited to micrometer scale along thickness direction and none of the studies had compared the in-plane conductivity of the aligned SPEs with the isotropic or intrinsic conductivity values.

Great effects had been made by Osuji and co-workers for macroscopic alignment of LC-BCP SPEs using magnetic field[128, 167-172]. Figure 2.20 shows an example of the structure of a poly(ethylene oxide-b-6-(4'-cyanobiphenyl-4-yloxy)-hexyl methacrylate) PEO-*b*-PMA/CB block copolymer membrane. $LiClO_4$ was selectively doped into the

PEO cylindrical domains for ion conduction and the alignment of PEO cylinders was directed by the smectic poly(MA/CB) block upon magnetic field.

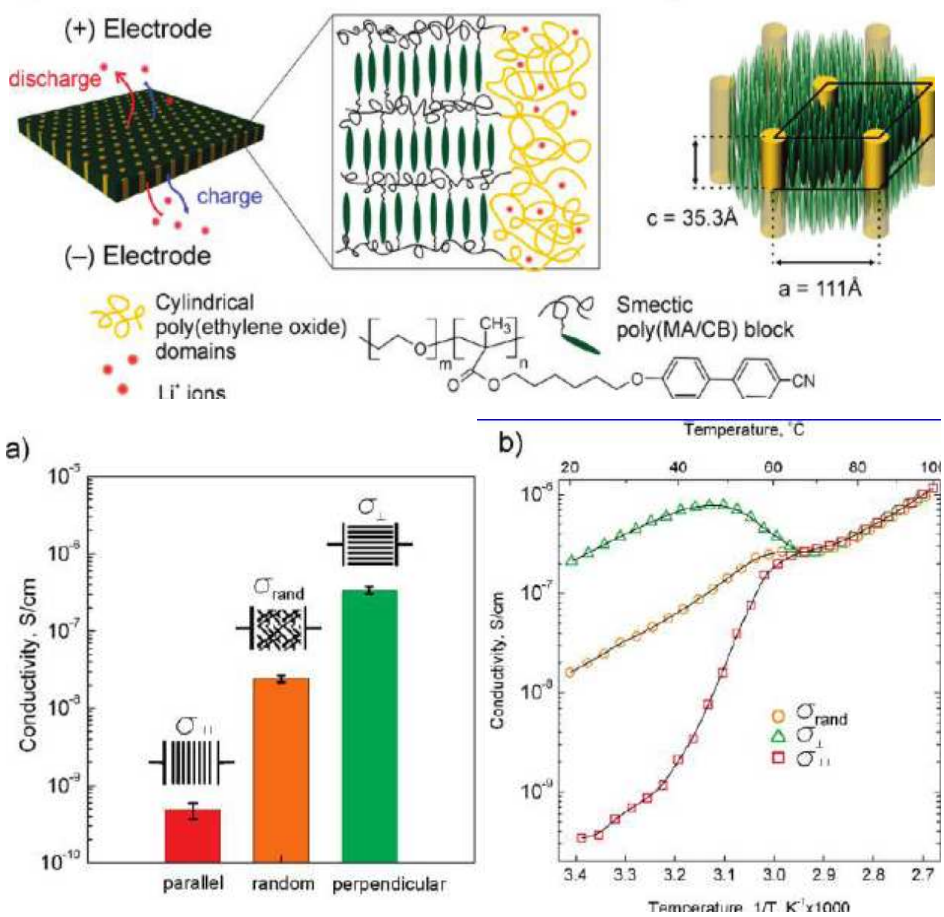

Figure 2.20 Structure of the poly(ethylene oxide-*b*-6-(4'-cyanobiphenyl-4-yloxy)-hexyl methacrylate) PEO-*b*-PMA/CB BCP membrane doped with $LiClO_4$ (top); a) Room temperature ionic conductivities and b) temperature dependent conductivity plots of random BCP SPE and aligned BCP SPE along two orthogonal directions. (Cited from ref.[128])

The parallel (//) and perpendicular (⊥) directions are defined as the PEO cylinders parallel and orthogonal to the electrode surface, respectively. The conductivity anisotropy ($\sigma_{//}$ / $\sigma_{\perp}$) reached ~ 10^3 under 5T magnetic field, suggesting the effective blocking of ions

migration transverse to the PEO cylinder long axis direction. Interestingly, a nearly 10-fold increase of the $\sigma_{\perp}$ compared with that of isotropic SPE was observed, which deviated from the expected 2-fold increase based on the morphological argument predicted by effective medium theory. And the discrepancy suggests that the less ideal connectivity at the grain boundaries may have caused the conductivity decrease in the isotropic LC-BCP SPEs.

2.5.2 Holographic polymerization

Holographic polymerization (HP) technique has been used to fabricate tunable periodic nanostructured membranes with long-range order and low defect[173]. Recently it has been demonstrated that this versatile technique can be used to fabricate novel electrolyte membrane with both robust mechanical property and highly ordered conducting channels. During the photopolymerization process, a mixture of polymerizable monomers, initiators and inert components are exposed to an interference pattern generated by two or more coherent beams. The monomers diffuse into the light or constructive region and start to cross link, while all the inert components are excluded into the dark destructive area. Depending on the geometry of the optical setups, 1D, 2D or 3D nanostructure with tunable spacing can be readily patterned. Smith *et al.* had first reported a holographic polymerized SPE, in which PEO-LiTFSI electrolyte was confined in ~100 nm layered conducting channels[132]. The ionic conductivity along the channels was consistently higher than the isotropic conductivity especially at high PEO-LiTFSI volume loadings, clearly indicating the importance of structural ordering on the conductivity improvement (Figure 2.21). It is expected that selecting appropriate recipe

to enhance the phase separation during the photopolymerization process could further improve the structure ordering and consequently optimize the ion conducting channel.

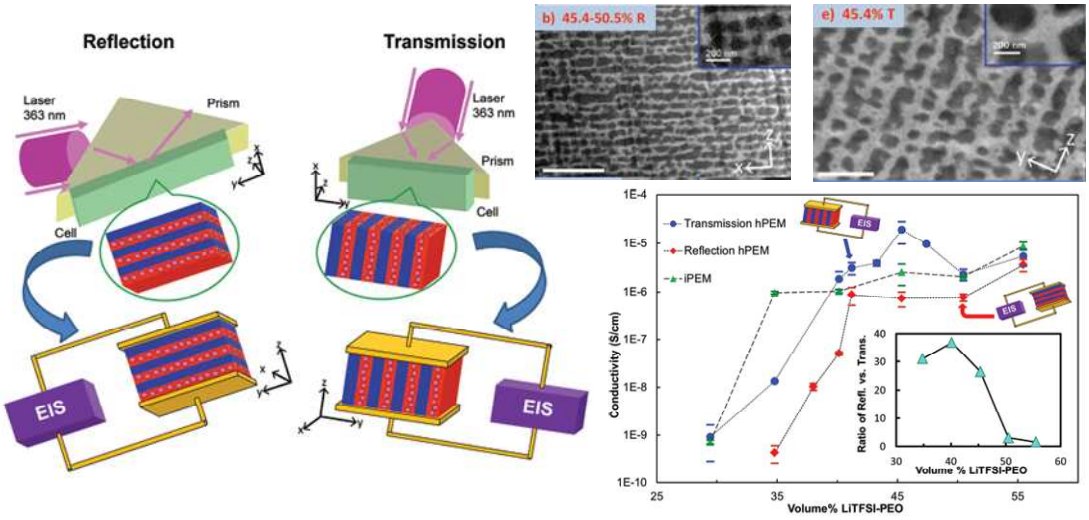

Figure 2.21 Left: Schematics of the optical set up for reflection and transmission gratings and electrode configuration for conductivity measurements; Right: Ionic conductivity as a function of PEO-LiTFSI volume fraction and cross-section morphologies of selected SPEs. Reproduced from ref.[132]

2.5.3 Stretched SPEs

Anisotropic conductivity was also found in some stretched semi-crystalline PEO SPEs[131, 174-181]. Golodnitsky and co-workers had reported stretching induced d.c. conductivity enhancement by a factor of 5 to 40 in several $P(EO)_nLiX$ (X= I, CF_3SO_3, TFSI, BOB) electrolytes[131, 174-176, 181]. In these studies, the hot pressed electrolyte membrane was uniaxially stretched under 450-500 N/cm^2 load at elevated temperatures and the in-situ longitudinal conductivity was monitored using four-probe-dc setup (Figure 2.22 left). Stretching induces the unraveling of loops in the polymer molecule and enhances the

chain alignment along the direction of applied force (Figure 2.22 right). Despite a decrease of polymer segmental motion, Li^+ hopping along the helix is facilitated by the long range order, as supported by the enhanced Li^+ diffusivity measured by Li NMR and the decreased activation energy obtained from Arrhenius plot. Maximum conductivity anisotropy of 40 was observed in a concentrated semi-crystalline electrolyte $P(EO)_7LiI$, in which the partial alignment of the PEO helices in the crystalline phase was believed to be responsible for the conductivity enhancement.

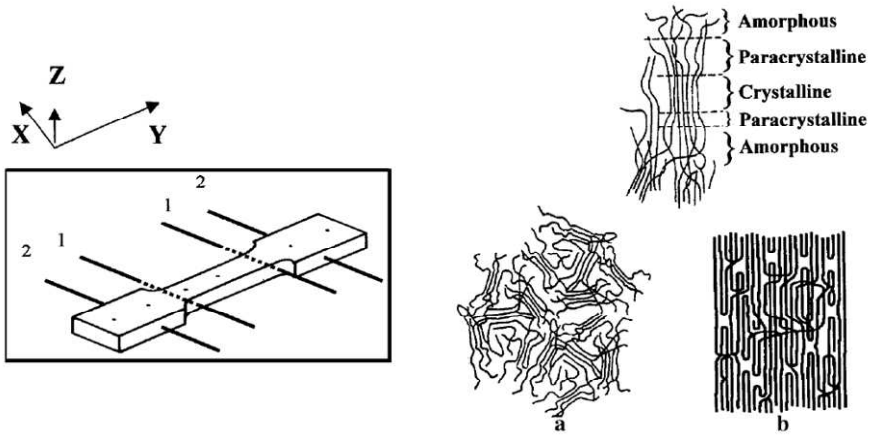

Figure 2.22 Illustration of the electrolyte specimen for stretching experiments and the positions of elelectrodes (left); Schematics of crystalline structure of the PEO electrolyte before and after stretching (right), reproduced from ref.[174]

Although the degree of longitudinal conductivity and anisotropy factor enhancement are moderate in these studies, the results provide valuable insights: ion conduction can be decoupled from polymer segmental motion, and the chain organization and long-range order are also critical to facilitate a fast ion transport.

2.6 Develop single ion conductors

In most polymer/salt blend SPEs, the cations and anions are dissociated in the polymer and both species can move upon the external electric field and contribute to the measured ionic conductivity. During charge and discharge cycles, a concentration gradient of the anions would gradually build up, causing a decrease of current density of the battery. Therefore, increasing cation transference number by developing single ion conductors is important to improve the cycle life of the batteries. There are generally three approaches to develop single ion conductors:

(i) Selection of salt with low lattice energy and immobile anions to facilitate salt dissociation and promote Li^+ transport. Vallée *et al.* first reported the advantage of using large delocalized imide salt LiTFSI over other commonly used salt such as $LiClO_4$[182]. Although this polymer/salt blend system is not an ideal single ion conductor, substantial improvement on the room temperature conductivity ($4x10^{-5}$ S/cm) had achieved due to the enhanced charge carrier density.

(ii) Blend of polyelectrolyte and ion-conductive polymer or oligomer. Bannister *et al.* first studied blends of PEO with two types of polyanionic addition polymers. Blend containing perfluoroalkylcarboxylate groups showed comparatively higher conductivity ~10^{-5} S/cm at 100 °C[133]. Hardy *et al.* reported Na^+ conductivity of $2x10^{-6}$ S/cm at 26 °C and $1x10^{-4}$ S/cm at 98 °C for a blend of PEG (M_w ~300) and sodium poly(styrene-sulfonate)[183]. Very recently Doyle *et al.* reported a single ion conductor blend of linear poly(ethyleneimine)-*g*-poly(ethylene glycol) and linear poly(ethyleneimine) bearing lithium *N*-propylsulfonate groups and a room temperature conductivity of $4x10^{-4}$ S/cm

was observed[184]. The blending approach is advantageous of simple preparation, though attention needs to be paid on the compatibility of the polymers in order to avoid phase separation.

(iii) Covalently immobilization of anion species onto the ion conducting polymer backbone. Copolymers consist of charge carrier containing block and ion conducting block are widely studied. For example, poly(alkali-metal methacrylate-*co*-oligo(oxyethylene)methacrylate)[134, 185], polyphosphazene sulfonates[186], siloxane comb polymers with pendant oligo-oxyethylene segments and sulfonate groups[187], lithium siloxyaluminate polymers containing PEO side chains[188-189]. A few network polymers with –COOLi or $-R_FSO_3Li$ covalently bonded onto the polymer backbone had been studied[190-191]. Other polyacrylate/polymethacrylate based network single ion conductors had also been reported but tedious synthesis steps were involved[192]. Homopolymer single ion conductors consist of both charge carrier and ion conductive species on the same backbone had also been reported[193-194]. However, low room temperature conductivities of 10^{-7} ~10^{-8} S/cm had been reported in these systems due to insufficient ion dissociation. Substituting with large TFSI anions had shown ~ one order of magnitude improvement on the ionic conductivity, examples include lithium poly[(4-styrenesulfonyl) (TFSI-*co*-methoxy-polyethylene glycol acrylate][195] and P(STFSILi)-*b*-PEO-*b*-P(STFSILi)[135]. On the other hand, considerable effects had been made recently in understanding the segmental dynamics and ion association of single ion conductors with precisely controlled structure by combining X-ray or neutron scattering, dielectric relaxation spectroscopy and molecular dynamics simulations[90-97].

2.7 Summary

In this chapter, a brief introduction of the history of polymer electrolyte was first described; the basics of ion conduction in PEO based SPEs was discussed and the state of art development of the current SPE systems was reviewed in details. Depending on the nature of the SPE system, the ion transport properties could be quite different (for example, BCP SPEs, nanocomposite SPEs compared with basic amorphous homopolymer SPEs). Although the ion conduction in polymers is strongly associated with chain dynamics, it is not a requisite for fast ion transport. Further understanding of the fundamentals of ion conduction mechanism in the current SPE systems is highly desirable.

CHAPTER 3: **MATERIALS AND METHODS**

3.1 Chemicals

Natural flake graphite with an average lateral size of ~44 µm was kindly provided by Asbury Carbons, Inc. Hydrochloric acid (HCl) (37%), sulfuric acid (H_2SO_4) (95-98%), potassium permanganate ($KMnO_4$) (≥99.0%), sodium nitrate ($NaNO_3$) (≥99.0%), hydrogen peroxide (H_2O_2) (35%), hydrazine hydrate ($N_2H_4 \cdot H_2O$) (50-60%), 1,2-dichlorobenzene (DCB) (spectrophotometric grade, 99%), *N, N'*-Dimethylformamide (DMF) (anhydrous, 99.8%), pentyl acetate (99%), lithium perchlorate ($LiClO_4$) (battery grade, dry, 99.99% trace metals basis), lithium Bis (trifluoromethane)sulfonimide (LiTFSI) (99.95% trace metals basis), Lithium (foil, thickness 0.6mm, as rolled, 99.9%) and poly(ethylene oxide) (PEO) (average M_n ~ 300 kDa) were purchased from Sigma-Aldrich. All chemicals were used as received, unless otherwise specified.

Both $LiClO_4$ and LiTFSI powders were heated in vacuum oven at 100 °C overnight right before use in order to remove moisture content. The solvent DMF was dried using 4Å molecular sieve for 10 min before use. Pentyl acetate was distilled and filtered through a 0.2 µm PTFE membrane before use.

3.2 Methods

3.2.1 Synthesis of graphene oxide (GO)

Graphite oxide was synthesized using the modified Hummers method[196-197]. Graphite (1.0 g), $NaNO_3$ (0.5 g), and $KMnO_4$ (3.0 g) were loaded into a 50 ml flask and

cooled in an ice bath, followed by slow addition of 25 ml H_2SO_4 under stirring. The mixture was then heated to 35°C in an oil bath with continued stirring for 2 h. The product was poured into excess deionized (DI) water and cooled in ice bath. H_2O_2 was slowly added until no gas evolution was observed. The product was then filtered, washed with 5% HCl solution and DI water, and was subsequently dried in a vacuum oven at room temperature over one week. One or a-few-layer graphene oxide (GO) nanosheets were obtained by sonicating graphite oxide in DMF solution.

3.2.2 Preparation of solution cast PEO SPEs

PEO SPEs were prepared using a solution cast method. 500 mg PEO was first dissolved in 8 ml DMF in a glass vial at ~ 45 °C for 2 hrs. Then, lithium salt powder with desired O/Li molar ratio was added to the solution. The mixture was purged with N_2 for 10 min and sealed with parafilm. After N_2 purge, the mixture was transferred to a 45 °C hot plate and continued stirring for 24 hrs to obtain a homogeneous solution. The solution was casted on PTFE petri dish and dried under vacuum at 45 °C for 5-7 days. Bubbles generation was avoided by carefully controlling the vacuum condition (keep the vacuum valve slightly open for the first two days to avoid rapid solvent evaporation and completely open for the rest of drying process). The total drying duration was determined by measuring SPEs dried at different time intervals using Thermogravimetric analysis (TGA). The weight loss profile of the SPE remained unchanged when drying time was above 5 days, indicating that this during was sufficient to remove the residue solvent or moisture. The resulting dry film was then transferred into a glovebox that purged with high purity Argon and stored at room temperature.

3.2.3 Preparation of GO/PEO nanocomposite and its SPEs

GO/PEO nanocomposite SPEs were fabricated using as two-step solution casting method as illustrated in Figure 3.1 and the formulation used in this study is listed in the table. First 66.75 mg GO was sonicated in 5 ml DMF in a glass vial using a Branson Ultrasonic bath for 90 min to yield a uniform GO dispersion. The solution was then mixed with PEO solution (500 mg in 5 ml DMF) and stirred at 45 °C under nitrogen for 10 hrs. $LiClO_4$ (O/Li molar ratio = 12) was added and stirred for another 5 hrs before casting into films. The concentration of GO is fixed to be 10 wt% of the total weight of the nanocomposite SPE.

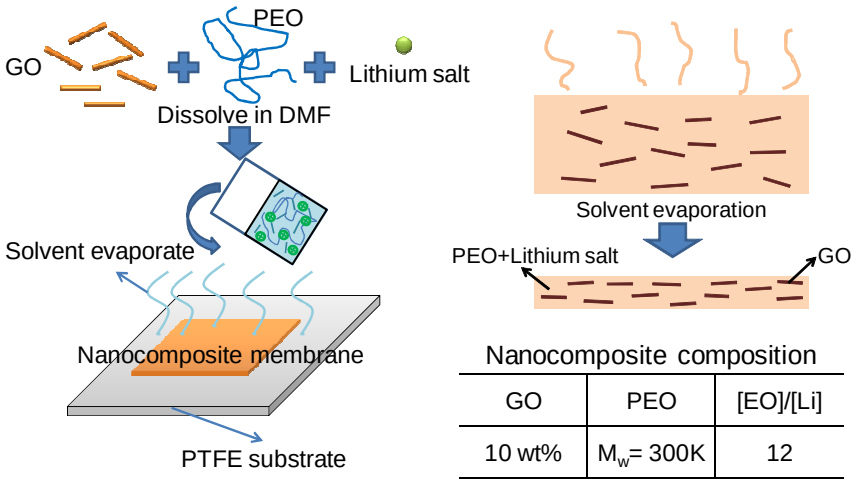

Nanocomposite composition

GO	PEO	[EO]/[Li]
10 wt%	M_w= 300K	12

Figure 3.1 Illustration of PEO/GO nanocomposite SPEs preparation.

3.2.4 PEO single crystals (PSCs) grown from dilute solution

PEO single crystals were grown from solution via a self-seeding method[198-204] as illustrated in Figure 3.2. 50 mg PEO (M_w ~ 300 kDa) was dissolved in 50 ml pentyl acetate at 80 °C for 10 min, and quenched to ~ –15 °C for 2 hrs to allow complete crystallization. The resulting PEO crystals were partially dissolved at appropriate seeding temperature (T_s) for 10 min to obtain crystal seeds. The seed solution was then brought to crystallization temperature (T_c = 20 °C) and isothermally crystallized for 1 day. T_s in this study was varied from 51 °C to 54 °C, and the resulting crystal size changes from 2 μm to 50 μm.

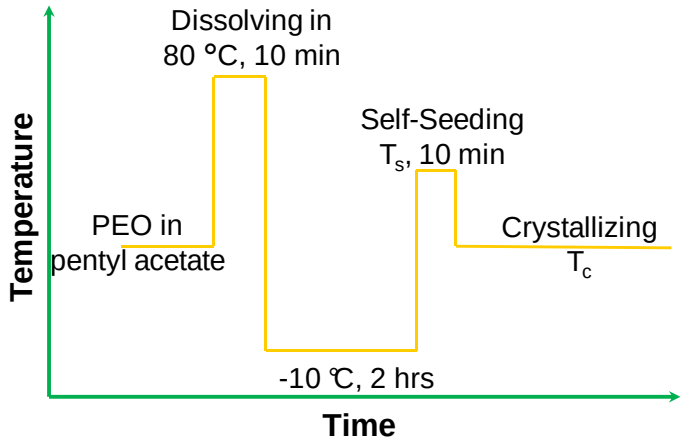

Figure 3.2 Temperature program of PEO single crystal growth from dilute solution using a self-seeding method.

3.2.5 Preparation of PSC-SPEs

To prepare PSC-SPEs, the single crystal suspension obtained using method described in section 3.2.4 was centrifuged at 3000 rpm for 3 min and washed for 4 times to remove uncrystallized polymers. The single crystal sediment was re-dispersed in a small amount of pentyl acetate, casted onto a PTFE petri dish, and slowly dried under vacuum at room temperature for 1 week to yield a uniform single crystal film with thickness ~10-20 µm. PEO single crystal SPEs were prepared by soaking the single crystal film in lithium salt pentyl acetate solutions for different time intervals. The SPE samples were dried under vacuum at room temperature for at least 5 days and weighed before and after to determine Li^+ to [EO] molar ratio. The PSC-SPE preparation process is illustrated in Figure 3.3.

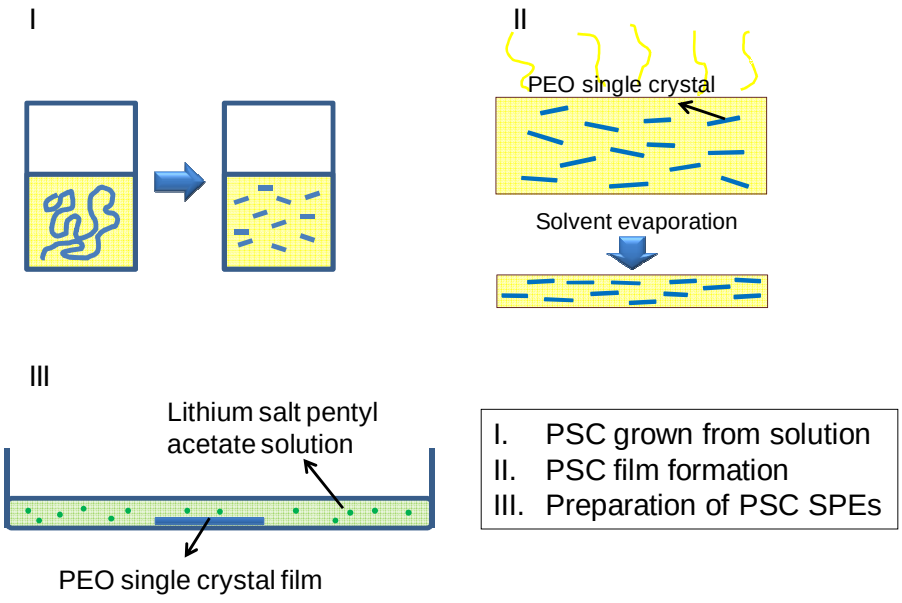

Figure 3.3 Schematic illustration of preparation of PSC-SPEs from PEO single crystal solutions.

3.3 Characterization techniques

3.3.1 Simultaneous 2D wide-angle X-ray diffraction (WAXD)/small-angle X-ray scattering (SAXS)

Both WAXD and SAXS techniques are based on the principle of coherent scattering from the electron density fluctuation of the sample. In brief, WAXD mainly detects the atomic structure of crystals with the lattice spacing below 1-2 nm and the condition for diffraction obeys the following Bragg's law:

$$2d\sin\theta = n\lambda \tag{3.1}$$

Where an integer n is the order of diffraction, d is the lattice spacing, 2θ is the diffraction angle and λ is the X-ray wavelength.

On the other hand, SAXS is recorded at very low angles (usually between 0.1 to 10°) and therefore captures much larger features in the structure with a length scale of 1 to 100 nm. The scattering vector q is correlated with d-spacing via Bragg's law and is defined as:

$$q = \frac{4\pi\sin\theta}{\lambda} \tag{3.2}$$

In this study, simultaneous 2D WAXD and SAXS experiments were performed using a Rigaku S-MAX 3000 SAXS system and instrument is shown in Figure 3.4. Similar setup has been used to study polymer crystallization and liquid crystalline block copolymers[205-208]. In this configuration, high energy X-ray beam is transmitted through a thin film sample (usually less than 1.5 nm for polymers), the main beam is blocked by a

beam stop while the scattered X-ray signals are collected onto a 2D detector. This is a powerful technique to probe the 3-dimensional structure and is especially useful for polymeric material with preferential orientations. The X-ray source is CuKα with a wavelength of 1.54Å. The incident beam is collimated by a 3-pinhole system and transmitted through the sample which is positioned between the X-ray source and the detector. An image plate with a 10 mm hole is placed in the chamber close to the sample holder where the x-ray diffracted at higher angles can be collected, while the SAXS patterns can be collected simultaneously using a 2D multi-wire area detector at a sample to detector distance of 1.5 meter.

The data is processed using a Matlab-based Graphical User Interface (GUI) capable of azimuthal integration and background subtraction. Silver Behenate standard with $q_{(001)} = 0.1076 Å^{-1}$ is used to calibrate the q vector of the SAXS and a glassy carbon standard is used for absolute intensity calibration. The d-spacing in WAXD is calibrated by silicone powder with $d_{(111)} = 3.1355$ Å. In-situ WAXD/SAXS is also feasible using a Linkam high temperature control stage with +/- 0.1 ℃ precision.

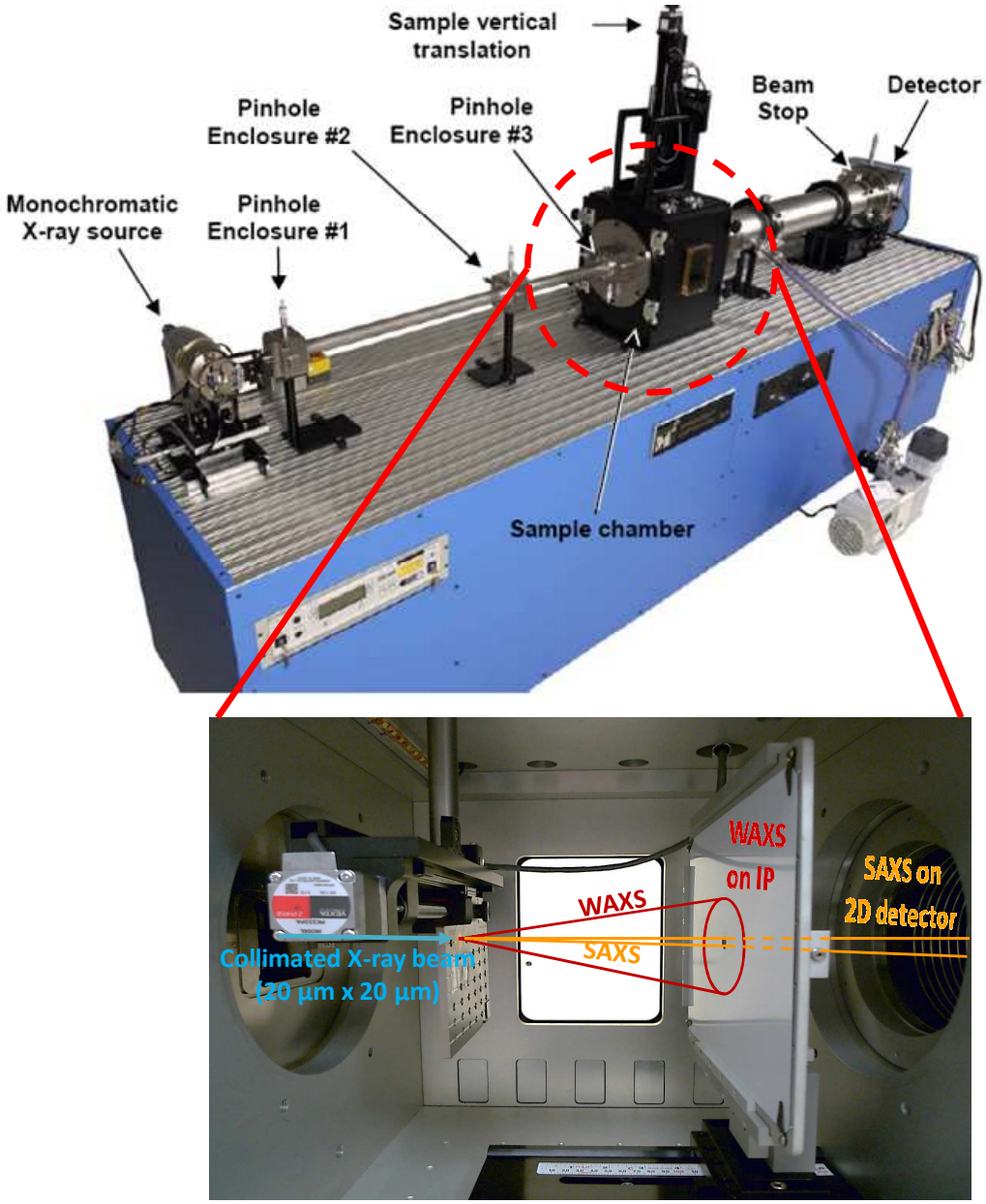

Figure 3.4 Photographs of a Rigaku S-MAX 3000 SAXS system

3.3.2 X-ray powder diffraction

X-ray powder diffraction (XRD) experiments were conducted using a Siemens D500 diffractometer with a CuKα wavelength of 1.54 Å. Thin film samples were

prepared and were scanned from 5° to 40° at a rate of 0.03 °/s. The powder diffraction was operated under reflection mode in which the X-ray beam was focused on the sample surface at an angle θ and the X-ray that was reflected was received at 2θ and the intensity was read by the detector. This technique gives higher intensity as the scanning area is much bigger compared with the 2D WAXD in transmission mode, but it does not provide the crystal orientation information in a 3D space.

3.3.3 Thermal analysis

Thermal analysis techniques such as differential scanning calorimetry (DSC) provide valuable information on the thermal behaviors of the materials. DSC is a technique that measures the heat flow rate difference into a substance and a reference as a function of temperature, while both the sample and reference are subjected to a controlled temperature program. Since both the sample and the reference are maintained at nearly the same temperature throughout the experiment, any phase transitions such as melting, crystallization, glass transition or reactions such as oxidation that absorb or release heat will be reflected on the heating or cooling curves. For semicrystalline polymers, the mass fraction crystallinity can be calculated using the following equation:

$$Crystallinity = \frac{\Delta H_f^{obs}}{\Delta H_f^{\circ}} \tag{3.3}$$

Where ΔH_f° is heat of fusion of 100% crystalline polymer and ΔH_f^{obs} is the experimentally measured heat of the fusion of the sample.

Two types of DSCs are available: power compensation and heat flux. Power compensation DSC is composed of two individual calorimeters for sample and reference. Both sample and reference are kept at the same temperature and the differential energy input is recorded as a function of program temperature. Heat flux DSC removes the thermocouple from the sample and uses a single furnace for both sample and reference; and the temperature difference (ΔT) is recorded as a function of block (furnace) temperature. Theoretically both types can give identical results; while each has its own advantages and disadvantages. Heat flux DSC has a flat and more reproducible baseline while power compensation DSC is more accurate for heat of fusion calculation and isothermal measurements.

A Perkin Elmer DSC7, which is a typical power compensation DSC, was used for measurements of melting temperature (T_m), crystallization temperature (T_c) and heat of fusion (ΔH) in this study. For PEO based SPEs, sample preparation was carefully handled to avoid any moisture uptake due to their hydroscopic nature. Samples of 5~6 mg were hermetically sealed in 40 µl aluminum pans in the glovebox prior to measurements. Samples were heated / cooled at 10 °C/min under N_2 if not specified. The DSC7 has a temperature range of -60 °C to 600 °C due to the limitation of the intracooler, therefore it is not able to measure the glass transition temperature (T_g) of PEO which exhibit a T_g around -65 °C.

A Mettler Toledo DSC822e/400 connected with a liquid nitrogen cooler (heat flux type DSC) is used in this case for T_g measurements. Glass transition temperature for semicrystalline polymer is difficult to measure since it can be broad and sometimes

smeared out. Therefore a hysteresis method was employed here to determine the T_g of PEO and PEO-based SPEs. The samples were cooled from 0 ℃ to -100 ℃ at 1 ℃/min and subsequently heated from -100 ℃ to 100 ℃ at 40 ℃/min, T_g was taken as the temperature at half height of ΔC_p during the heating scan.

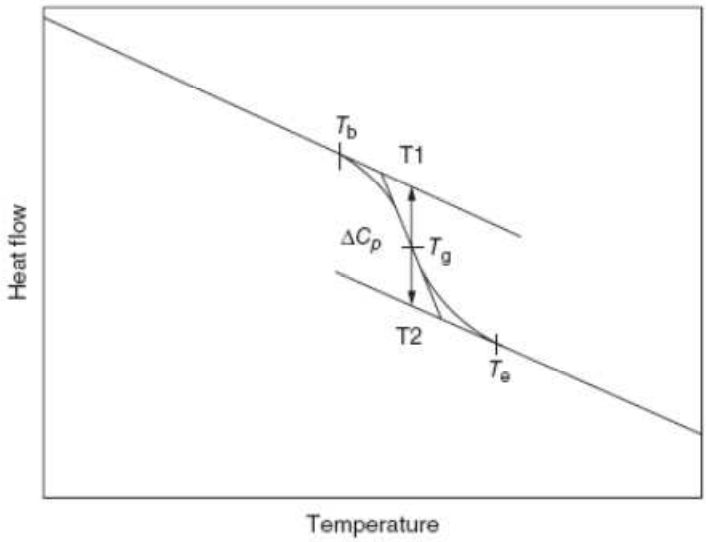

Figure 3.5 Define the glass transition temperature from a DSC measurement[209].

3.3.4 Microscope

Multiple microscopy techniques were employed in this study to better understand the materials morphology from micrometer scale down to nanometer scale. The techniques used include Optical Microscope, Transmission Electron Microscopy (TEM), Scanning Electron Microscopy (SEM), and Atomic Force Microscope (AFM).

Optical microscope images are collected using an Olympus BX-51 equipped with an Insight digital camera. Samples were typically prepared by spin coating onto a glass substrate. Phase contrast microscopy is suitable for observing polymer single crystals with large aspect ratio (usually a few microns in lateral direction and ~10 nm in thickness direction) that are grown from dilution solution. Polarized light microscopy (PLM) is useful to characterize spherulitic polymer crystals.

Electron Microscopy (EM) is a powerful technique to characterize the microstructures with very high resolution compared with optical microscope. Electrons are accelerated at several tens or hundreds kV and focused with a series of electromagnetic lenses under high vacuum (10^{-4} to 10^{-13} mbar). When high energy coherent electron beam interacts with the specimen as it passes through, various signals are generated and can be collected for different analysis (as shown in Figure 3.6).

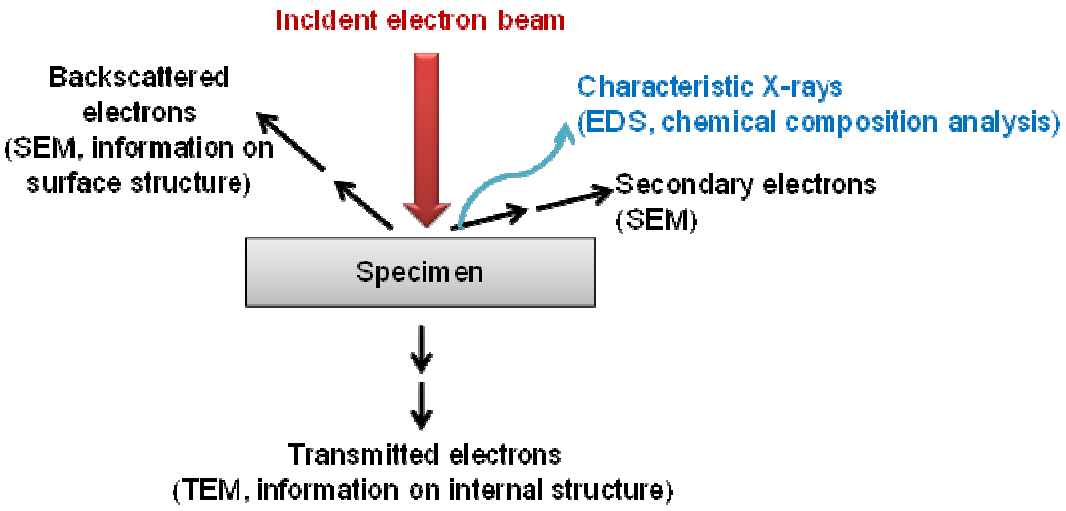

Figure 3.6 Schematic of the interaction between incident electron beam and the specimen.

TEM detects the transmitted electron, therefore required the thickness of the specimen to be less than 100 nm. The transmitted electrons are focused to the back focal point below the objective lens; two types of images can be formed depending on the position of the objective aperture. Removal of all incoherently and coherently scattered electrons results in a bright field image; while blocking of all transmitted and incoherently scattered electrons gives a dark field image. The final magnified image can be collected onto either a phosphorescent screen or a CCD camera, which provides information on the internal structure of the transmitted specimen. TEM was performed on a JEOL JEM2100 microscope with an accelerating voltage of 200 kV in this study. Samples were drop-casted onto carbon coated nickel grids and dried overnight. Elemental analysis was conducted by an EDS detector attached to the TEM.

In a SEM, electron beam with energy range from 0.2 keV to 40 keV bombards on the sample surface and interacts with the atoms at or near the sample surface. Secondary electrons are collected into the detector and high resolution images of the surface can be produced. SEM was performed using a Zeiss Supra 50VP to determine the cross-section morphology of PEO single crystal films in this study. The films were cryo-fractured, vacuum dried, and sputtered with platinum for 20 s before testing.

Other than TEM or SEM, which is commonly used for imaging nanostructure with ~ 100,000 x or higher magnification, AFM can provide more accurate information on the depth profile of the surface features with nanometer scale resolution. AFM experiments were conducted using a Nanoscope IIIa (Digital Instruments/Veeco) tapping mode AFM at 0.5 Hz scanning frequency in this study.

3.3.5 Electrochemical Impedance Spectroscopy (EIS)

3.3.5.1 A.C. Ionic conductivity measurement

Room temperature ionic conductivities were measured in Argon purged glovebox using custom-made cells connected to a Princeton Applied Research Parstat 2273 Potentiostat. In-plane conductivity $\sigma_{//}$ was measured using a four-parallel-electrode method with two outer working electrodes and two inner sensing electrodes lying on the same side of the sample as shown in Figure 3.7. The a.c. impedance spectroscopy was collected from 0.1 Hz to 1 MHz at 500 mV. Ionic conductivity was calculated using the following equation:

$$\sigma_{//} = \frac{L}{w \times t \times R} \tag{3.4}$$

Where L is the distance between two inner sensing electrodes and is 2.5 mm in this study; w and t are the width and thickness of the sample, respectively. The bulk resistance of the electrolyte R is determined from the low frequency plateau in the Bode plot of real impedance z as a function of frequency (the result is indistinguishable with that obtained from the semicircle fit method in Nyquist plot).

Through-plane conductivity $\sigma_{\perp}$ was measured using a two-electrode setup with the sample film sandwiched between two stainless steel electrodes. The ac impedance spectroscopy was collected from 0.1 Hz to 1 MHz at 10 mV. The conductivity was calculated using the following equation:

$$\sigma_{\perp} = \frac{L}{R \times A} \tag{3.5}$$

Where L is the sample thickness, the typical electrolyte membrane thickness in this thesis range from 10 μm to 150 μm; A is the area of the electrode and is 0.367 cm^2 for the setup used in this study. The bulk resistance R is read as the intersection of the semicircle fit with axis of real impedance part in the Nyquist plot (also consistent with the result obtained from the high frequency plateau in the real impedance plot).

The actual experimental setups of these two configurations are shown in Figure 3.7. Two to five measurements were performed for each sample and experimental error was within a few percentage of the mean value. Temperature-dependent ionic conductivity was performed using a Mettler Toledo hot stage with a temperature accuracy of less than 0.1°C.

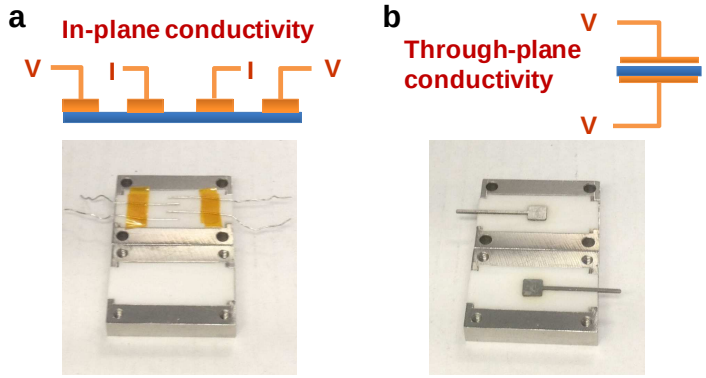

Figure 3.7 Schematic and photographs of 4-parallel-electrode and 2-electrode setups for ionic conductivity measurements.

3.3.5.2 Lithium transference number measurement

Lithium transference number is defined as the fraction of current across a reference plane that is carried by the lithium cation or cation containing species and can be expressed as below[210]:

$$t_+ = \frac{i_+}{i_+ + i_-} = \frac{i_+}{i} \tag{3.6}$$

Where i_+, i_- are the partial currents carried by cation and anion constituents respectively, and i is the total current. In this study, lithium transference number was measured using an electrochemical method first developed by Vincent and Bruce[211-213]. A symmetrical *Li* | polymer electrolyte | *Li* cell (as shown in Figure 3.8) was polarized by a small, constant potential across the electrodes and the response of cell current was monitored until a steady state current was reached. A typical current response as a function of time is shown in Figure 3.9a. The initial current drop is due to I) the concentration gradient that is established to stop the net motion of the anion constituents; II) the potential reduction at the electrode/electrolyte interface due to a passivating layer formation.

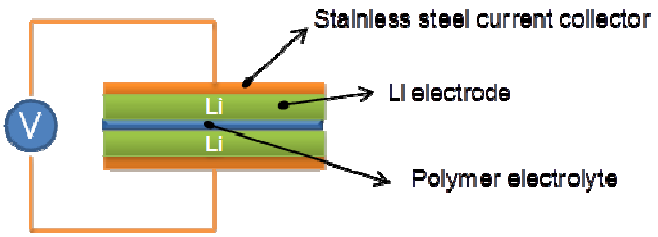

Figure 3.8 Schematics of the cell assembly for lithium transference number measurement.

The a.c. impedance was measured before and after the d.c. polarization in order to determine the change of the electrode resistance. Typical a.c. impedance plot is shown in Figure 3.9b and can be modeled by the equivalent circuit in the inset. R_1 and C_1 are related to the passivating layer formation at the electrode/electrolyte interface while R_2 is the bulk resistance of the electrolyte.

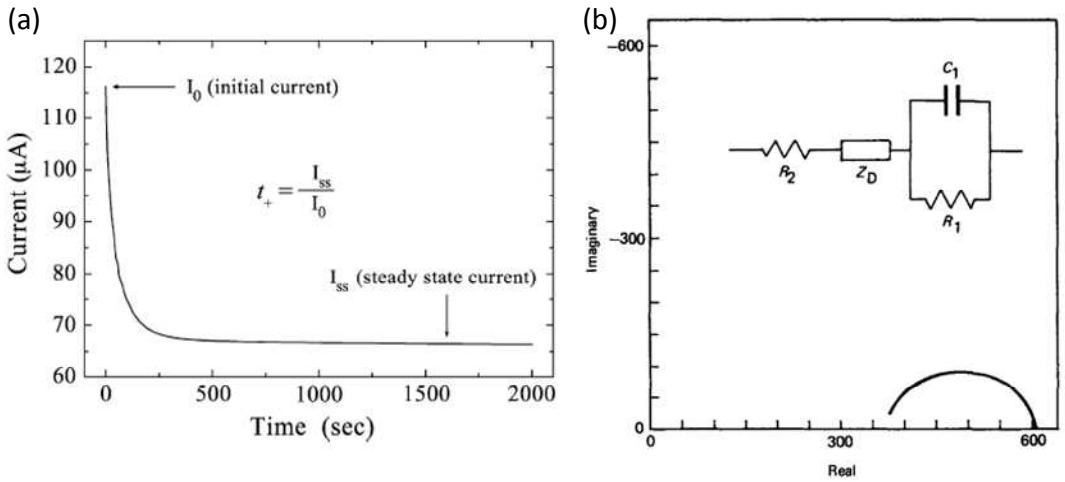

Figure 3.9 (a) A typical current profile under 10 mV polarization potential, adopted from ref.[214]; (b) A typical a.c. impedance plot of a symmetric Li | polymer electrolyte | Li cell, inset is the equivalent circuit.

The lithium transference number can be calculated using the following equation, a different nomenclature from Vincent and Bruce's original paper is used here for better illustration:

$$t_+ = \frac{I_s\left(\Delta V - I_0 R_i^0\right)}{I_0\left(\Delta V - I_s R_i^s\right)} \tag{3.7}$$

The equation is further modified by Abraham *et al.*[215] to include the change of electrolyte resistance and is expressed as follows:

$$t_+ = \frac{I_s R_e^s}{I_0 R_e^0}\left[\frac{\Delta V - I_0 R_i^0}{\Delta V - I_s R_i^s}\right] \tag{3.8}$$

I_0 — Initial current;

I_s — steady state current;

ΔV — potential across the electrodes

$R_e^{\,0}$ — initial resistance of the electrolyte;

$R_e^{\,s}$ — steady state resistance of the electrolyte;

$R_i^{\,0}$ — initial resistance of the passivating layers at the Li electrode/electrolyte interface;

$R_i^{\,s}$ — steady state resistance of the passivating layers on the Li electrode/electrolyte interface.

CHAPTER 4: **ION TRANSPORT IN SEMICRYSTALLINE PEO SPES PREPARED VIA SOLUTION CASTING METHOD**

4.1 Introduction

In semicrystalline PEO SPEs, the crystalline PEO lamellae act as impermeable barrier that dispersed in the amorphous conducting matrix. Therefore, the ion transport in this case largely relies on the continuity of the amorphous phase, which is sensitive to the thermal history and crystalline morphology (for example, crystallinity, crystallite size, crystalline lamellae thickness and orientation.) Creating continuous amorphous ion conducting channels by controlling the crystalline morphology is critical to obtain considerable room temperature ionic conductivity.

In this chapter, a semi-crystalline PEO SPE containing $LiClO_4$ salt was prepared via a controlled solution casting method. During the slow solvent evaporation process, the PEO crystallized into flat on lamellae with chain preferentially aligned parallel to the film normal. Moderate degree of crystal orientation was observed, which led to ~10 fold difference between the conductivity measured along and perpendicular to the crystal surface. The results suggest that the tortuosity effect on ion conduction due to PEO crystal orientation is not trivial and the ion conduction is favored along the PEO crystal surface.

4.2 Preparation of solution cast PEO SPEs

PEO with a number averaged M_w ~ 300 kDa was chosen in this study in order to maintain sufficient mechanical integrity of the SPE. This molecular weight is significantly higher than the critical M_w of 3.2 kDa, above which the chain end effect is negligible and the cation mobility is independent on PEO M_w. lithium perchlorate ($LiClO_4$) was selected as a prototype salt due to its thermal stability, electrochemical stability, and high ionic conductivity at elevated temperatures[101]. More importantly, the phase diagram of PEO-$LiClO_4$ electrolyte has been well established and less complicated compared with some other Li salt systems, which allows more comprehensive study of crystallization effect on ion conduction in semicrystalline SPEs[111]. O/Li molar ratio was fixed to be 12, at which ratio the PEO-$LiClO_4$ electrolyte shows a conductivity maximum at both room temperature[111] and elevated temperatures[62]. The SPE is denoted as $P(EO)_{12}$:$LiClO_4$.

To prepare $P(EO)_{12}$:$LiClO_4$ SPEs with controlled crystal orientation, a slow solvent evaporation method was used, detailed in section 3.2.2. In brief, PEO (300 kDa) and $LiClO_4$ with desired stoichiometry were dissolved in anhydrous DMF solvent. The solution was poured into a petri dish and underwent slow evaporation over a period of 5-7 days at 45 °C. The resultant SPE membranes have an average thickness of ~ 100 to 200 µm. The drying temperature and duration were carefully selected not only to completely remove solvent and moisture but also to avoid the formation of PEO_6:$LiClO_4$ crystalline complex phase which forms at much longer annealing time. The membrane was then

transferred into an Argon purged glovebox and stored at room temperature for 1 week before EIS measurements.

4.3 Ionic conductivity of solution cast PEO SPE

Ionic conductivity was measured in a dry Argon filled glove box using home-build cell that fits in a Mettler-Toledo hot stage, which allows in-situ conductivity measurement with a temperature control better than 0.1 °C. Ionic conductivities were measured along two directions, namely in-plane $\sigma_{//}$ (along the film surface) and through-plane $\sigma_{\perp}$ (along the film normal), and the setups for each configuration is described in details in section 3.3.5. Room temperature conductivities were first measured and the measurements were repeated using 3 fresh made samples.

The two-parallel-electrode configuration for through-plane ionic conductivity measurement is most commonly used in solid electrolyte research (Figure 4.1a). The Nyquist plot (Imaginary impedance vs. real impedance) for a typical polymer electrolyte measured between two ion-blocking electrodes is featured by a single semicircle at high frequency range with a slanted line at the low frequency range[76] as shown in Figure 4.1b, which can be modeled by an equivalent circuit of a constant phase element of the electrode/electrolyte interfaces (CPE_{int}) in series with a parallel combination of electrolyte resistance and pseudo-capacitance (CPE_{el})[125] (Figure 4.1c). In semicrystalline PEO SPEs, depressed semicircle instead of a perfect semicircle was often observed due to the inhomogeneity of the electrolyte and have be fitted into much complicated equivalent circuit[65, 216].

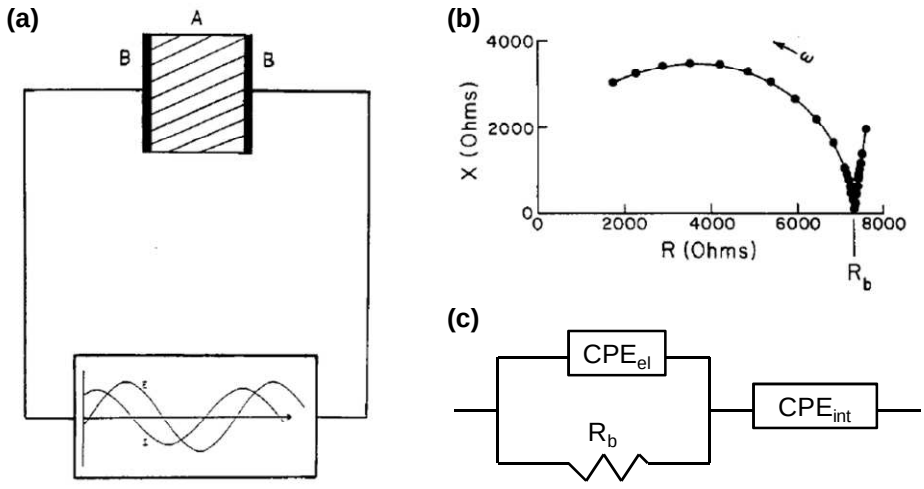

Figure 4.1(a) Schematic of an a.c. impedance measurement using two-parallel-electrode configuration; (b) Nyquist plot of a typical polymer electrolyte measured between two Pt electrodes. R_b represents the bulk resistance of the electrolyte sample; (c) The corresponding equivalent circuit model. Figure (a) and (b) are reproduced from ref.[76]

The Nquist plot (Imaginary impedance vs. real impedance) and Bode plot (Real impedance vs. frequency) of as cast $P(EO)_{12}$:$LiClO_4$ measured from through-plane direction at room temperature are shown in Figure 4.2. Nyquist plot exhibits a single semi-circle that is slightly deformed at high frequency and a slanted spur at low frequency, which is commonly found in semicrystalline SPEs; while an impedance plateau in the medium frequency range is shown in the Bode plot. In this case, the bulk resistance of the electrolyte was calculated as the intersection at *x*-axis of the fitted semicircle at high frequency side, which is consistent with the resistance read from the plateau between 10-100 Hz in the Bode plot.

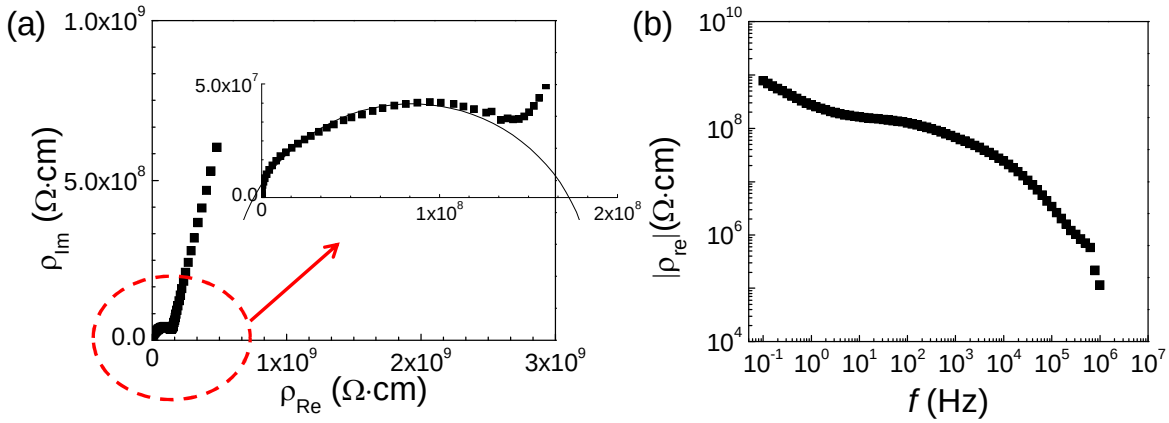

Figure 4.2 (a) Nyquist plot (black line represents the fitted semi-circle) and (b) Bode plot of as cast $P(EO)_{12}$:$LiClO_4$ SPE, measured from through-plane direction at room temperature.

In-plane configuration using a 4-parallel-electrode setup under a small a.c. perturbation is not common but has been reported by a limited number of studies. Zhou *et al.* had used a standard four-electrode method to measure the in-plane ionic conductivity of a hot pressed PEO-$LiCF_3SO_3$ electrolyte[217]. Two inner wires were used as working sensor and reference electrodes while the outer working and counter electrodes were made of stainless steel sheets. A custom made 4-electrode PTFE coated stainless steel cell had been employed by Elabd and co-workers to study the ionic conductivity of polymerized ionic liquids (PIL) block copolymers[218-222]. However, no detailed information on the interpretation of the impedance plots was provided in these studies.

In the present work, Nyquist and Bode plot of as cast $P(EO)_{12}$:$LiClO_4$ measured from in-plane direction at room temperature (shown in Figure 4.3) are quite different from that of through-plane measurements. The Nyquist plot shows a distorted semicircle with absence of the slanted spur; while the impedance plateau moves to much lower

frequency in the Bode plot. The impedance spectrum difference between these two configurations can be attributed to the electrode geometry and sample dimensions. The absence of the spike in the in-plane Nyquist plot is likely due to the small contact area between the sensing Pt wire electrodes and the electrolyte sample that reduces the EDL effect. Nevertheless, the electrolyte bulk resistance in this configuration is read from either the intersection of the semi-circle fit with axis of real impedance part in the Nyquist plot or the low frequency plateau in the real impedance plot. No major errors have been found in the measurement results due to the difference in the electrode configurations as the conductivity values for isotropic SPEs measured from in-plane and through-plane directions is minimum (will be covered in the following discussion).

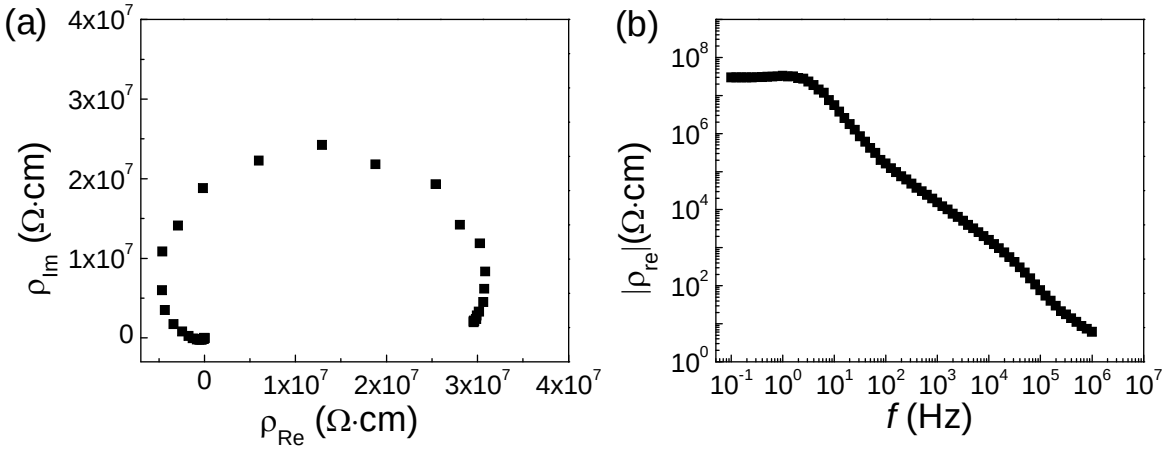

Figure 4.3 (a) Nyquist plot and (b) Bode plot of as cast $P(EO)_{12}$:$LiClO_4$ SPE, measured from in-plane direction at room temperature.

Figure 4.4 shows both in-plane and through-plane ionic conductivity ($\sigma_{//}$, $\sigma_{\perp}$) during the first heating scan at 1 °C/min for the as cast $P(EO)_{12}LiClO_4$ electrolyte film (open square and triangle). To quantitatively analyze the data, we introduce the

conductivity anisotropy factor $\sigma_{//}/\sigma_{\perp}$, which is defined as the ratio between in-plane and through-plane ionic conductivity of the sample, and it is also plotted in Figure 4.4 (black solid squares). Both $\sigma_{//}$ and $\sigma_{\perp}$ increase with increasing temperature and exhibit a conductivity "knee" around 60 °C which is characteristic of the melting of PEO crystals.

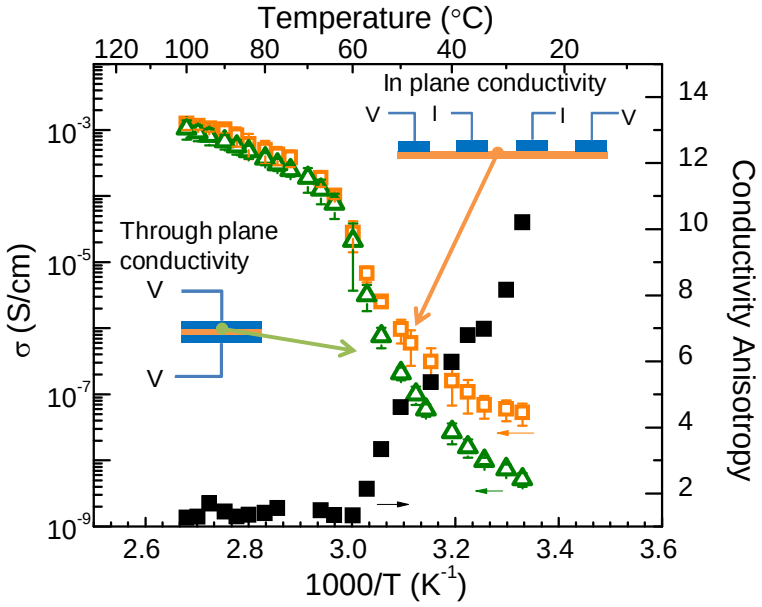

Figure 4.4 Temperature dependent ionic conductivity for solution cast $P(EO)_{12}$:$LiClO_4$ SPEs that stored at room temperature for 10 days. All curves represent first heating scans from room temperature to 100 °C.

At temperatures below T_m of PEO, $\sigma_{//}$ appears consistently greater than $\sigma_{\perp}$ and the anisotropy factor reaches ~ 10 at room temperature. This moderate conductivity anisotropy indicates that PEO crystallization should play a role and it is postulated that the anisotropic conductivity arises from PEO crystal orientation. The anisotropy factor remains at a relatively constant value of ~ 1.2 above 60 °C, where PEO is a homogeneous melt and the ion conduction is isotropic along all directions. The 1.2 fold difference

between in-plane and through-plane conductivity can be ascribed to the electrode setup difference as the lead and contact resistance need to be taken into account in the through-plane setup while they can be eliminated in the in-plane configuration. However, the setup difference can be considered as insignificant and the 10 times conductivity anisotropy observed at room temperature mush origin from the unique structure of the semicrystalline PEO SPE.

4.4 Correlating conductivity anisotropy with PEO crystalline morphology

Morphological characterizations of as cast $P(EO)_{12}$:$LiClO_4$ were conducted in order to better understand the cause of the observed ionic conductivity anisotropy. Figure 4.5 shows the crystalline morphology of both as cast PEO without lithium salt doping and $P(EO)_{12}$:$LiClO_4$ SPE under polarized light microscope. The microscope image reveals that $P(EO)_{12}$:$LiClO_4$ SPE crystallizes into spherulite but with a less regular shape and coarsened structures at the spherulite interiors and boundaries as a result of strong PEO-Li interactions during the crystallization process (Figure 4.5 b).

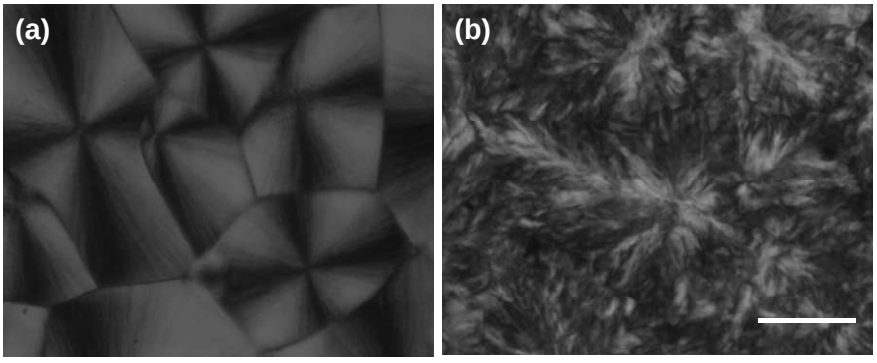

Figure 4.5 Polarized light microscopy images of (a) pure PEO film without salt doping; (b) $P(EO)_{12}$:$LiClO_4$ SPE. Samples for microscope observation were prepared by solution casting a

small amount of DMF solution onto glass slide and drying at 45 °C overnight prior to measurements. Scale bar is 50 μm.

2D WAXD provides more detailed information on the crystal structure and orientation of the electrolyte membrane. For a thin film electrolyte as illustrated in Figure 4.6, *z*-axis is the film normal and is defined as through-plane direction; and *x or y*-axis is defined as in-plane direction. WAXD patterns were measured from two directions: in-plane (x-ray beam parallel to *x*-*y* plane) and through-plane (x-ray beam parallel to *z*-axis) and are displayed in Figure 4.6. At room temperature, PEO electrolyte film does show noticeable preferred orientation, as indicated by a pair of equatorial PEO (120) arcs from the in-plane WAXD pattern. Only isotropic (120) ring is observed from the through-plane pattern, suggesting the *c*-axis of the polymer chain is preferentially aligned perpendicular to the film surface. The azimuthal profiles of the (120) plane for both in-plane and through-plane measurements at room temperature are shown in Figure 4.7a. The Herman's orientation factor of PEO (120) plane f_{120} is calculated to be ~ 0.35 from in-plane direction using the following equations:

$$f_{120} = \frac{3\cos^2\theta - 1}{2} \tag{4.1}$$

$$\cos^2\theta = \frac{\int_0^{\pi/2} I_{120}(\theta)\cos^2\theta \sin\theta d\theta}{\int_0^{\pi/2} I_{120}(\theta)\sin\theta d\theta} \tag{4.2}$$

For PEO (120) plane, θ is defined as the angle between (120) plane normal and the membrane surface plane. At 100 °C, the polymer is in its molten state and the

polymer chains are all randomly oriented, as suggested by the isotropic rings in 2D WAXD patterns in Figure 4.6 and the flat Azimuthal profiles curves integrated between 17 and 20° of 2θ from both in-plane and through-plane directions (Figure 4.7b).

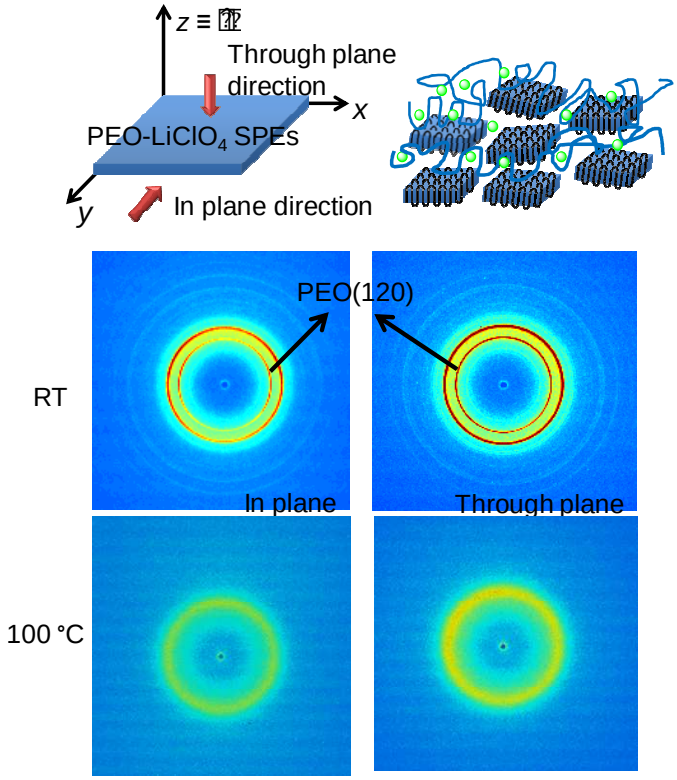

Figure 4.6 2D WAXD patterns of as cast $P(EO)_{12}$:$LiClO_4$ from both in-plane and through-plane directions at room temperature and 100 °C. Schematic shows the PEO lamellae orientation within the SPE film.

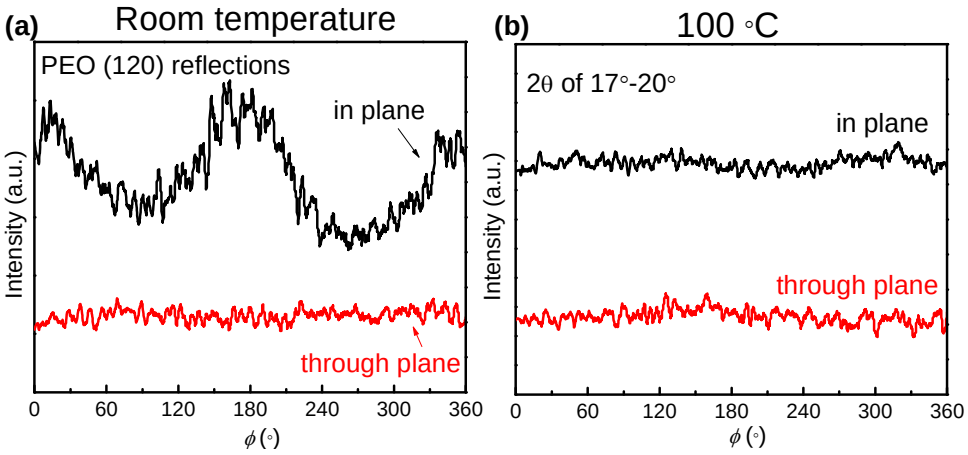

Figure 4.7 (a) Azimuthal profiles of PEO (120) reflections from in plane (black) and through plane (red) directions at room temperature; (b) Azimuthal profiles of the ring between 2θ of 17° to 20° at 100 °C.

Azimuthal integrations of 2D WAXD patterns from both in-plane and through-plane directions at room temperature show identical diffraction peak positions that are characteristic of PEO monoclinic crystal structure (Figure 4.8). The peak at 2θ = 19.15° refers to reflection from PEO (120) plane; and the peak at 2θ = 23.3° can be assigned to the overlapping reflections from PEO (032), $(\bar{1}32)$, (112), $(\bar{2}12)$ planes[223]. Meanwhile four peaks at 2θ = 10.3°, 16.6°, 14.9°, 22.4° that are characteristic of PEO_6:$LiClO_4$ crystalline complex are absent[111]. Since the crystallization kinetics of PEO_6:$LiClO_4$ crystalline complex is very slow, only crystalline PEO and amorphous PEO-lithium phases co-exist in the as cast $P(EO)_{12}$:$LiClO_4$ SPE during the time frame of any measurements.

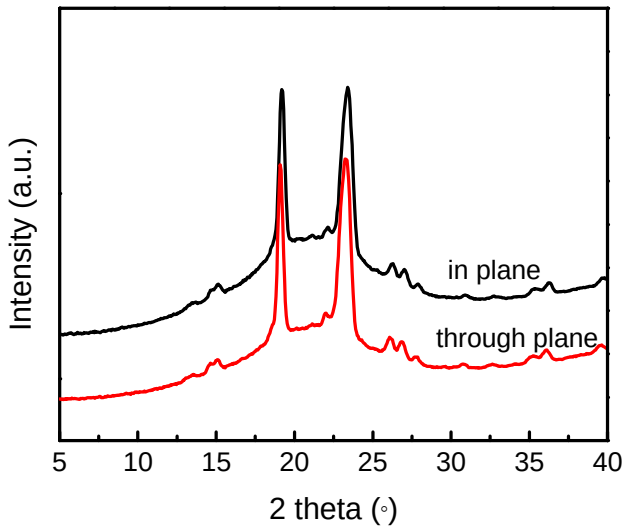

Figure 4.8 Integrations of 2D WAXD patterns from in plane (black) and through plane (red) directions at room temperature for as cast $P(EO)_{12}$:$LiClO_4$ SPE.

The consequent cooling scans of conductivity measurements at 1 °C/min immediately after the first heating for $P(EO)_{12}$:$LiClO_4$ SPEs from both in-plane and through-plane directions are shown in Figure 4.9a. The in-plane and through-plane cooling curves overlap and both show a sharp conductivity drop at around 35 °C, which corresponds to the onset of PEO crystallization upon cooling. During the relatively fast melt crystallization process, the PEO crystals tend to grow in a more random way since there is no confinement on the crystallization, as confirmed by the isotropic PEO (120) rings from both in-plane and through-plane WAXD patterns shown in Figure 4.9b. The isotropic structure is consistent with the overlapping of in-plane and through-plane conductivity curves during the cooling scan and it further confirms the hypothesis that the anisotropy observed at room temperature from the first heating scan arises from crystal orientation.

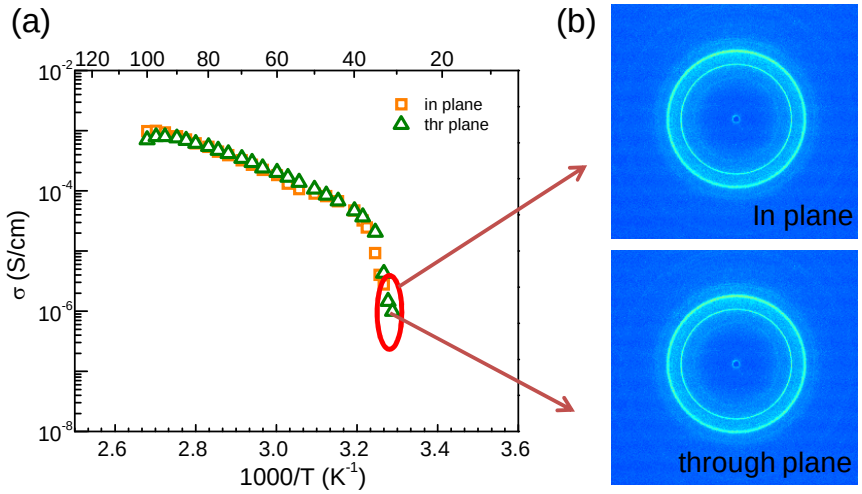

Figure 4.9 (a) Subsequential cooling scan at 1 °C/min for solution cast $P(EO)_{12}$:$LiClO_4$ SPEs right after the first heating scan; (b) 2D WAXD patterns of $P(EO)_{12}$:$LiClO_4$ SPEs measured at 30 °C from in plane (top) and through-plane direction (bottom), data were collected right after samples were cooled from 100 °C to 30 °C.

4.5 Discussion

The 2D WAXD combined with conductivity measurements along two orthogonal directions suggests there is a strong correlation between PEO crystal orientation and ion conduction. At low temperature, PEO lamellae surface preferentially aligned parallel to the membrane surface; such orientation significantly affects $\sigma_{\perp}$, because ions cannot transport through lamellar crystals and it took more tortuous pathway for the ions to diffuse from one electrode to the other through the membrane, while the ion conducting path along the in-plane direction is less impacted (as illustrated in Figure 4.10).

If one considers the semicrystalline PEO SPE at the room temperature as a classical two-phase model consisting amorphous conducting and crystalline insulating

phase, the morphology of the sample largely mimics many other types of solid electrolytes including block copolymer films[22, 38-40, 43], porous polyolefins[224-225], holography directed SPEs[132], etc. For example, by synthesizing BCPs consisting of PEO and a high modulus segment (such as polystyrene, PS), it has been demonstrated that exploiting BCP phase separation at ~10-100 nanometer scales, ionic conducting channels can be formed in the PEO domains, while PS provides high modulus of the film. The present experiment demonstrate that one can treat the crystalline domain as the load bearing component (mimicking PS) while the amorphous domains provide ion conducting channels. Further, tailoring lamellar structure can further tune ion conducting path. Carefully designed structure can therefore lead to mechanically robust film without significantly sacrificing ion conductivity.

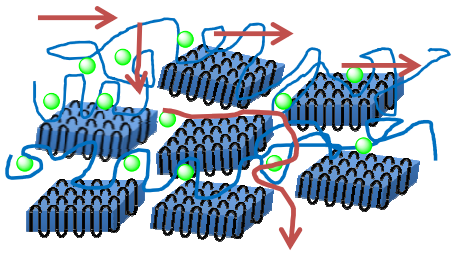

Figure 4.10 Schematic illustration of ion transport along and across PEO crystalline lamellae.

4.6 Summary

In this chapter, a $P(EO)_{12}$:$LiClO_4$ SPE had been prepared using a controlled solution casting method. During the slow solvent evaporation process, polymer chains tend to partially orient with the normal of PEO (120) plane parallel to the film surface.

The moderate crystal orientation results in anisotropic ionic conductivity at room temperature with $\sigma_{//}$ nearly 10 times higher than $\sigma_{\perp}$. The conductivity anisotropy is absent once the SPEs were cooled from melts to room temperature at 1 °C/min. The structure-conductivity correlation observed in this chapter clearly suggests that the crystal orientation is one of the key factors to affect the overall room temperature conductivity. The two-phase semi-crystalline PEO based SPEs are morphologically similar to BCP system. The closely packed PEO crystalline lamellae provide adequate mechanical support and can act as templates to direct ion transport in the inter-lamellae amorphous regions. The ion conducting channel is expected to be optimized if the PEO crystal orientation can be further improved. And further effort will be focused on controlling the PEO crystalline morphology in order to enhance conductivity anisotropy.

CHAPTER 5: **ENHANCED CONDUCTIVITY ANISOTROPY IN A NANOCOMPOSITE ELECTROLYTE**

5.1 Introduction

In our preliminary approach discussed in Chapter 4, only moderate crystal orientation (f_{120} = ~ 0.35) was achieved simply by slow solvent evaporation, it is speculated that the conducting channel can be further optimized if the degree of PEO crystal orientation can be improved. Several strategies have been previously used to control PEO crystal orientation by imposing a geometric confinement to the crystallization, including PEO based block copolymer and nanolayered polymer blends with one PEO containing phase. Zhu *et al.* investigated the confined PEO crystallization in a shear-aligned poly(ethylene oxide)-*block*-polystyrene (PEO-*b*-PS) diblock copolymer with lamellar morphology[231-232]. The study had shown that when the BCP crystallized at temperatures above 35 °C, PEO block adopted a homeotropic crystal orientation (crystal normal is parallel to the lamellae normal) within one-dimensionally confined lamellae spacing less than 10 nm.

Similarly, Baer and coworkers had developed a layer-multiplying coextrusion method to obtain thousands of alternating polymer nanolayers with PEO as one phase and a glassy polymer as the second phase. And the method was demonstrated to be successfully in several systems, such as poly(ethylene-*co*-acrylic acid) (EAA)/PEO blends[233] and polystyrene (PS)/PEO blends[234-235]. When the thickness of PEO layer was reduced to be below 25 nm, PEO crystallized as single lamellae with a large aspect ratio. This idea was initially aimed at inhibiting small gas molecule permeation and improving

the barrier properties of the film, but the same concept would also be applied to the case of polymer electrolyte, where the ions can be treated as small molecules that diffuse through the amorphous matrix and the lamellae crystals that oriented perpendicular to the diffusion direct would impose a much tortuous pathway.

In this chapter, a nanocomposite approach has been explored in order to achieve higher degree of structural and conductivity anisotropy. Two dimensional Graphene oxide (GO) nanosheets, which is a derivative of graphene, is ideal to be used as the nanofiller due to its high aspect ratio, high young's modulus and ability to be dispersed in common organic solvents. In addition, relatively large quantity of single or a few layer GO nanosheets can be easily obtained through a well-known oxidation-reduction reaction from natural abundant graphite[196, 226-230]. The purpose of introducing GO nanosheets into PEO matrix is two-fold: Firstly, GO nanosheet itself can act as an impermeable barrier to confine the ion transport. Secondly, aligned GO nanosheets can be used to template PEO crystal orientation, which further directs the ion conducting channels.

Compared with the BCP approach, in which case the phase-separated morphology is dependent on the volume fraction of each block and external shear force is required to obtain the long range alignment, the advantage of using 2D GO nanofiller is that the morphology is less dependent on the composition and a wide range of PEO molecular weights and GO fraction can be used to fabricate the nanocomposite SPEs. And compared with PEO/glassy polymer multilayer co-extrusion, the processing of GO/PEO nanocomposite is relatively simple and the GO can be easily aligned during the deposition process.

GO/PEO nanocomposite SPEs were prepared using a similar slow solvent evaporation method as described in Chapter 3. GO nanosheets are readily aligned parallel to the film surface under controlled evaporation condition and the confinement of GO at nanoscale has demonstrated significantly enhancement of PEO crystal orientation compared with previous discussed solution cast PEO SPEs. The conductivity anisotropy is correlated with the nanocomposite morphology and the results are compared with those of the semicrystalline PEO SPEs discussed in Chapter 4.

5.2 Preparation and characterization of GO/PEO nanocomposite electrolyte

Graphene oxide was synthesized by the oxidation of natural flake graphite using a modified Hummer's method[236] followed by exfoliation through sonication in solvent. A schematic chemical structure of graphite oxide is shown in Figure 5.1a and it is consists of stacks of graphene oxide layers. The *d*-spacing of (001) plane increases from 0.34 nm for graphite to 0.96 nm for graphite oxide based on XRD result (Figure 5.1 b). C/O molar ratio of 1.3 for graphite oxide was determined by elemental analysis and Karl Fischer Coulometry. The results indicate a disruption of the sp^2 conjugated carbon structure and the incorporation of additional oxygen containing functional groups after oxidation. Graphite oxide can be easily dispersed in aqueous and a selected number of commonly used organic solvent such as DMF to yield exfoliated single or a few layer GO nanosheets. TEM micrograph of exfoliated GO sheets is shown in Figure 5.1 c.

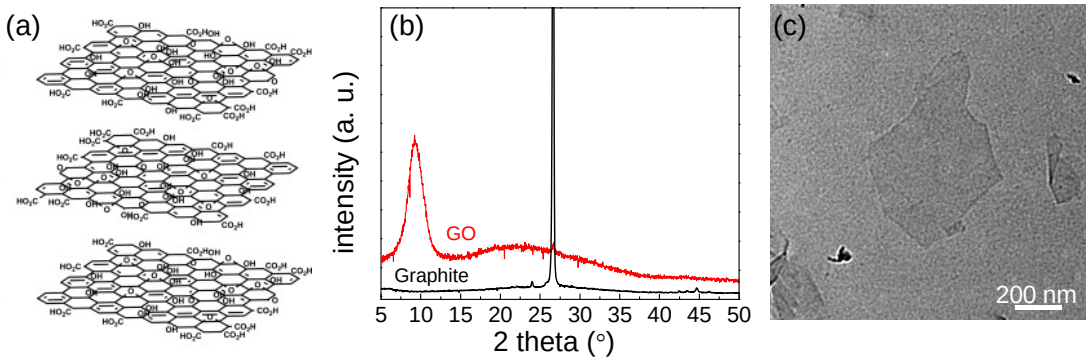

Figure 5.1 (a) Schematics of the graphite oxide structure, modified from ref [237]; (b) X-ray powder diffraction of GO and graphite; (c) TEM image of exfoliated GO nanosheets.

The concentration of GO directly affects the nanocomposite membrane's structure anisotropy, and therefore the ionic conductivity. The criteria to determine the concentration of GO in the final SPE is: (i) the GO concentration is sufficient to impose a nanoconfinement in order to restrict PEO crystal orientation; (ii) No significant nanoparticles aggregation; (iii) PEO should remain the major phase in the nanocomposite so that the effective conducting phase is not significantly reduced.

A series of GO/PEO nanocomposites were first prepared using a solution blending method as described in Chapter 3. Figure 5.2 shows the 2D in-plane WAXD patterns of a series of GO/PEO nanocomposites with and without lithium salt doping. For GO/PEO nanocomposite without lithium salt, the degree of PEO crystal orientation gradually increases with increasing GO content as the PEO (120) diffraction pattern changes from isotropic ring to highly anisotropic arcs from 0 to 10 wt%, and the Herman's orientation factor f_{120} increases and reaches a plateau of ~ 0.8 above 5 wt% of GO content. The addition of lithium salt results in a decrease of PEO crystallinity as more amorphous scatterings between the crystalline rings are observed in Figure 5.2e and f.

And the degree of PEO orientation for the nanocomposite SPEs slightly decreases compared with nanocomposite without salt doping possibly due to the interference of lithium salt with the polymer chain during the solution casting process. The highest degree of PEO orientation in the nanocomposite SPEs is obtained at 10wt% GO content and the Herman's orientation factor at this composition is calculated to be 0.64.

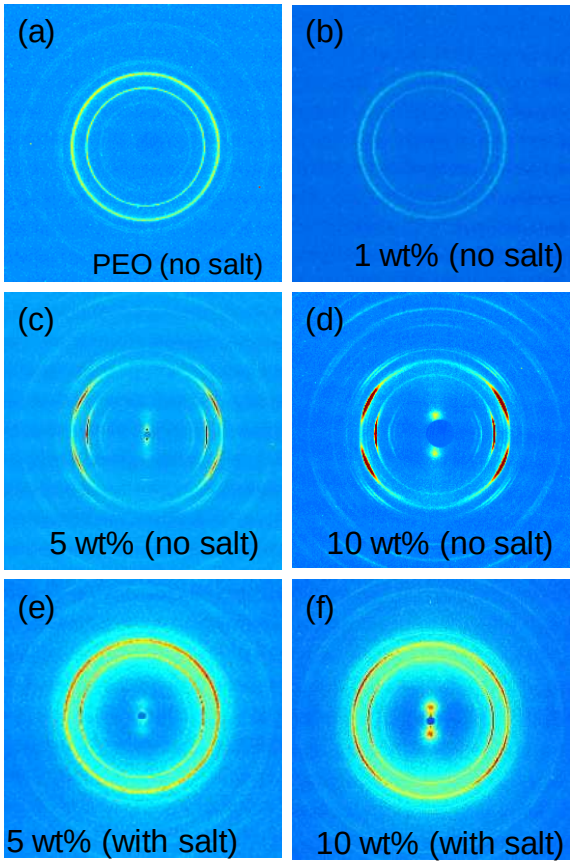

Figure 5.2 2D WAXD patterns of (a-d) GO/PEO nanocomposites without lithium salt at 0, 1, 5, 10 wt% of GO content, respectively. (e) and (f) nanocomposite doped with $LiClO_4$ (O/Li molar ratio of 12) at 5, 10 wt% GO content of total SPE weight, respectively. The WAXD patterns were collected from in-plane direction.

The PEO orientation factor f_{120} remains 0.64 when further increasing GO concentration, while the fraction of effective conducting phase comprised. Therefore, the optimal GO concentration was fixed at 10wt% of the total SPE weight. PEO molecular weight 300 kDa and O/Li molar ratio of 12:1 was used based on the criteria described in Chapter 4. The nanocomposite was fabricated by a two-step method as described in Chapter 3. The mixture was solvent casted and slowly dried in 45 °C oven for 5-7 days to allow complete solvent removal, resulting a uniform nanocomposite thin film with an average thickness of 100 to 200 μm. The nanocomposite SPE is denoted as 10wt% GO-$P(EO)_{12}$:$LiClO_4$ SPEs.

5.3 Structure and ionic conductivity correlation of nanocomposite SPEs

Temperature dependence of $\sigma_{//}$ and $\sigma_{\perp}$ for 10wt% GO-$P(EO)_{12}$:$LiClO_4$ was first investigated. The first heating curves at 1 °C/min for as cast 10wt% GO-$P(EO)_{12}$:$LiClO_4$ SPEs that stored at room temperature for 10 days are shown in Figure 5.3; the first heating scans of as cast $P(EO)_{12}$:$LiClO_4$ are also plotted for comparison. Each curve was repeated three times and the standard deviations are shown in Figure 5.3b. Three major features have been observed for these temperature dependent ionic conductivities: (i) in the low temperature region, the in/through plane conductivity difference of nanocomposite SPEs becomes more prominent than of solution cast PEO SPE and an anisotropy factor ($\sigma_{//}/\sigma_{\perp}$) as high as 70 is observed at room temperature; (ii) $\sigma_{//}$ for GO-containing samples is nearly one order of magnitude higher than that of the solution cast PEO SPE while the $\sigma_{\perp}$ values for both SPEs are similar at room temperature; (iii) In the

high temperature region, $\sigma_{//}$ curves for samples with and without GO are almost superimposed while $\sigma_{\perp}$ for GO-containing sample is noticeable lower.

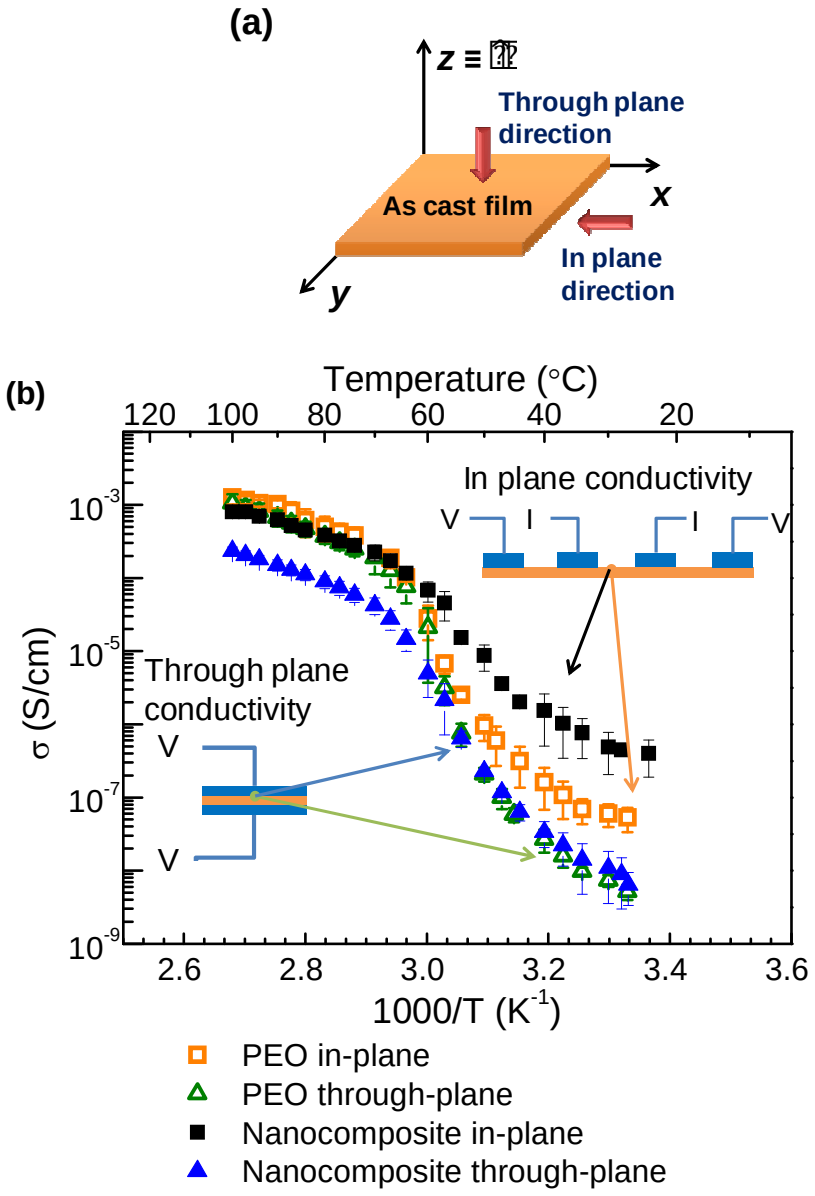

Figure 5.3 (a) Illustration of in-plane and through-plane directions of the as cast sample film; (b) Temperature dependent ionic conductivity for as cast SPEs that stored at room temperature for 10 days. All curves represent first heating scans from room temperature to 100 °C at 1 °C /min.

The conductivity anisotropy factor as a function of temperature and the in-plane and through-plane WAXD patterns of as cast 10wt% GO-P(EO)$_{12}$:LiClO$_4$ SPE are shown in Figure 5.4. At room temperature, the strong meridional scattering at low angle in the in-plane WAXD pattern suggests that the surface of the 2D GO nanoplatelets are oriented parallel to membrane surface and Herman's factor f_{001} was calculated to be -0.34 using equation 4.1 and 4.2 (in this case θ is defined as the angle between GO (001) plane normal and membrane surface). PEO crystal shows strong equatorial (120) diffraction with Herman's factor f_{120} of 0.64.

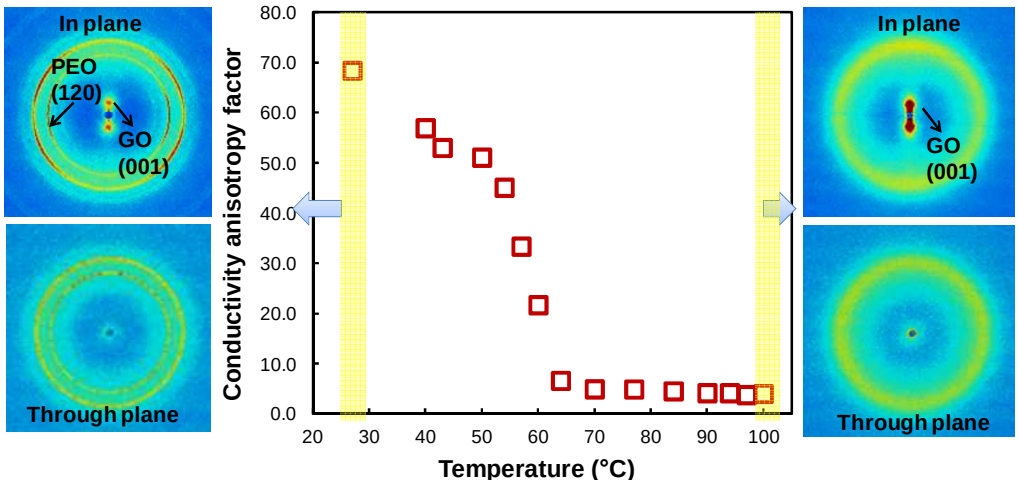

Figure 5.4 Conductivity anisotropy as a function of temperature for GO/PEO nanocomposite SPEs with the corresponding 2D WAXD patterns from both in-plane and through-plane directions at room temperature and 100 °C.

Both highly oriented GO nanoplatelets and PEO crystals are responsible for the enhanced conductivity anisotropy at room temperature. At high temperature, the PEO phase is in the molten state as suggested by the isotropic ring in the 2D WAXD pattern

from both in-plane and through-plane direction, the conductivity anisotropy of 4 observed at 100 °C can be attributed to GO orientation as the strong low angle meridional scattering from GO is retained at high temperature. The conducting mechanism is illustrated in Figure 5.5.

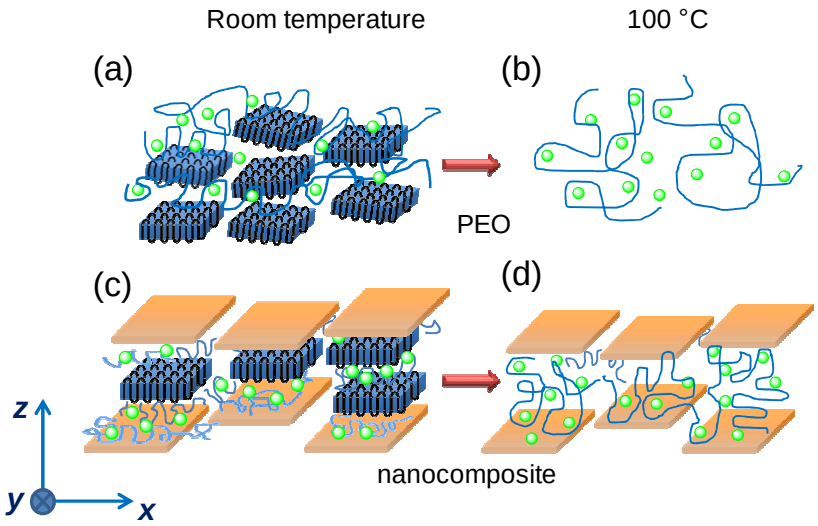

Figure 5.5 Illustration of the crystalline structure change of PEO (top) and GO/PEO nanocomoposite (bottom) SPEs from room temperature (left) to 100 °C (right).

To further understand the absolute conductivity difference between as cast PEO and nanocomposite SPEs at room temperature, the crystallization behavior was studied by DSC non-isothermal and isothermal scans. The non-isothermal scan from first heating of as cast SPEs stored at room temperature for 10 days are shown in Figure 5.6. Both SPEs exhibit very broad melting peaks and even shoulders, which indicates a broad distribution of PEO lamellae thickness as a result of the strong PEO-Li interactions

during the crystallization process. The nanocomposite SPE has a lower melting temperature (54 °C of the peak position compared with 62 °C for as cast PEO SPE) and reduced crystallinity (18.79% compared with 28.68% for as cast PEO SPE), suggesting a suppression of crystallization in the presence of GO nanoplatelets.

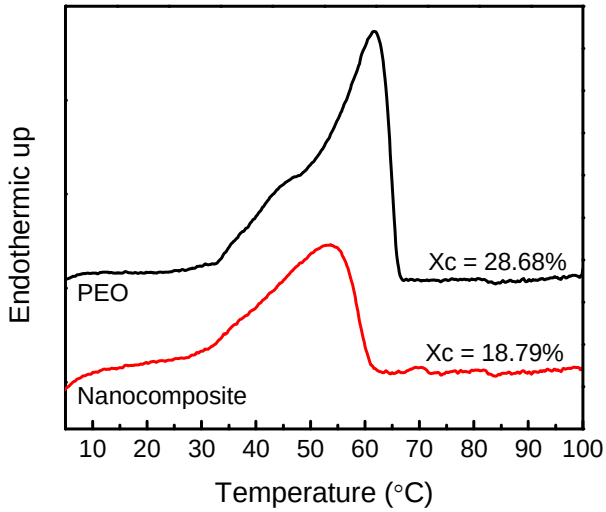

Figure 5.6 DSC first heating scans for as cast PEO and nanocomoposite electrolytes stored at room temperature for 10 days.

Isothermal crystallization measurements were further performed to investigate the crystallization kinetics. The nanocomposite and PEO films without salt doping were isothermally crystallized at 30 °C for 10 minutes and have been used as a control study. A lower isothermal crystallization temperature of 28 °C was selected for both SPE samples in this study since the crystallization kinetics of all SPE samples was significantly slower and a well-defined isothermal crystallization peak could not be obtained when the SPEs were crystallized at 30 °C. The isothermal crystallization curves are plotted in Figure 5.7.

Here $t_{0.05}$ and $t_{1/2}$ are defined as the time taken to reach 5% and 50% of the final crystallinity, respectively and the values are listed in table 5.1. Two different trends have been observed: (i) for the systems without lithium salt doping, $t_{1/2}$ decreases from 0.21 min for pure PEO film to 0.12 min for the nanocomposite, suggesting the crystallization kinetics is faster in the nanocomposite case. This is reasonable since the GO nanosheets act as heterogeneous nuclei that template the PEO crystallization; (ii) interestingly, opposite trend has been observed in the case of nanocomposite and as cast PEO SPEs. The nanocomposite SPE has a slower crystallization kinetics compared with PEO SPEs, and it is consistent with the reduced crystallinity shown in Figure 5.6.

The retardation of PEO crystallization in multi-phase systems is not unusual. Similar phenomenon had been observed in a PEO nanocomposite containing lithium dodecyl sulfate (LDS) stabilized single wall carbon nanotubes (SWNTs)[238-240]. It is proposed that the presence of Li^+ and SWNTs have a synergistic effect on the disruption of PEO crystallization. Specifically, Li^+ ions have an affinity to SWNTs and strongly interact with PEO, resulting in a local region of amorphous PEO-Li complex near SWNTs. The nucleation and growth of PEO are further disrupted by the SWNT network that imposes an energy barrier for chain diffusion during the crystallization process. This mechanism may be extended to our system and it seems to fit our conductivity results quite well. In our GO/PEO nanocomposite SPE, Li^+ ions in the vicinity of GO surface form amorphous complex with PEO and reduce the number of available nucleation sites for PEO heterogeneous crystallization. Ion transport is confined in the amorphous region and is guided by both GO nanoplatelets and PEO crystalline lamellae, resulting in a significant improvement on the room temperature $\sigma_{//}$ compared with that of PEO SPE.

Meanwhile the $\sigma_{\perp}$ for nanocomposite SPE is comparable with that of the PEO SPE despite the improved degree of PEO crystal orientation would have imposes more tortuous pathways along through-plane direction, which is likely due to the reduced crystallinity and possibly smaller crystallite size.

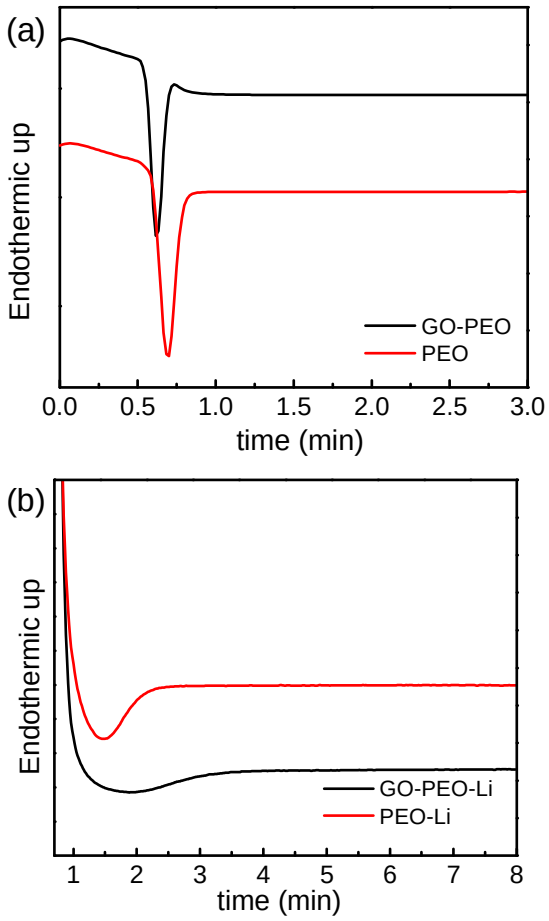

Figure 5.7 (a) Isothermal crystallization at 30 °C of GO/PEO nanocomposite and PEO films without lithium salt doping; (b) Isothermal crystallization at 28 °C of GO/PEO nanocomposite and PEO SPEs with $LiClO_4$ doping.

Avrami equation[241] is employed to describe the crystallization process and can be expressed as follows:

$$1 - X(t) = exp\left(-Kt^n\right) \quad (5.1)$$

Where *X(t)* is the relative crystallinity calculated as the ratio of the heat of fusion at time *t* and the total heat of fusion of the whole crystallization process and is plotted in Figure 5.8 as a function of *t*; *n* is the Avrami exponent and *K* is crystallization rate parameter. Values of *n* and *K* are determined using the initial linear part of the Avrami plot (Figure 5.9) and are listed in Table 5.1. The kinetics parameter *K* is significantly reduced for all SPEs compared with the pristine nanocomposite and PEO without salt doping as a result of the strong interaction between the salt and the polymer. *K* of the as cast PEO SPE is nearly as 3 times as that of the nanocomposite SPE, which is consistent with the $t_{1/2}$ result.

Table 5.1 Summary of crystallization parameters obtained from the isothermal crystallization scan.

	T_c (°C)	$t_{0.05}$ (min)	$t_{1/2}$ (min)	*n*	*K* (min^{-n})
GO-PEO	30	0.07	0.12	2.75	502.3
PEO	30	0.14	0.21	2.54	177.5
GO-PEO-Li	28	0.19	0.84	1.67	0.86
PEO-Li	28	0.12	0.49	1.74	2.45

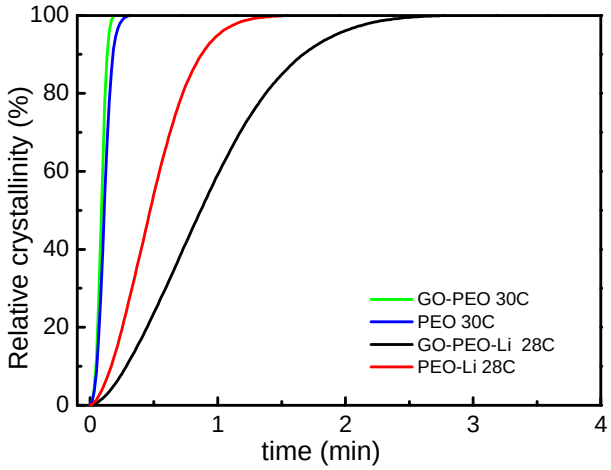

Figure 5.8 Relative crystallinity X(t) as a function of isothermal crystallization time t for both GO/PEO nanocomposite and PEO films with and without salt doping.

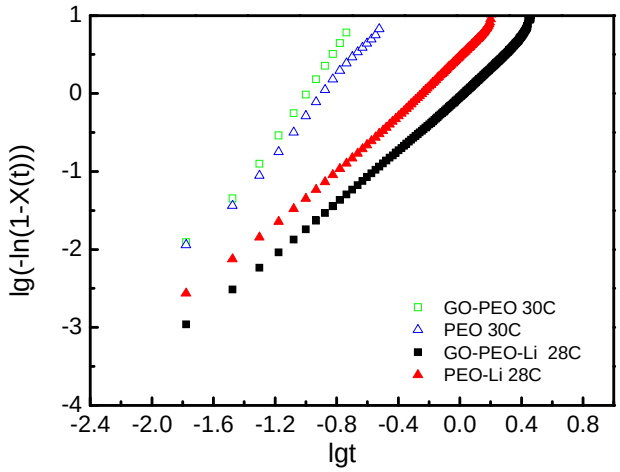

Figure 5.9 Avrami plots of both GO/PEO nanocomposite and PEO films with and without salt doping.

The Avrami exponent *n* typically indicates the growth dimension of the polymer. However, it should be noted that, in addition to growth dimensionality, the exponent also depends on many other factors. For example, 3D growth of athermal nucleation leads to

an exponent of 3 while similar 3D growth of thermal nucleation has an exponent of 4. Other factors complicate the situation include volume change during crystallization, changing growth rate during crystal growth, changing of nucleation mechanism due to asymmetric nucleation agent, etc.[242] Therefore, caution should be taken when applying Avrami analysis in polymer crystallization. The Avrami exponent *n* was calculated to be 2.75 and 2.54 for GO/PEO nanocomposite and PEO film without salt doping, suggesting a 3D spherulitic growth. On the other hand, the calculated Avrami exponent *n* values for both nanocomposite and PEO SPEs fell below 2 (1.67 for nanocomposite SPE and 1.74 for PEO SPE), which is possibly due to the strong interaction between PEO chain and Li^+ during the crystallization process. As the PEO starts to crystallize, the lithium ions are expelled from densely packed crystals and complex with polymer chains in the remaining amorphous region. The effective Li^+ to ether oxygen ratio gradually increases as the crystallinity increases, which would result in a stronger restriction of the mobility of the amorphous chains that need to diffuse to the growth front. This would possibly change the linear growth rate of the crystal, leading to the Avrami exponent deviation.

5.4 Summary

In this chapter, a nanocomposite approach had been employed to direct ion transport. A GO/PEO nanocomposite SPE was prepared by solution casting a homogeneous mixture of PEO, GO and $LiClO_4$. GO was highly aligned with the nanoplatelet surface parallel to the film surface during the slow solvent evaporation process, which further confined PEO crystallization, resulting in the polymer chain perpendicular to the film surface (PEO crystalline lamellae surface parallel to the film

surface). The conductivity anisotropy factor was calculated to be ~ 70 at room temperature and can be attributed to both GO and PEO crystal orientation. The presence of GO and Li^+ ions had a synergistic effect to retard PEO crystallization, and it is speculated that the ion transport was confined in the amorphous region and guided by GO nanoplatelet and PEO lamellae orientation, resulting in an enhanced in-plane conductivity compared with the solution cast PEO SPE.

CHAPTER 6: **PEO SINGLE CRYSTAL SPE CONTAINING LITHIUM PERCHLORATE**

6.1 Introduction

The effect of PEO crystallization on ionic transport is two-fold. In addition to the well-known slowed down dynamics of the tethered amorphous chain, the tortuous ion diffusion pathways associated with 2D polymer lamellar crystals are also critical to the overall observed conductivity. Results from Chapter 4 and 5 suggest that PEO crystal orientation is a key factor to the overall ionic conductivity. Significant conductivity anisotropy was achieved in the PEO/GO nanocomposite SPE system due to the high degree of orientation of PEO crystals and it is practically useful from an application point of view. However, the nanocomposite SPE is not an ideal model for quantitative studies of crystallization effect on ion transport since the crystallite size, lamellae thickness, and the distribution of lithium salt cannot be precisely controlled and characterized by a simple solution casting method.

On the other hand, polymer single crystal appears advantageous for the fundamental study of ion transport in crystalline polymers. Polymer single crystal (will be denoted as PSC for the following discussions), which is commonly confused with the crystallographic single crystals, often refers to a monolayer lamellae with uniform thickness (~ 10 nm) and chain folding direction perpendicular to the large lamellae surface (Figure 6.1). It can be grown from dilute solution in which the polymer chains are effectively separated from each other. Initial studies on polymer single crystals by Keller *et al.* were aimed at understanding the fundamentals of the chain folding structure[243-245].

Until very recently it had been demonstrated that PSCs would potentially have versatile applications in combined with the emerging nanotechnology[201, 203-204, 246-249].

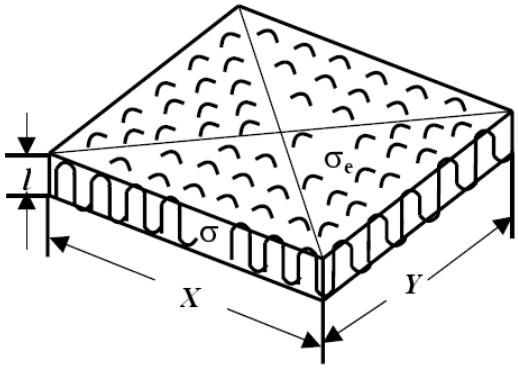

Figure 6.1 Illustration of the chain folding model in a polymer lamellae crystal, reported by Keller et al.[243]

Uniform sized PEO single crystals can be grown from dilute solution using a self-seeding method[198], in which technique the crystals are partially dissolved at elevated temperature (called seeding temperature T_s), leaving microscopic nuclei that template the subsequent crystal growth at lower crystallization temperature (T_c). The crystal size and lamellae thickness can be readily manipulated by varying the crystallization conditions (T_s and T_c, respectively). Square-shaped PEO single crystals are often observed as a result of chain folding along the {120} growth faces[250].

Ideally if an electrolyte membrane consists of stacks of PEO single crystals with precisely defined geometry and high degree of alignment, the tortuosity/structural effect can be quantified by comparing the in-plane and through-plane conductivities; and the

conductivity anisotropy $\sigma_{//}$ / $\sigma_{\perp}$ can be modeled using appropriate permeability model. In addition, since the effect of crystal orientation on ion transport is negligible along the in-plane direction, the dynamic/tethered chain effect can be directly measured by the ratio between in-plane conductivity of the PSC-SPE and the conductivity of its amorphous counterpart at the same ion concentration.

In this chapter, PSC-SPEs containing $LiClO_4$ as a model system were prepared using a two step method (Illustrated in Figure 6.2): (i) Depositing PEO single crystals that were grown from solution into a thin film; (ii) Introducing $LiClO_4$ by infiltration. Highly anisotropic ion conducting behavior with $\sigma_{//}$ to $\sigma_{\perp}$ ratio of up to 2000 has been observed, demonstrating the directed ion transport by individual lamella. The well aligned single crystal SPE also allows quantitatively study of the dynamic/tethered chain effect on conductivity. We demonstrate that the dynamic effect is significant at low ion contents, and becomes negligible as the ion content increases to an effective Li^+/EO ratio of ~ 0.1.

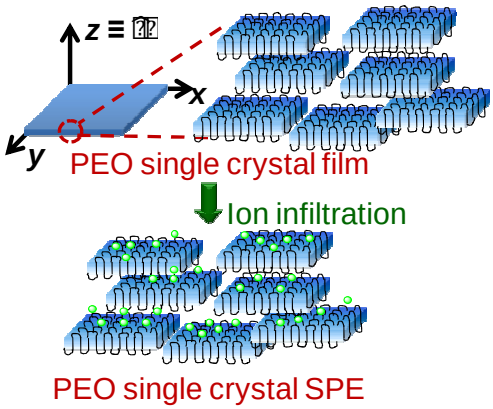

Figure 6.2 Schematic of PEO single crystal (PSC)-SPE preparation.

6.2 Preparation and structural characterization of PSC film

To prepare a PSC film, PEO single crystals were first grown in dilute pentyl acetate solution using a self-seeding method as described in section 3.2.4. Because of the well-controlled crystallization conditions, the obtained PEO single crystals have a uniform size as shown in the phase contrast microscope (Figure 6.3) and TEM (Figure 6.4a) images. The lateral size of the single crystals can be easily controlled by varying the seeding temperature (T_s): the higher T_s is, the less number of seeds left in the solution and therefore the larger lateral size of the resulting single crystals. The lateral sizes of PEO single crystals grown from 0.1 wt% pentyl acetate solution range from 2 μm to 50 μm when T_s increases from 51 ℃ to 54 ℃. Significant crystal overgrowth is observed when the lateral size is above 20 μm. The thickness of the crystals is ~ 10 nm as determined by AFM in Figure 6.4b when the polymer is crystallized at 20 ℃, and therefore the single crystals can be viewed as quasi-2D nanoplates. PSC with ~ 20 μm lateral size was selected for the following study since it reaches a high aspect ratio (~2000) while maintains the monolayer morphology for the majority of crystals.

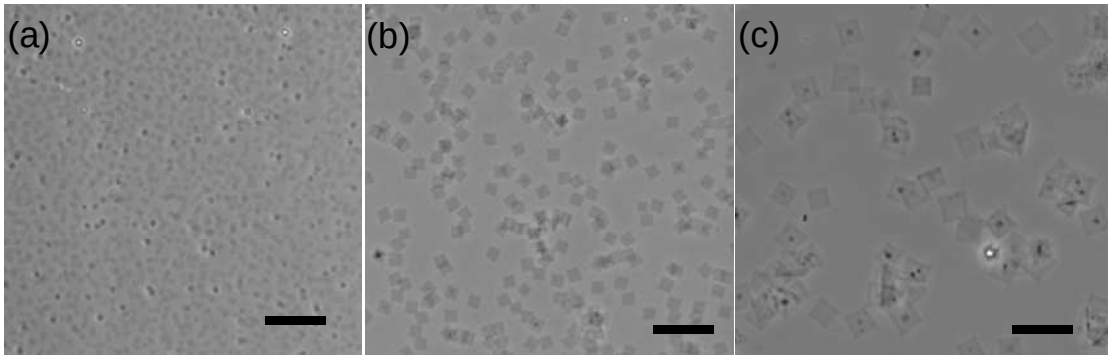

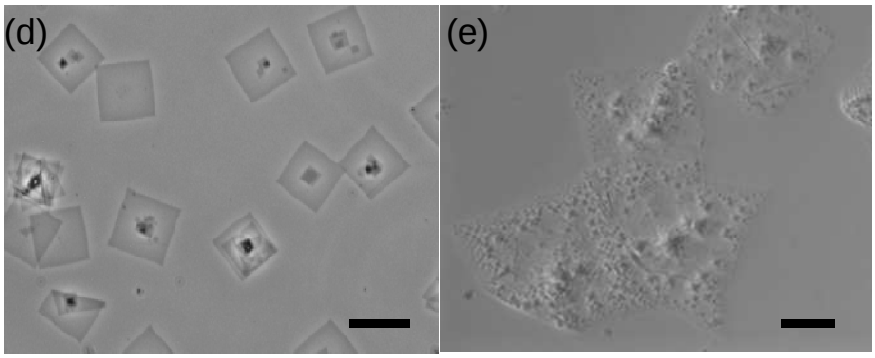

Figure 6.3 Phase contrast optical microscope images of PEO single crystals with different lateral sizes that are grown from dilute pentyl acetate solution at room temperature (PEO Mw ~ 300 kDa, 0.1 wt% pentyl acetate solution). The seeding temperatures in from (a) through (e) are 51 °C, 51.5 °C, 52 °C, 52.5 °C, 54 °C respectively. Scale bar is 20 μm.

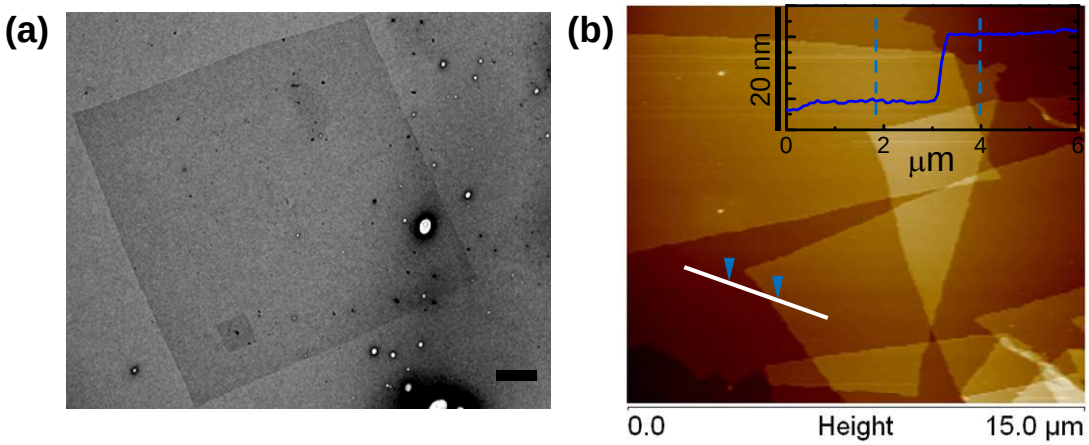

Figure 6.4 (a) Transmission electron micrograph of a typical PEO single crystal (T_s= 52.5 °C), scale bar is 2 μm; (b) Atomic force microscopy height image of a 15 x 15 μm area scan of single crystals. Inset shows the corresponding height profile along the white line.

The above single crystal suspension was slowly casted onto a PTFE substrate and dried under vacuum at room temperature to yield a single crystal film with an average thickness of 10 ~ 20 μm. The film is flexible and mechanically robust (Figure 6.5 inset). Thanks to the 2D nature of the crystal, they align parallel to the film surface upon

deposition. SEM image of the cross-section of the film reveals a well ordered layer structure (Figure 6.5). PEO crystal orientation was further confirmed using X-ray scattering.

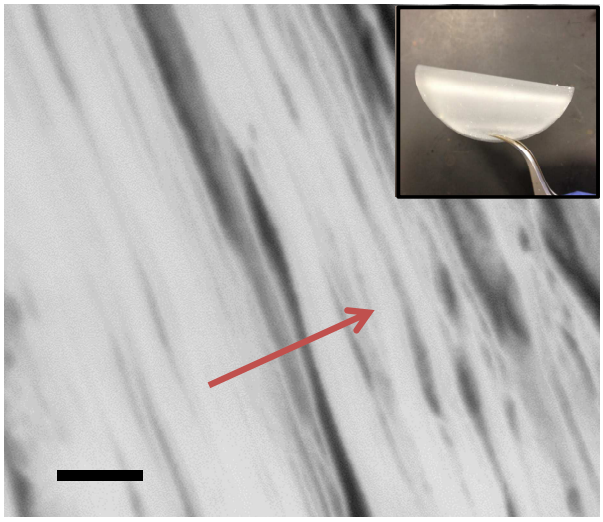

Figure 6.5 Scanning electron micrograph of the cross-section of a PEO single crystal film (lateral size of the single crystal is ~20 μm), red arrow shows the film normal, scale bar is 200 nm. Inset shows a photograph of the dry film.

2D WAXD experiments were conducted with the X-ray beam parallel to the film surface, and the in-plane diffraction pattern (Figure 6.6a left image) reveals well oriented patterns with (120) equatorial diffractions at 2θ = 19.15° and (032) diffraction at 2θ = 23.3° in the quadrants[223, 231, 251], indicating that the polymer chains are aligned parallel to the film normal. The Herman's orientation factor of (120) diffraction, f_{120}, is calculated to be 0.80 according to equation 4.1 and 4.2 described in section 4.4, Chapter 4 and the azimuthal integration of PEO (120) plane is shown in Figure 6.6c. Well-oriented SAXS

pattern was also obtained as shown in Figure 6.6a (right image). Strong meridional scattering arcs arise from the periodic electron density fluctuation from crystalline stem and amorphous folds of the polymer single crystals, and the orientation of the lamellae is consistent with WAXD results.

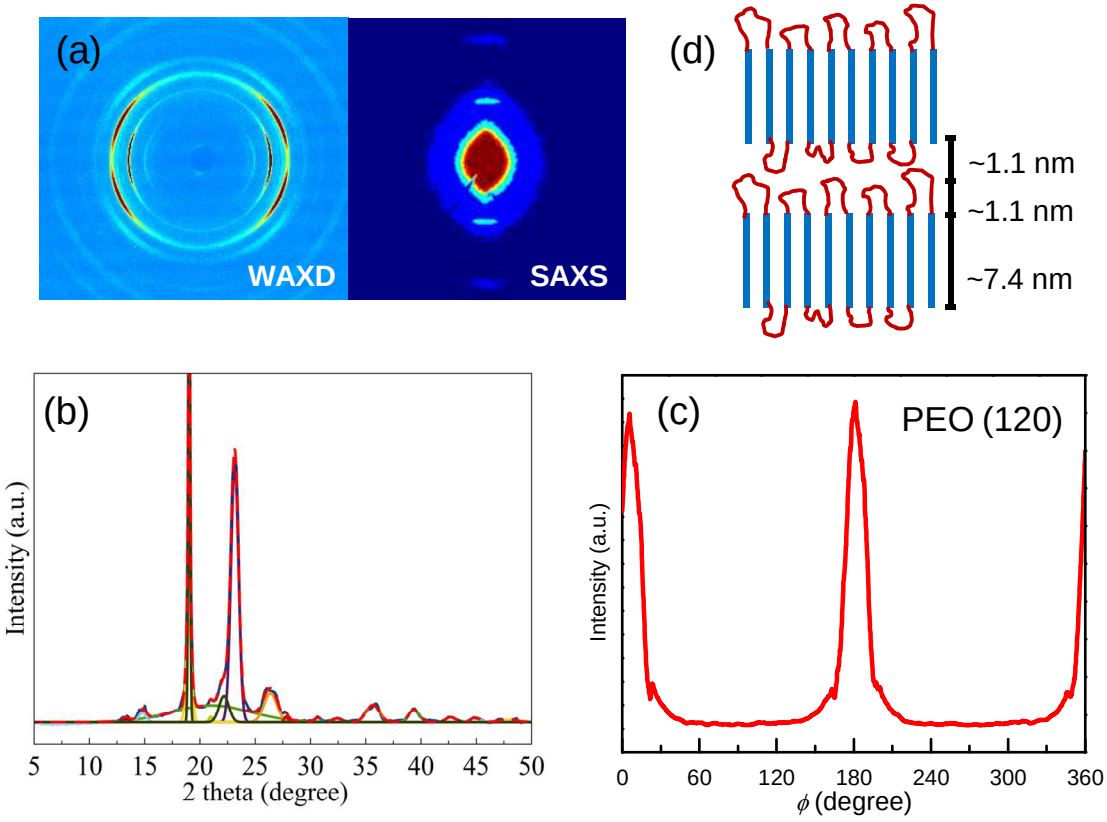

Figure 6.6 (a) 2D in-plane WAXD (left) and SAXS (right) patterns of as cast PSC film; (b) Azimuthal integration and peak fitting of isotropic WAXD data for PSC film. (PSC film had been folded and randomized in order to obtain an isotropic disk for WAXD measurement); (c) Azimuthal profile of PEO (120) diffraction for PSC film, X-ray beam is parallel to film surface. (d) Schematic illustration of PEO crystalline stems (blue) and amorphous loops (red).

The period of the lamellar stacks calculated from SAXS integration is 9.6 nm, which is comprised of two layers of amorphous loops attached to the crystalline stems.

The crystallinity X_c is estimated to be 0.77 based on integration of isotropic WAXD patterns as shown in Figure 6.6b using the following equation:

$$X_c = \frac{\sum_i I_i^c}{\sum_i I_i^c + \sum_j I_j^a} \tag{6.1}$$

Where I_i^c is the area under the crystalline peak and I_j^a is the area under amorphous peak. The fitting result is shown in Figure 6.6b. Combining SAXS and WAXD results, the thickness of each amorphous loop layer is calculated to be approximately 1.1 nm, and the crystalline stems have a thickness of 7.4 nm (red and blue regions in Figure 6.6d). Comparing to crystalline stem layers, polymer loop-containing fold surfaces (red region) are loosely packed, which is prone to Li^+ binding.

6.3 Preparation and structural characterization of PSC-SPEs containing $LiClO_4$

To prepare PSC-SPE, $LiClO_4$ was infiltrated into the above mentioned PEO single crystal film by soaking the latter in 0.02~0.2 wt% $LiClO_4$ / pentyl acetate solution at time intervals varying from 1 to 10 min (schematics in Figure 6.2). Here Li^+ to ethylene oxide (EO) molar ratio is defined as *r*, which is calculated from the weight differences of the film before and after salt infiltration. All the PSC-SPE films were vacuum dried for at least 5 days at room temperature prior to any measurement to completely remove the residue solvent (The moisture/solvent level in the SPE is low enough and has negligible impact on the conductivity measurement after 5 days since the conductivity remains unchanged over 2-3 months when stored in Argon purged glovebox). To simplify the system, the Li^+ concentration was controlled in the region of $0.001 < r < 0.05$ so that only crystalline PEO and amorphous PEO:Li complex are present[111]. 2D in-plane WAXD

results in Figure 6.7 top row show that both PEO crystalline structure and crystal orientation remain the same after the infiltration process, and PSC-SPEs exhibit only a monoclinic crystal structure of pure PEO within the entire Li^+ concentration range studied in this chapter as indicated by the Azimuthal integration of WAXD patterns in Figure 6.8a.

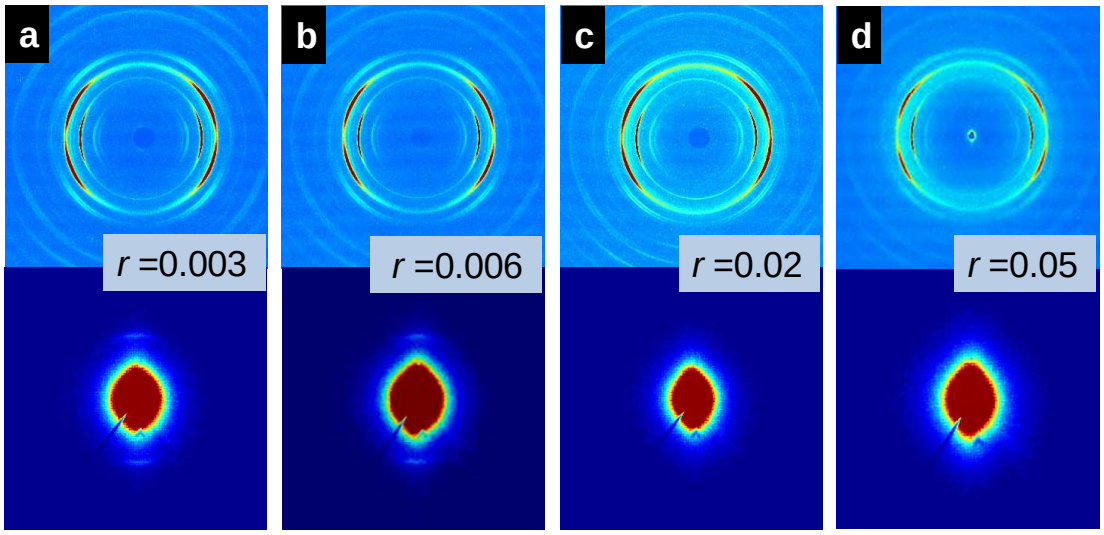

Figure 6.7 (a-d) 2D in-plane WAXD (top row) and SAXS (bottom row) patterns of selected PSC-SPEs containing $LiClO_4$ with Li^+ to EO ratio r =0.003, 0.006, 0.02 and 0.05, respectively. The meridian of the diffraction patterns is parallel to the film normal.

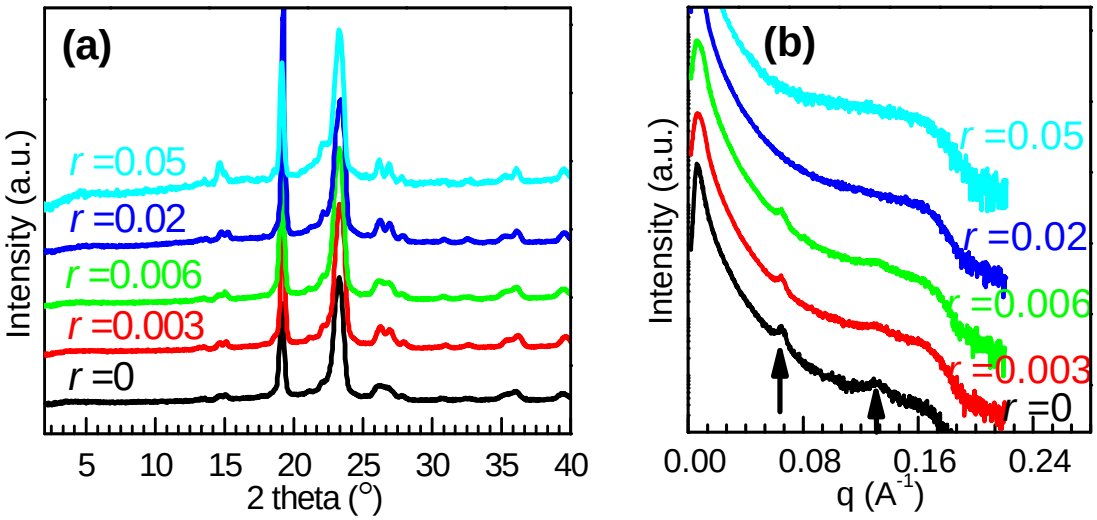

Figure 6.8 Azimuthal integrations of the (a) 2D WAXD patterns and (b) 2D SAXS patterns of PSC-SPEs containing $LiClO_4$ at different Li^+ concentrations.

The crystallinity of the films does gradually decrease from 77% to 60% when *r* increases from 0.001 to 0.05, which is likely due to the strong Li-PEO interaction (Figure 6.9). Another interesting observation is that the long period completely disappears in $r \geq 0.02$ samples in the SAXS patterns, suggesting that Li^+ infiltrates into PEO single crystal fold regions instead of laterally solvating the crystalline stem (Figure 6.10). As more and more salts accumulate in the fold region, the electron density contrast decreases and eventually disappears. Therefore, one can adopt a 2-phase model (PEO crystalline phase and amorphous PEO/Li^+ salt phase) to analyze the ion transport behavior as shown in Figure 6.10. All the ions are confined in a 2D space with a thickness of ~ 2–3 nm. For conductivity discussion, it is therefore more appropriate to use an effective Li^+ to EO molar ratio by normalizing *r* with the corresponding crystallinity of each SPE, and the normalized *r* is denoted as $\langle r \rangle$ ($\langle r \rangle = r/(1-Xc)$), as shown in Table 6.1.

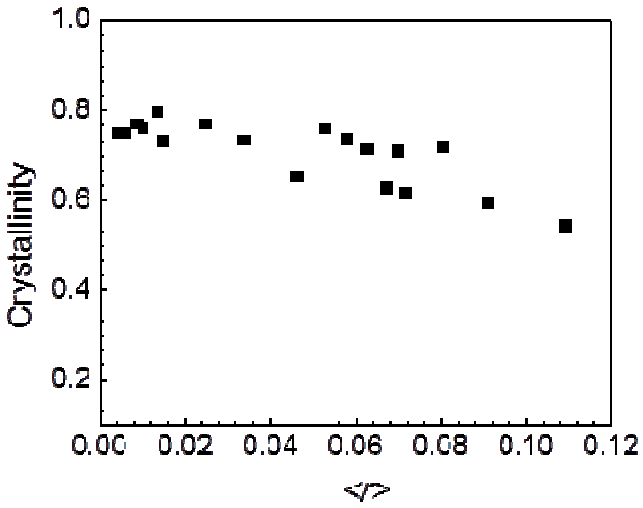

Figure 6.9 Crystallinity of PSC-SPEs as a function of Li to EO ratio *r*, determined by WAXD integrations.

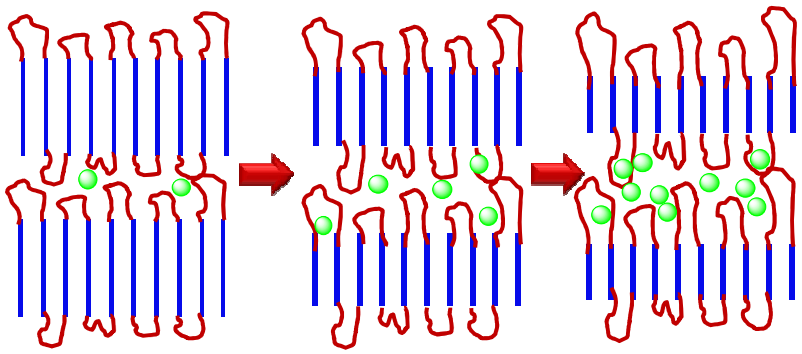

Figure 6.10 Schematic illustration of PEO crystalline stems (blue) and amorphous loops (red). Ions (green) are confined in the fold regions.

6.4 Ion transport in PEO single crystal SPE model system

6.4.1 Tortuosity effect

Room temperature ionic conductivities of all SPEs were measured from both in-plane ($\sigma_{//}$) and through-plane ($\sigma_{\perp}$) directions. Figure 6.11 shows that both $\sigma_{//}$ and $\sigma_{\perp}$

increase rapidly with <*r*> at low Li^+ ion concentration (<*r*> < 0.02), and nearly plateau when <*r*> is above 0.02. In the entire region studied, $\sigma_{//}$ is significantly greater than $\sigma_{\perp}$. The conductivity difference along these two directions can be quantified by anisotropy factor $\sigma_{//}/\sigma_{\perp}$. Figure 6.11 shows two distinct regions of $\sigma_{//}/\sigma_{\perp}$, *i.e.* for <*r*> < 0.02, $\sigma_{//}/\sigma_{\perp}$ is approximately 800-2,000, and it decreases to 100–300 where <*r*> > 0.02. Overall the in-plane conductivity of the polymer single crystal SPEs is 2-3 orders of magnitude greater than that of the through-plane one.

Previous studies have reported numerous SPEs with anisotropic conductivities[26, 128, 166, 252-253]. For example, anisotropic conducting behavior can be achieved in BCP systems after aligning the films using a solvent casting method[253] or applying mechanical, electric, or magnetic fields[26, 128, 166, 254]. Well-designed liquid crystal (LC)[129, 165] or holographically polymerized systems[132] also showed large anisotropy. Among all the achieved values, $\sigma_{//}/\sigma_{\perp}$ of 2,000 is one of the highest and it is also achieved in a semicrystalline SPE with a crystallinity of ~ 70%. Evidentially, this unprecedented conductivity anisotropy in semicrystalline SPEs is due to the well-controlled single crystal SPE morphology. From the molecular structure standpoint, the 2-phase morphology in semicrystalline polymers is analogous to lamellar BCP, or smectic LC phases – even the length scales are close. This simple comparison leads to an interesting finding: if the lamellar morphology can be well controlled, the two-phase semicrystalline SPEs system, similar to BCP, could be a valid model to design mechanically strong and ionic conducting SPE. In this case, ion transport is confined within the chain fold region, and guided by the crystalline lamellae.

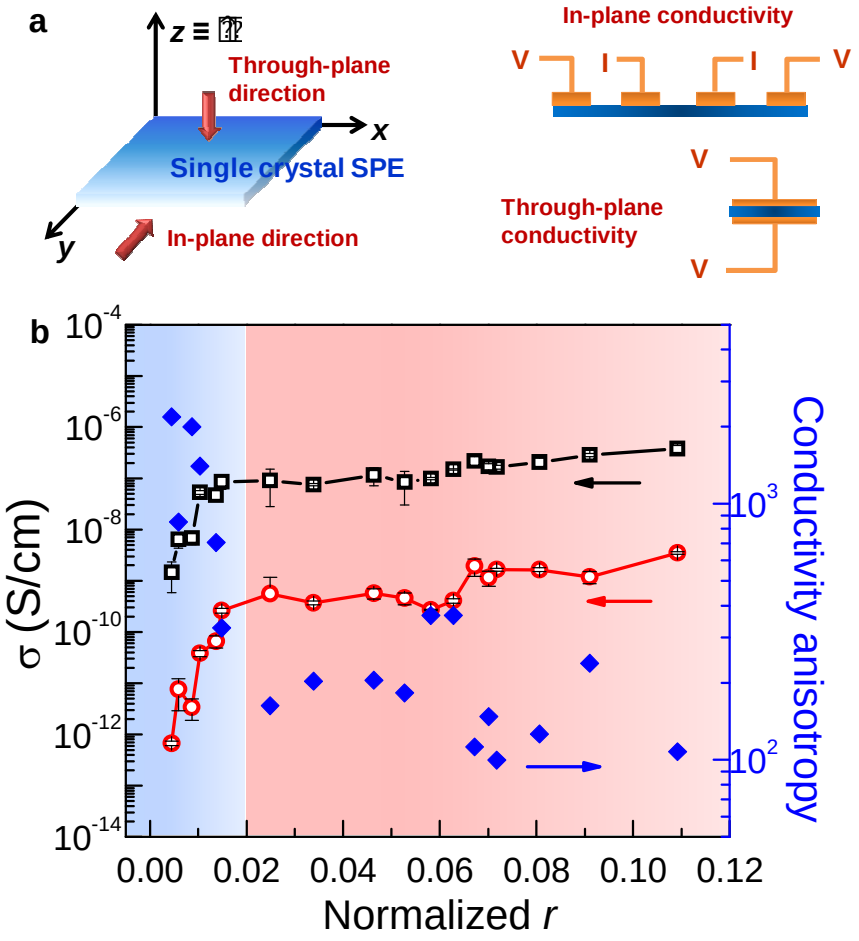

Figure 6.11 (a) Schematic description of in-plane and through-plane conductivity measurement setup. (b) Ionic conductivity and conductivity anisotropy as a function of normalized r. (black open square: $\sigma_{//}$ of single crystal SPEs; red open circle: $\sigma_{\perp}$ of single crystal SPEs; blue solid diamond: conductivity anisotropy $\sigma_{//}/\sigma_{\perp}$ of single crystal SPEs)

6.4.2 Dynamic effect

The effect of crystallization on ion conductivity is two-fold. The previously discussed conductivity anisotropy shows the structural/tortuosity effect, while there is a dynamic effect where the relaxation of the amorphous chain is affected because they are locally tethered to the crystalline lamellae. In a typical semicrystalline SPE, these two

factors are often intertwined and it is difficult to quantitatively evaluate the significance of each factor. However, one can decouple them using the previously mentioned well-aligned polymer single crystal SPEs. This is because that structural/tortuosity effect is negligible along the lamellar direction. Here we introduce a coefficient *k* to describe the dynamic effect and it is defined as the ratio between measured normalized $\sigma_{//}$ (denoted as $|\sigma_{//}|$, $|\sigma_{//}| = \sigma_{//}/(1-\phi_s)$) of PSC-SPEs and the conductivity of the corresponding 100% amorphous SPE counterpart (denoted as σ_0).

At $r = 0.1$, σ_0 can be directly measured immediately after quenching the SPE from 120°C to room temperature because the SPE remains 100% amorphous due to the slow crystallization kinetics at this ion concentration. However, measuring σ_0 of 100% amorphous SPEs at lower *r* is difficult because of the fast crystallization kinetics of linear PEO. Nevertheless, one can use a Vogel-Tamman-Fulcher (VTF) equation to fit the high temperature (above melting) data and extrapolate the plot to room temperature[104-106],

$$\sigma = \sigma_0 e^{-B/(T-T_0)} \tag{6.2}$$

The cooling scans of temperature dependent conductivity for linear PEO (M_w ~300 kDa) SPEs at *r*= 0.01 and 0.033 are shown in Figure 6.12 and the fitted parameters are listed in Table 6.1.

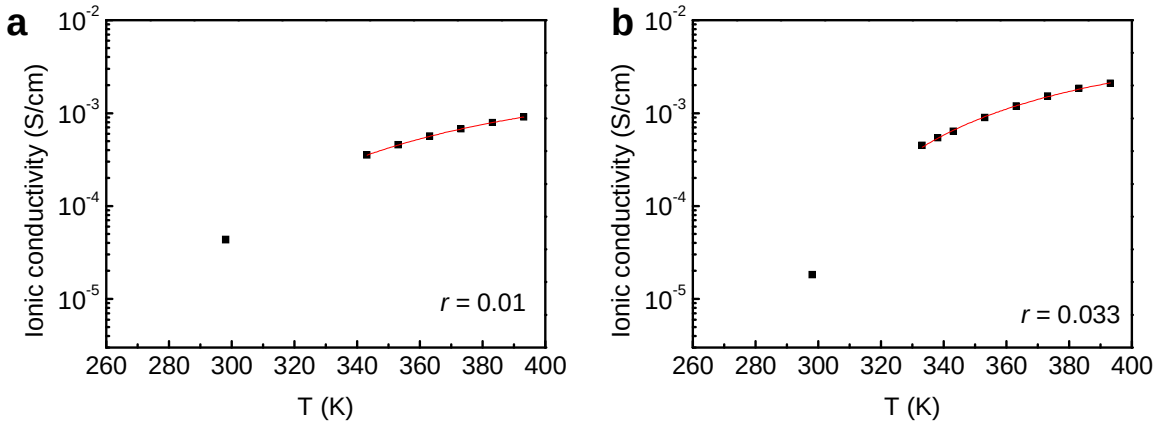

Figure 6.12 VTF fitting of the cooling scan of temperature dependent conductivity above T_m at (a) r = 0.01 and (b) r = 0.033. All the samples were equilibrated for ~ 1h at each temperature before measurement.

Table 6.1 Fitting parameters using VTF equation for temperature dependent ionic conductivity curves of different SPEs.

	σ_0	B	T_0
***r* = 0.01**	7.26×10^{-3}	332.4	233.3
***r* = 0.033**	1.56×10^{-2}	268.8	258.4

The extrapolated room temperature conductivities at r= 0.01 and 0.033 and the measured conductivity of melt quenched linear PEO SPE that is 100% amorphous are plotted as the green triangles in Figure 6.13. As a comparison, σ_0 of cross-linked PEO network (100% amorphous) SPEs reported by Watanabe *et al.* [255] are also plotted (inverted triangle) in Figure 6.13. And the two curves representing the 100% amorphous counterparts are compared with the $\sigma_{//}$ of our PSC-SPEs containing $LiClO_4$. Despite slight discrepancy of the σ_0 values which is likely due to cross-linking effect, the conductivities for both linear amorphous and network SPEs gradually decrease with

increasing Li^+ concentration. It is a net result from both increased T_g of the polymer due to Li-ether oxygen interaction and ion aggregation, detailed discussion can be found elsewhere[255]. The dynamic effect can therefore be quantified by comparing σ_0 with $\sigma_{//}$ at a given <*r*>. Table 6.2 summarizes the calculated coefficient *k* using σ_0 obtained from the above mentioned two sets of data. *k* gradually decreases from 180/30 at <*r*> = 0.01 to 2.1/0.6 at <*r*> = 0.11, suggesting that the conductivity reduction due to the dynamic effect decreases from 10^1 ~ 10^2 to near unity.

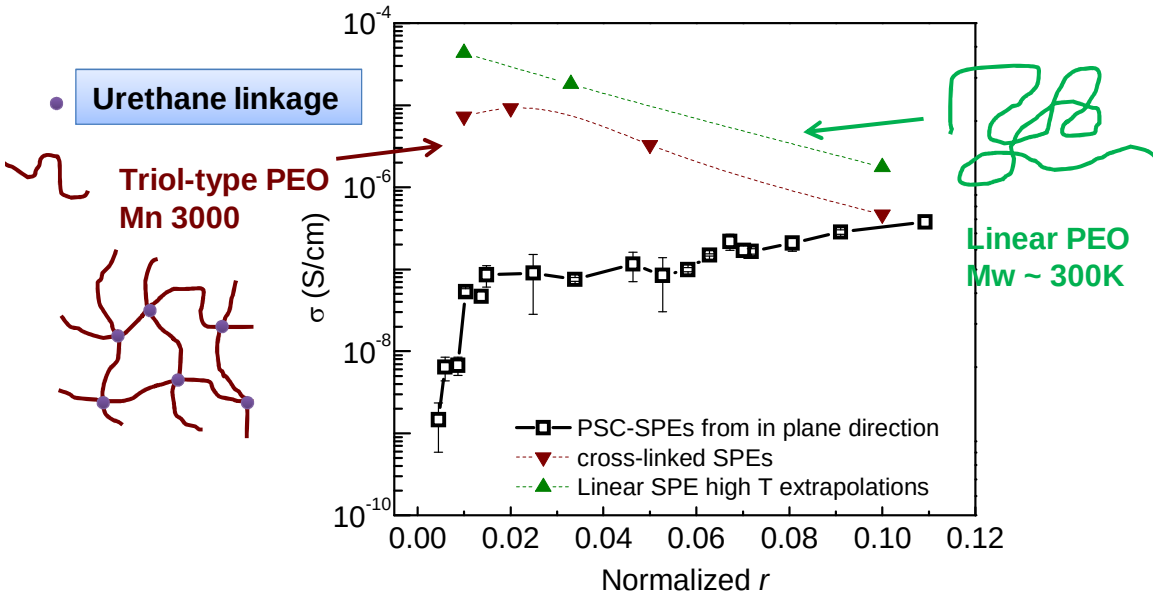

Figure 6.13 Comparison of in-plane conductivity of PSC-SPEs containing $LiClO_4$ and the conductivity of 100% amorphous SPEs. Green triangle: σ_0 of linear PEO-$LiClO_4$ SPEs; brown inverted triangle: σ_0 of network PEO-$LiClO_4$ SPEs from ref[255].

Table 6.2 Summary of σ_0 and calculated coefficient k at different r.

r	X_c	<r>	$\lvert\sigma_{//}\rvert$ (S/cm)	$\sigma_{0//}^{a,b}$ (S/cm)	Calculated k from $\sigma_{0//}^{a,b}$	σ_0^{c} (S/cm)	Calculated k from σ_0^{c}
0.050	0.54	0.11	3.77×10^{-7}		2.1		0.6
0.037	0.59	0.09	2.85×10^{-7}	1.76×10^{-6} ,a	2.5	4.65×10^{-7}	0.7
0.023	0.72	0.08	2.08×10^{-7}		2.4		0.6
0.013	0.76	0.05	8.42×10^{-8}	-	-	3.30×10^{-6}	9.4
0.006	0.77	0.03	1.02×10^{-7}	1.81×10^{-5} ,b	41.90	9.22×10^{-6}	20.9
0.003	0.76	0.01	5.68×10^{-8}	4.32×10^{-5} ,b	180.8	7.29×10^{-6}	30.5

a: Measured room temperature conductivity of amorphous SPE at r = 0.1;

b: σ_0 extrapolated from high temperature conductivity of linear SPEs using VTF equation;

c: room temperature conductivity of network PEO SPEs, data reproduced from *ref* [255].

Glass transition temperatures for single crystal SPEs were measured to better understand the dynamic effect on conductivity at different ion contents, and the results are shown in Figure 6.14. The T_g at a given <r> of the single crystal SPEs prepared is nearly identical to that of either PEO networks[255] or solution cast SPEs[62] reported elsewhere. For example, the T_g is –46.3°C at <r> = 0.014 for single crystal SPE and is –43°C at <r> = 0.01 for PEO network. When <r> = 0.1, T_g is approximately –22°C to –15°C for all types of SPEs. Therefore, polymer chain mobility, which characterized by T_g alone, cannot explain different k values at various <r>. And we propose that the local chain conformation restricted by the attached crystalline lamellae would play an important role in determining the k. At low <r> where long range polymer segmental motion is forbidden, this tethered chain effect is significant and results in one to two orders of magnitude drop of conductivity compared with amorphous SPEs. On the other hand, at moderate <r>, ions themselves would act as cross-linkers to reduce the long

range segmental motion of the polymer; therefore, the tethered chain effect is no longer the limiting factor.

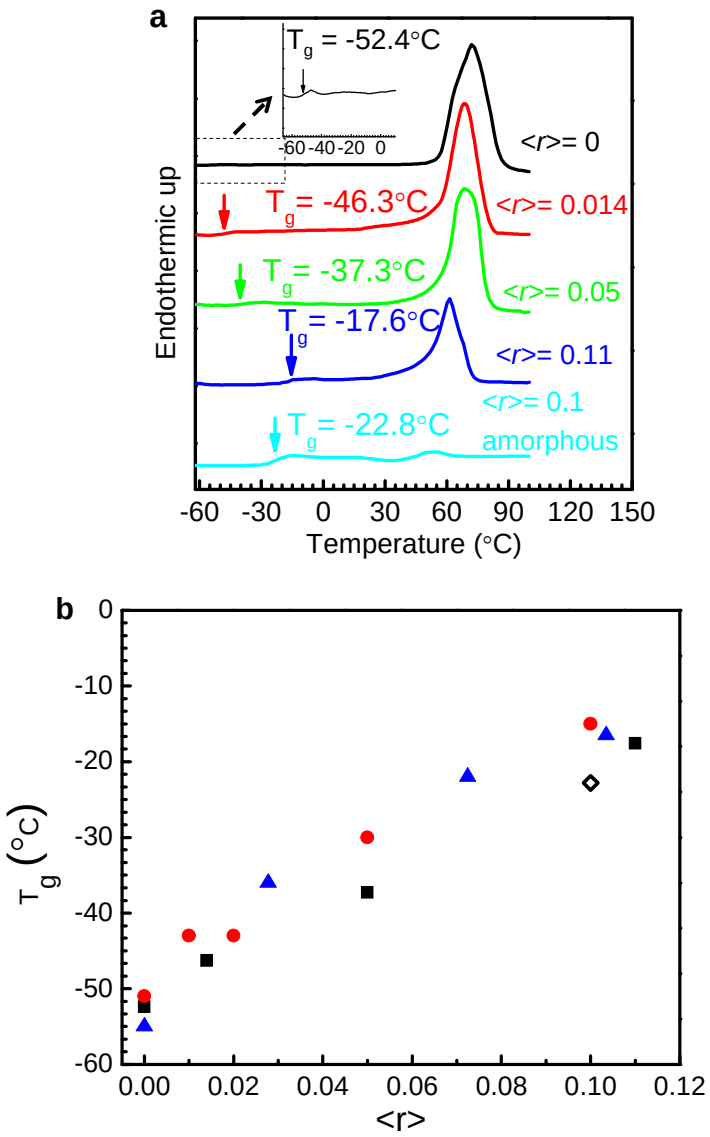

Figure 6.14 (a) T_g of PEO single crystal SPEs determined by differential scanning calorimetry (DSC). The samples were first cooled from 0°C to -100°C at 1°C/min and then heated from -100°C to 100°C at 40°C/min. T_g was determined by the heating curve; (b) T_g as a function of <*r*> for different SPEs. Black solid squares denote the single crystal SPEs in our current work, red solid circles are the network PEO SPEs reproduced from ref[255]. Blue solid triangles are solution cast linear PEO SPEs reproduced from ref[62]. Black open diamonds represent the amorphous linear PEO SPE at <*r*> = 0.1 prepared in the current work.

Temperature dependent conductivities were also measured for PEO single crystal SPEs at both dilute and higher Li^+ concentration regions. First heating scans of both $\sigma_{//}$ and $\sigma_{\perp}$ at a constant rate of 1°C/min for SPE at <*r*> = 0.015 and 0.08 are shown in Figure 6.15a and b. For SPE at <*r*> = 0.015, with increasing temperature, the conductivity anisotropy remains unchanged (or slightly decreases) below T_m, and sharply drops to ~2 at T_m. On the other hand, the anisotropy decreases continuously below T_m and the slope becomes steeper near T_m for SPE at <*r*> = 0.08, which is due to an earlier onset of melting, supported by both *in-situ* WAXD (Figure 6.16) and DSC (Figure 6.17). At temperatures below the onset, $\sigma_{//}$ and $\sigma_{\perp}$ for both SPEs exhibit Arrhenius behavior, which confirms that ion hopping is the conduction mechanism.

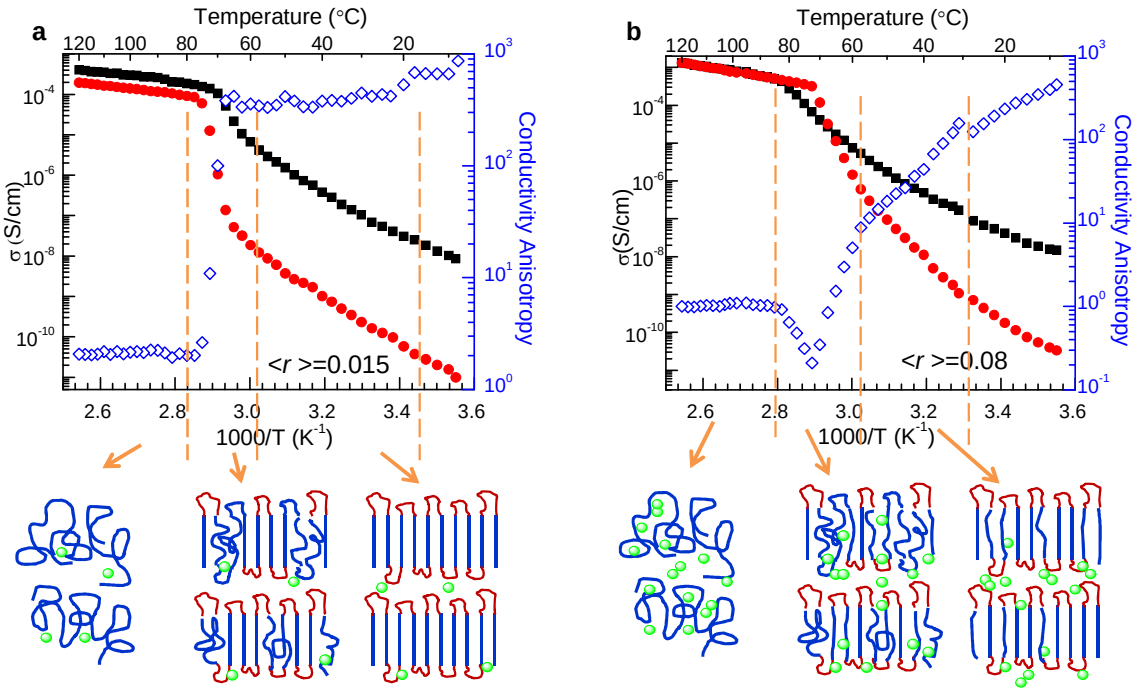

Figure 6.15 Temperature dependent ionic conductivity of PEO single crystal SPEs at (a) dilute region where <r> = 0.015; (b) high concentration region where <r>=0.08, data were collected

during first heating scan at 1°C/min heating rate. Scheme shows the proposed morphology at different temperature ranges for the two SPEs.

E_a of $\sigma_{//}$ and $\sigma_{\perp}$ can be calculated to be 0.86 eV and 1.06 eV at <*r*> = 0.015, and 0.75 eV and 1.17 eV at <*r*> = 0.08. For both SPEs, the in-plane activation energy is consistently lower than its corresponding through-plane activation energy, suggesting that it is more difficult for ions to circumvent the highly oriented crystals than hopping along the crystal surface. Robitaille *et al.* reported E_a of PEO-$LiClO_4$ electrolyte at 60°C < T < 120 °C is approximately constant and equals to ~0.7 eV at high Li^+ loading and ~ 0.3 eV for diluted electrolytes[111]. As a comparison, the in-plane E_a of the concentrated single crystal SPE at <*r*> = 0.08 (E_a=0.75) is close to that of reported for concentrated electrolyte (0.7 eV). This further supports our previous statement that crystallization has nearly no effect on ion conduction for the in-plane direction in moderate ion concentration systems.

Table 6.3 Summary of activation energy E_a of various SPEs

E_a (eV)	PSC SPE In plane	PSC SPE Through plane	Amorphous SPE
<*r*> = 0.015	0.86	1.06	0.3
<*r*> = 0.08	0.75	1.17	0.7

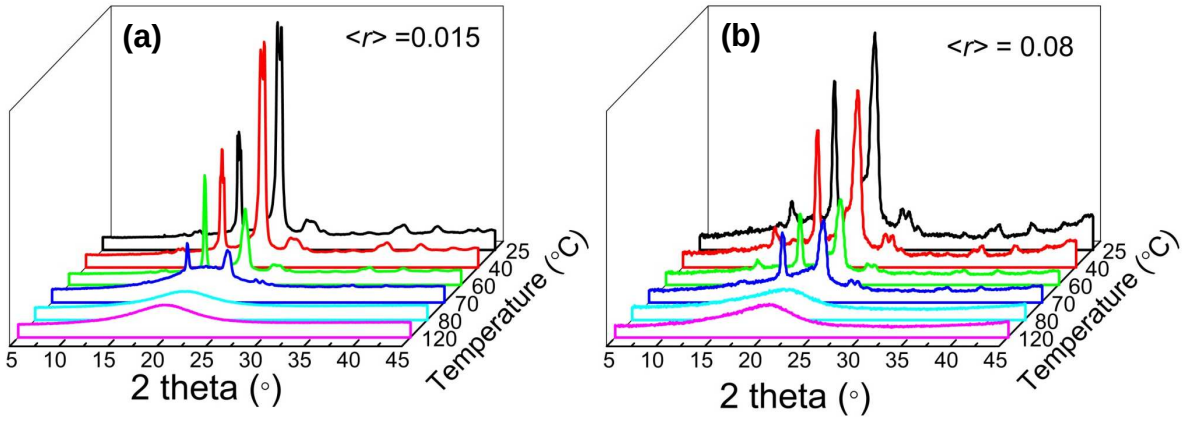

Figure 6.16 In-situ WAXD measurements for single crystal SPEs at (a) <r> = 0.015 and (b) <r> = 0.08 from first heating curve, the average heating rate was controlled to ~ 1°C/min;

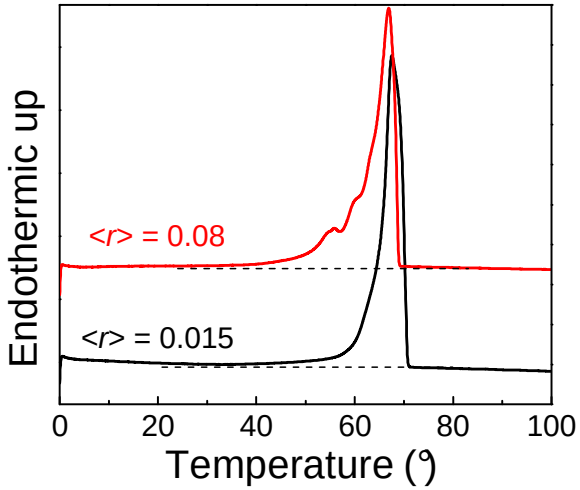

Figure 6.17 DSC first heating scans from 0°C to 100°C at 1°C /min heating rate for single crystal SPEs at <r> = 0.08 and 0.015.

It is also interesting to note that at <*r*> = 0.08, $\sigma_{//}$ and $\sigma_{\perp}$ show a crossover near the end of the melting process. This is probably due to the polymer chain memory effect upon melting: although crystals are molten, polymer chains are still loosely orientated

parallel to the film normal, which facilitates ion transport along the through-plane direction. The crossover near melting is not observed at $<r>$ = 0.015 since the ion concentration at this composition is too low so that ions remain phase separated from the molten lamellae within the timescale of the measurement, as illustrated in the scheme in Figure 6.15.

6.5 Summary

It was demonstrated for the first time that the two intertwined effects of PEO crystallization on ionic conductivity reduction, namely the structural/tortuosity effect and dynamic/tethered chain effect, can be decoupled and quantified using a model PEO single crystal SPE with controlled size, structure, crystallinity, and crystal orientation. High conductivity anisotropy (10^2~10^3) was obtained when the degree of 2D PEO lamellae orientation is high (f_{120} = 0.8). The important result from this study is that the conductivity reduction via chain tethering due to crystallization is not always as significant as it had been widely considered. For dilute electrolytes, a drop in conductivity by a factor of ~10^1 to 10^2 was observed, which can be explained by long range polymer segmental motion prohibition due to the rigid amorphous loop tethered on crystal lamellae surface. However, with a moderate ion concentration, crystallization has nearly no effect on chain mobility and the conductivity decrease is controlled by crystal orientation, strong Li-PEO interaction and Li^+ aggregation.

CHAPTER 7: **PEO SINGLE CRYSTAL SPE CONTAINING LITFSI**

7.1 Introduction

PSC SPEs containing $LiClO_4$ as discussed in the previous chapter has served as a perfect model system to understand the crystallization effect on ion transport in semicrystalline PEO based SPEs. Throughout the entire Li^+ concentration studies, the PSC-SPEs can be treated as a two-phase model that consists of PEO crystalline lamellae phase and amorphous PEO:Li complex phase in the loop region between PEO lamellae. This model allows for a quantitative study of both tortuosity and dynamic effect on ion transport. However, the drawback for using $LiClO_4$ is that it tends to aggregate into ion pairs, triplet and ion clusters at higher ion concentrations and the T_g raises significantly due to strong PEO-Li interaction, which is a limiting factor for polymer chain mobility reduction and ionic conductivity decrease.

On the other hand, Lithium bis(trifluoromethylsulfonyl) imide (LiTFSI), which was first discovered by Armand *et al.*[256] and systematically studied by Prud'homme *et al.*[114, 182] later on, shows a few advantages over $LiClO_4$ (chemical structures of these two types of salts are shown in Figure 7.1). It has a wide electrochemical stability window and large charge delocalization as the bulky anion promotes higher degree of ion dissociation. In addition, the TFSI anion acts as a plasticizer in the amorphous phase of PEO:Li salt complex, which lowers the T_g of the electrolyte, increases polymer chain mobility and therefore improves the room temperature conductivity.

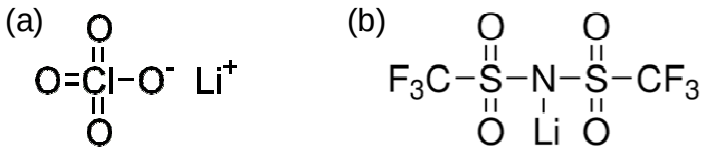

Figure 7.1 Chemical structures of (a) $LiClO_4$ and (b) LiTFSI.

The phase diagram of PEO:LiTFSI electrolyte that had been developed by Prud'homme *et al.*[114, 182] are shown in Figure 7.2. Only crystalline PEO and amorphous PEO-Li salt complex phase coexist in dilute region where O/Li molar ratio is above 12, which is similar to the PEO:$LiClO_4$ electrolyte system[111]. In the semi-dilute region (6 <O/Li<12), PEO crystallization kinetics is significantly slowed down[257-258], and even a crystallinity gap within which the PEO:LiTFSI phase are completely amorphous had been observed for low molecular weight PEO electrolyte[114]. Several crystalline compounds (e.g. 6/1, 3/1, 2/1) can be observed in the high concentration salt-rich region while some of the crystalline structure still remains a subject of controversy.

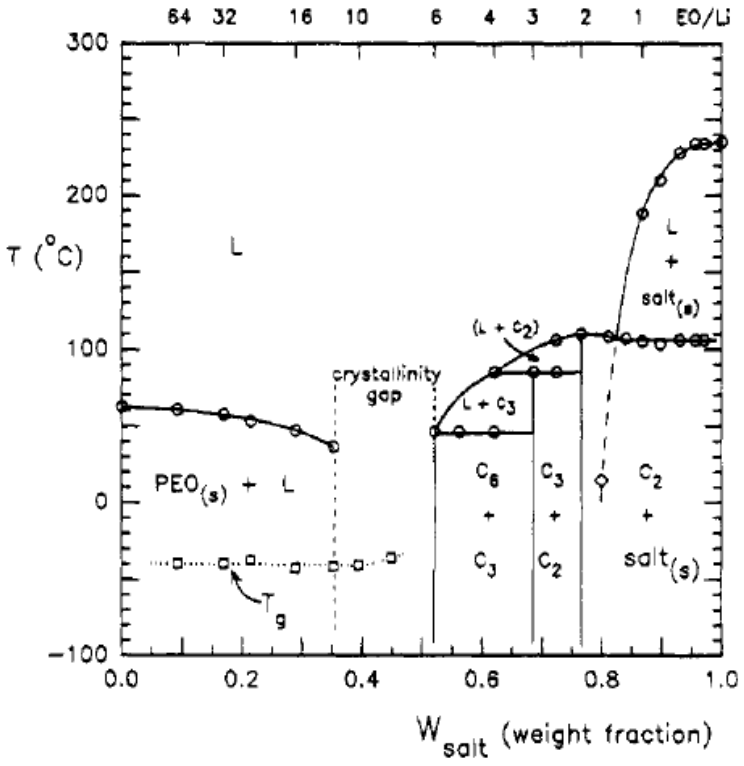

Figure 7.2 Phase diagram of PEO:LiTFSI SPEs, adopted from ref [114].

In this chapter, PSC-SPE containing LiTFSI was prepared through a similar way as PSC-$LiClO_4$ SPE system described in Chapter 6. And the salt concentration was controlled to be within the dilute region within which only crystalline PEO phase and amorphous PEO/Li complex phase co-exist. The objective of this study is: 1) To improve room temperature ionic conductivity of the PSC SPEs by replacing ClO_4^- with a large delocalized TFSI anion in order to minimize ion aggregation and the T_g increase; 2) To study the anion effect on the structure and ionic conductivity correlation of PSC-LiTFSI SPEs.

7.2 Structure and ionic conductivities of PSC-LiTFSI SPEs

7.2.1 Preparation and structural characterization of PSC-LiTFSI SPEs

To prepare PSC-LiTFSI SPEs, PSC films were soaked in 0.1~0.4 wt% LiTFSI pentyl acetate solutions at time intervals varying from 10 to 100 min. LiTFSI has higher affinity with pentyl acetate solvent and therefore the infiltration time for the lithium salt to reach the similar concentration in the PSC film as in the $LiClO_4$ system is much longer. The resultant effective Li^+ to [EO] ratio (<*r*>) was controlled from 0.01 to 0.1 (O/Li molar ratio from 100 to 10) so that all the PSC-SPEs were still within the dilute region as defined in the phase diagram. All the PSC-LiTFSI SPEs were dried under vacuum at room temperature for 5-7 days and transferred to an Argon purged glove box and stored at room temperature prior to any measurements.

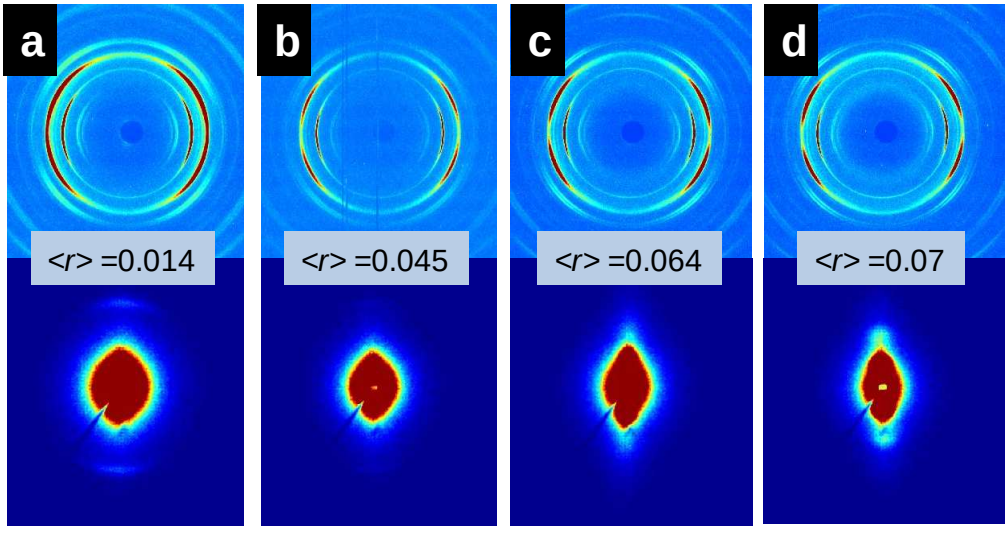

Figure 7.3 (a-d) 2D in-plane WAXD (top row) and SAXS (bottom row) patterns of PSC-LiTFSI SPEs.

The 2D in-plane WAXD patterns in Figure 7.3 (top row) confirm that PEO crystal orientation remains intact. Integrations of the 2D in-plane WAXD patterns in Figure 7.4a reveal that only PEO monoclinic crystalline structure exists in all PSC-LiTFSI SPEs. However, the PEO crystallinity does decrease at higher Li^+ concentration as the amorphous area under the crystalline peaks increased as <*r*> increases. Beside the broad amorphous hump around 15~30° of 2θ under the major crystalline peaks, there is an additional amorphous peak near 10~17° of 2θ and it becomes prominent between <*r*>=0.7~0.94, which likely suggests the crystalline to amorphous transition is directional along certain crystallographic planes.

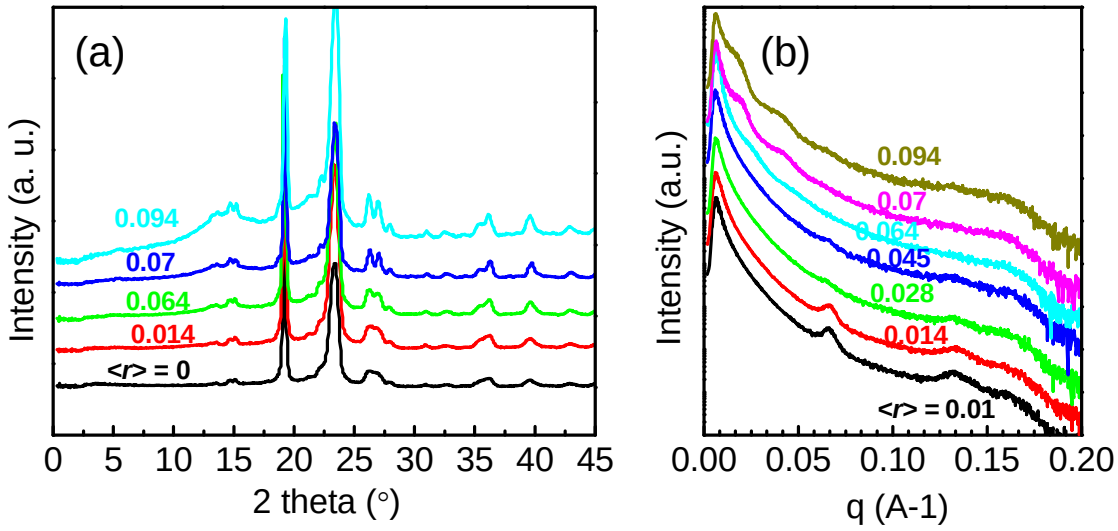

Figure 7.4 Azimuthal integrations of (a) WAXD and (b) SAXS patterns of PSC-LiTFSI SPEs.

It had been proposed in section 6.3 for the PSC-$LiClO_4$ SPE system that at initial low Li^+ concentration, ions have a tendency to infiltrate into the fold region and form

complex with the rigid amorphous loops tethered on the crystalline lamellae surface (schematics in Figure 6.10). This is supported by the fact that the intensity of the SAXS scattering at q= 0.065 $Å^{-1}$ (corresponding to 9.6 nm periodicity) gradually decreases and eventually disappears, since the introduction of the anion decreases the contrast between amorphous loops region and crystalline lamellae. This phenomenon is also observed in the PSC-LiTFSI SPE system. The integrations of SAXS patterns of PSC-LiTFSI SPEs in Figure 7.4b indicate that the critical Li^+ concentration at which the scattering peak at q= 0.065 $Å^{-1}$ completely disappears shifts to much lower <r> (~0.02 for PSC-LiTFSI SPEs compared with <r> ~ 0.06 for PSC-$LiClO_4$ SPE system). This is consistent with the fact that $TFSI^-$ has a higher electron density than ClO_4^-, which could balance the contrast between amorphous loops and crystalline lamellae at much lower ion concentrations.

Another interesting observation is that a large feature of structure in the PSC-LiTFSI SPE systems begins to form at <r> above 0.05 as indicated by the SAXS integrations in Figure 7.4b. Two broad peaks at much lower q-values start to appear at <r> = 0.064, and the intensity of these two peaks increases with further increase of ion concentration. The first order peak corresponds to an average d-spacing of ~ 30 nm, which is nearly as three times as one PEO crystalline lamellar thickness. Since the highest weight percentage of LiTFSI salt in the PSC film is 22 wt% at <r> =0.094, it is unlikely that the volume increase due to the introduction of LiTFSI into the amorphous inter-lamellar region can cause an expansion of periodicity from 10 nm to 30 nm, therefore a different mechanism must be involved. It is speculated that a “super-structure” might be formed at high ion concentrations.

7.2.2 Characterization of the PSC-LiTFSI SPE "Super-structure"

To further understand this "super-structure", 2D in-plane and through-plane WAXD and SAXS measurements were performed on PSC-LiTFSI SPE at <*r*> =0.094. WAXD patterns (Figure 7.5a, b) suggest that the monoclinic PEO crystal structure remains unchanged and the polymer chains are all aligned parallel to the film normal. The 2D in-plane SAXS patterns in Figure 7.5c show a strong anisotropic scattering along meridian direction while the SAXS pattern from on the through-plane direction is isotropic, indicating that this "super-structure" also has strong orientation and it's aligned in the same direction as the PEO lamellae. The elliptical shaped scattering pattern in Figure 5.3c becomes much narrower along the equator direction, suggesting a periodic structure with an even larger lateral size compared with the 20μm PEO single crystal lamellae.

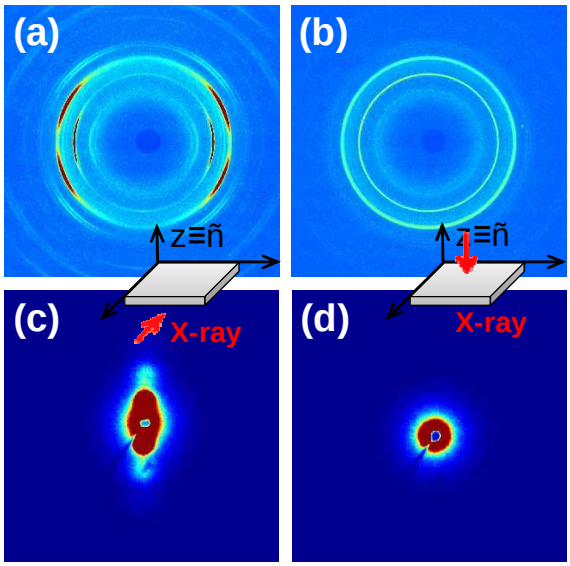

Figure 7.5 2D WAXD (top row) and SAXS (bottom row) patterns of PSC-LiTFSI SPE at <*r*> = 0.094. (a) and (c) are collected when x-ray beam is parallel to film surface; (b) and (d) are collected when x-ray beam is perpendicular to film surface.

Ideally, morphological characterization would be more straightforward to visualize the “super-structure”. However in this case, the hydroscopic nature makes it extremely difficult to directly characterize the morphology and structure of these SPE films using traditional techniques such as cross-section AFM and TEM due to tedious sample preparation procedure. Therefore a few alternative ways had been attempted here in order to better understand the morphology of these PSC-LiTFSI SPEs at relatively high ion content.

In one of our approaches, 0.1 wt% LiTFSI pentyl acetate solution was added into ~0.1 wt% PEO single crystal pentyl acetate solution. The resultant solution was well mixed and spin-coated onto a carbon coated TEM grid and dried in vacuum for 1 day before measurement. Figure 7.6 shows a TEM image of a-few-layer PEO single crystal/ LiTFSI clusters. In contrast to a clean surface that commonly observed for pristine PEO single crystals, the surface of these mixed PEO single crystal/LiTFSI clusters is very heterogeneous. EDXS analysis confirms that LiTFSI salts are present in these structures. The contrast between the dark and light domains could be due to the height difference, and it is likely that PEO crystals in the light area were partially dissolved by LiTFSI at this early stage of perforation.

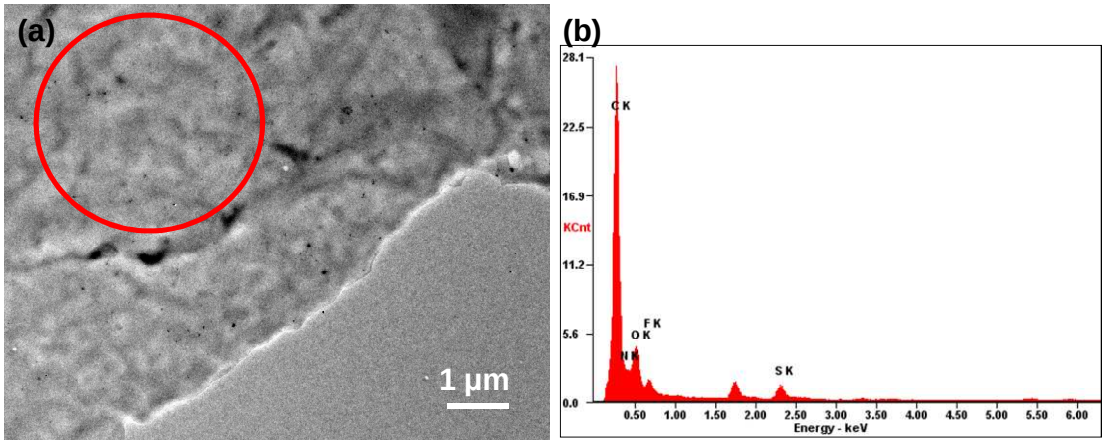

Figure 7.6 Transmission electron micrograph (a) and EDXS analysis (b) of PEO single crystal and LiTFSI mixture in pentyl acetate solution.

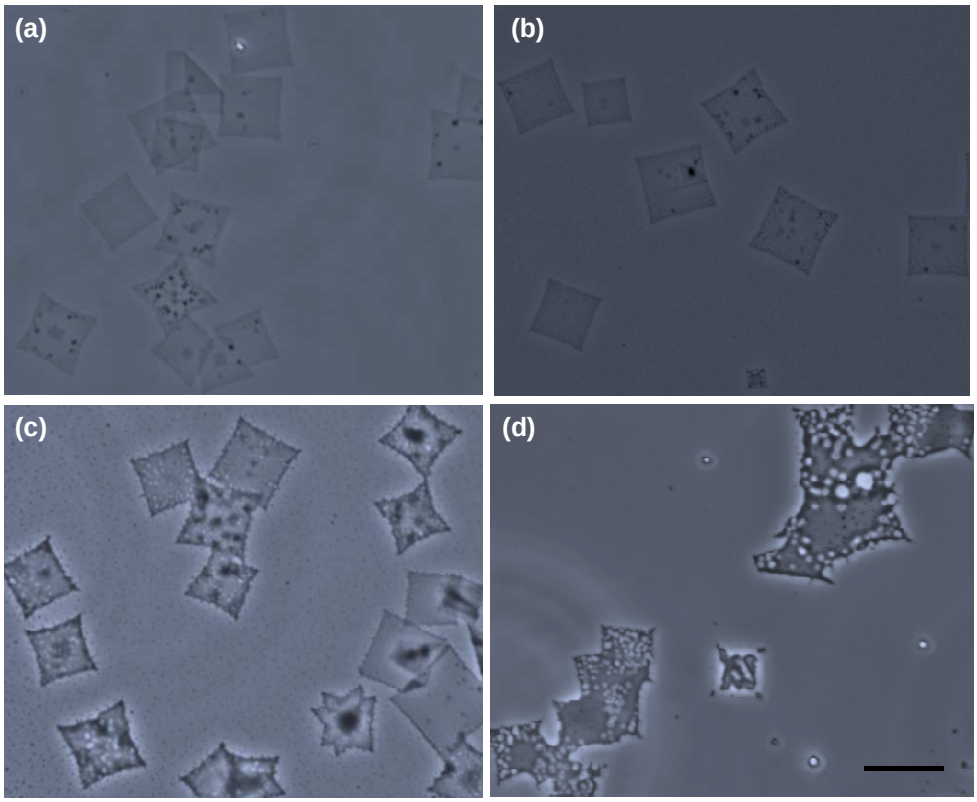

Figure 7.7 Phase contrast microscope images of PEO single crystals. LiTFSI solutions with different concentrations were spun coated onto the PSC substrate. (a) to (d) are microscope images of PEO single crystals after spun coated with 0, 0.27, 0.54, and 1.08 wt% LiTFSI pentyl acetate solution, respectively. Scale bar equals to 20 µm.

A second control experiment is shown in Figure 7.7. LiTFSI pentyl acetate solutions with different concentrations were spun coated onto glass substrates that were pre-deposited with PEO single crystals. When LiTFSI concentration increased, the PEO crystals were partially dissolved as large holes were clearly observed on the crystal surfaces. Despite the fact that the LiTFSI infiltration progress in PSC film was likely to be different from these two supplementary experiments, the results of the latter highly suggest that perforation of PEO crystals is possible to take place at high LiTFSI concentrations.

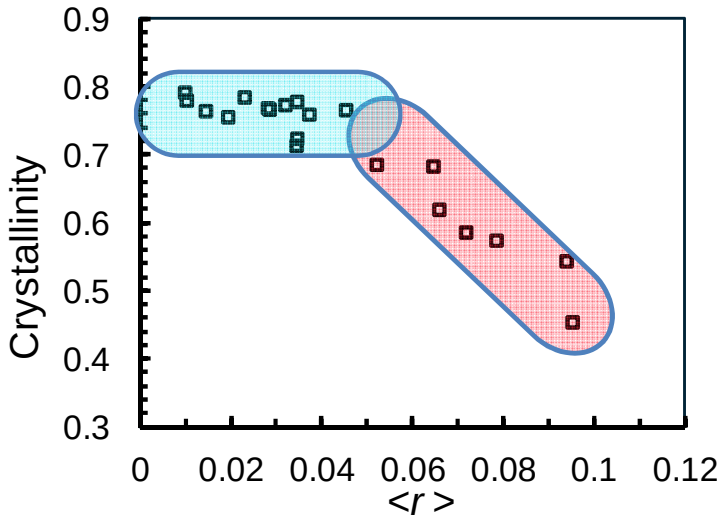

Figure 7.8 Crystallinity of PSC-LiTFSI SPEs as a function of <r>, the crystallinity is calculated from isotropic WAXD integrations.

The crystallinity of PSC-LiTFSI SPEs that determined from the WAXD integrations as a function of <*r*> is plotted in Figure 7.8. The crystallinity remains nearly the same as pristine PSC film (X_c ~ 76%) at <*r*> below 0.05. This is likely due to the

large size of the TFSI anion, within the experimental time scale, PEO crystalline lamellae appear to be impermeable to the ions in dilute region, therefore ions are enriched in the amorphous region and the PEO crystals remain intact. When further increase the ion concentration to <*r*> above 0.05, a quick drop of the crystallinity was observed and it is consistent with the perforation of the PEO single crystals in the microscope measurement.

7.2.3 Proposed mechanism of PSC-LiTFSI "super-structure" formation

Based on all the characterization results discussed above, the effect of LiTFSI on the structure change of PSC film is summarized and mechanism of the "super-structure" formation is proposed. During the infiltration process, ions are first enriched in the amorphous loop regions between PEO crystalline lamellae, resulting in a decreased electron density contrast between the loop region and crystal region and the disappearance of the SAXS scattering at q= 0.065 $Å^{-1}$. When <*r*> further increases to above 0.064, a new periodic structure is observed from the SAXS patterns. This so called "super-structure" has an average periodicity of ~30 nm and also adopts an anisotropic layered structure with the layer normal parallel to the film normal, while the lateral size of the layer is much larger than that of the PEO crystal, as suggested by the shape change on the 2D SAXS pattern.

After ions are saturated within the inter-lamellae amorphous domains, they start to penetrate into the PEO crystals and reduce the crystalline PEO fraction, as confirmed by the decrease of PEO crystallinity from 75% at <*r*>=0.05 to 45% at <*r*>=0.094. The dissolution of the PEO lamellae is likely to be inhomogeneous and it may start from the

weak points, e.g. defects and extended to a whole layer of crystals. Perhaps the crystals are selectively dissolved every one or two layers, resulting in a larger periodicity in average (Schematics of the proposed “super-structure” is shown in Figure 7.9. The “super-structure” is not observed in PSC-$LiClO_4$ SPEs and it is likely because there is not sufficient contrast between the amorphous PEO/Li region and the remaining crystalline lamellae within the concentration range in this study due to the lower electron density of ClO_4^- compared with $TFSI^-$. Further study by varying the anion size and measuring the SAXS patterns would provide better understanding on the origin of this large periodicity formation.

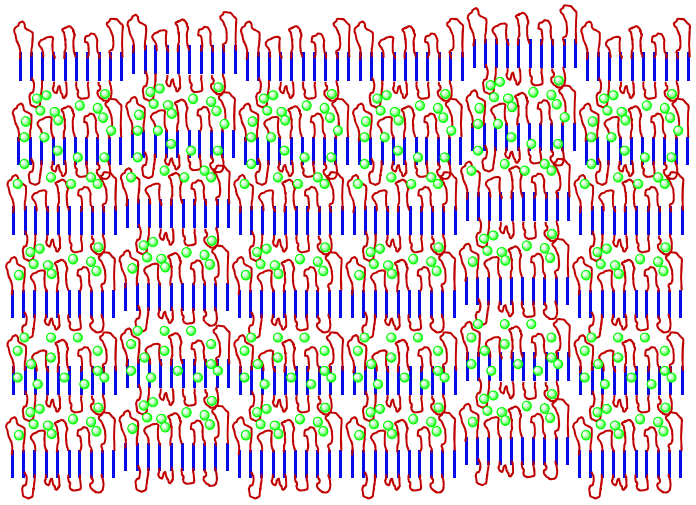

Figure 7.9 Schematics of the proposed “super-structure” in PSC-LiTFSI SPEs at high ion contents, viewed from cross-section of the film.

7.2.4 Structure evolution of PSC-LiTFSI SPEs

Although the integration of WAXD pattern for PSC-LiTFSI SPE at <*r*> =0.094 is only characteristic of pure monoclinic PEO crystalline structure, the curve does show noticeable difference compared with pristine PSC without LiTFSI doping (Figure 7.4a). For the dry SPE that stored at room temperature for 1 week, there is an amorphous bump near 10 ~ 17° of 2θ. Additional crystalline structure had slowly formed after annealing at room temperature for 3 months. Four peaks at 2 θ = 9.3°, 11.4°, 14.7° and 16.3° can be assigned to $P(EO)_6$:LiTFSI crystalline complex as reported elsewhere[63]. And 2D WAXD pattern in Figure 7.10c shows anisotropic scattering from these planes, indicating that the slowly formed 6:1 crystalline complex has certain orientation. It is likely that the polymer chain arrangement is preserved in the initial amorphous state, which further guides the orientation of the subsequent PEO:Li 6:1 crystalline complex after slow crystallization at room temperature. In addition, the peak position gradually shifts to lower *q* value after 3 months annealing in the SAXS integration plot in Figure 7.10b, indicating this "super-structure" is slowly evolving with time into a larger periodicity. Since the fraction of this 6:1 crystalline complex is very low, the majority phase of the PSC-LiTFSI SPE at <*r*> =0.094 is still crystalline PEO.

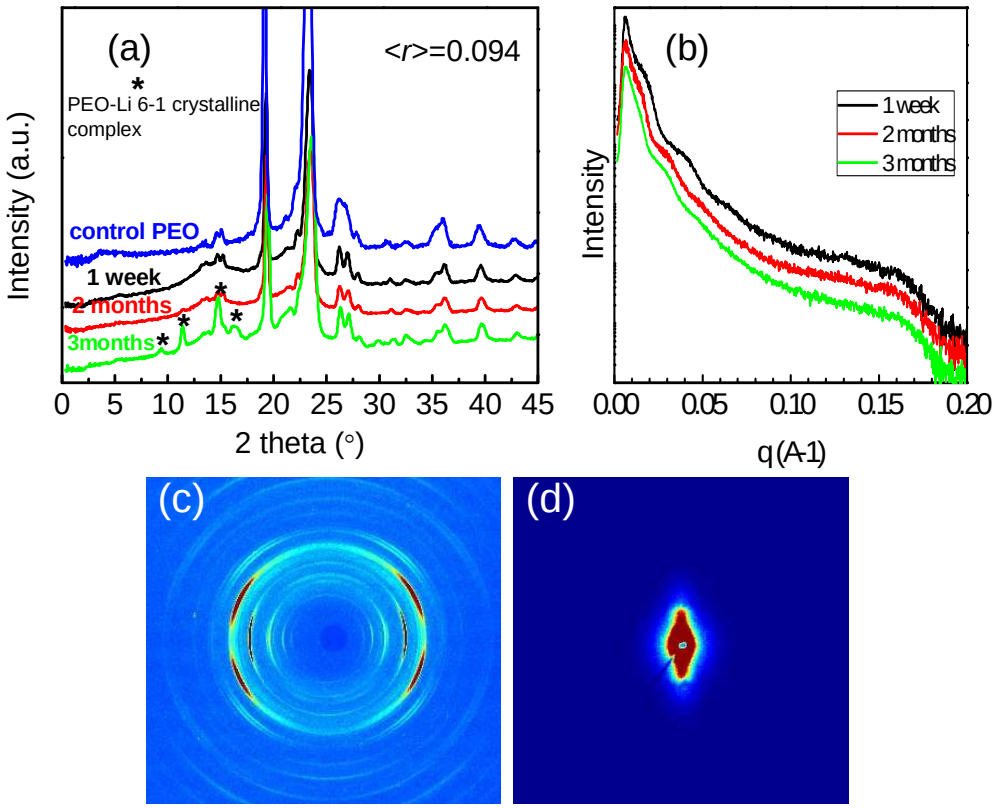

Figure 7.10 (a) WAXD integrations; (b) SAXS integrations of PSC-LiTFSI SPE at <r>=0.094, annealed at room temperature for different time intervals. (c) 2D in-plane WAXD; (d) 2D in-plane SAXS of 3-month-aged PSC-LiTFSI SPE.

WAXD and SAXS were also performed on two additional samples at low and intermediate concentration ranges up to 3 months room temperature aging in order to determine whether there is any structure evolution. <*r*>=0.045 is slight below the critical concentration where both crystallinity and conductivity anisotropy starts to drop. At this concentration, the PEO crystalline lamellae scattering peak at q= 0.065 $Å^{-1}$ is the weakest and no feature of "super-structure" is observed after the initial 1 week aging based on the SAXS results in Figure 7.11b. However, the PEO crystalline lamellae scattering peak completely disappears and a weak sign of "super-structure" starts to appear after 3

months. While the WAXD integrations remains unchanged over 3 months (Figure 7.11a), suggesting that the crystalline structure in dilute electrolyte is stable.

At intermediate concentration (<*r*> =0.066), the intensity of peaks at ~ q = 0.023 and 0.045 $Å^{-1}$ that are characteristic of the "super-structure" is enhanced after 3 month aging in the SAXS plot in Figure 7.11d, indicating that the structure becomes more ordered after rearrangement at room temperature over a long period of time. No PEO:Li 6:1 crystalline complex has been formed even after 3 months at this stoichiometry based on the WAXD results in Figure 7.11b.

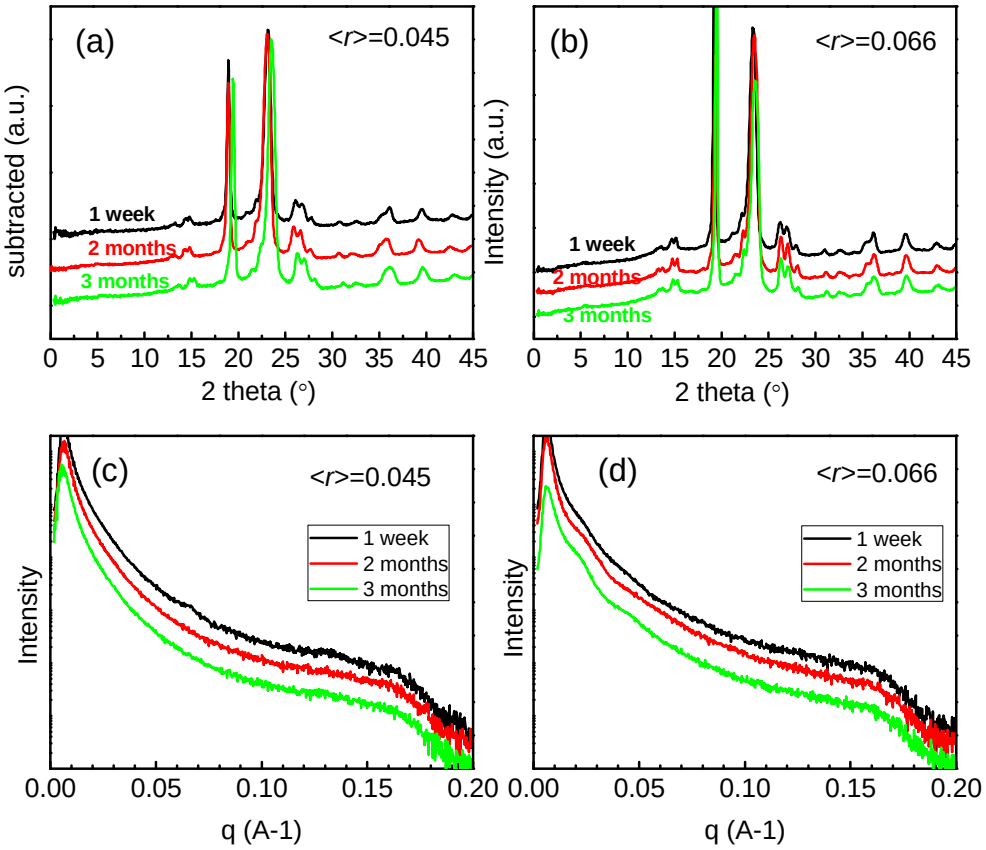

Figure 7.11 WAXD (a, b) and SAXS (c, d) integrations of PSC-LiTFSI SPEs at <r> = 0.045 and 0.066, respectively that annealed at room temperature for 3 months.

7.2.5 Correlation of structure and ionic conductivity in PSC-LiTFSI SPEs

In-plane and through plane conductivities and the anisotropy factor ($\sigma_{//}/\sigma_{\perp}$) of PSC-LiTFSI SPEs are summarized in Figure 7.12. The general behavior of ionic conductivity as a function of Li^+ concentrations is very similar to that observed in the PSC-$LiClO_4$ SPEs previously discussed in Chapter 6: Both $\sigma_{//}$ and $\sigma_{\perp}$ increase with <*r*> and $\sigma_{//}$ is consistently higher than $\sigma_{\perp}$ throughout the entire Li^+ concentration range, which indicates the ion transport along the crystal surface is less affected by crystallization. High conductivity anisotropy on the order of 10^3 ($\sigma_{//}$ / $\sigma_{\perp}$ = 500 to 3,000) is observed for PSC-LiTFSI SPEs in dilute region when <*r*> is below 0.05. Above the critical point ~ <*r*> = 0.05, the conductivity anisotropy quickly dropped to 50-20, with the $\sigma_{\perp}$ increases much faster than $\sigma_{//}$. It is also coincident that PEO crystallinity decreases from 76% to 45% when <r> increases from 0.045 to 0.095. Partial dissolution of the PEO single crystal is further confirmed judging from the steeper slope of $\sigma_{\perp}$ curve and low conductivity anisotropy at high ion content.

This structure-conductivity correlation and the similarity of the conductivity behaviors between the two types of lithium salts imply that the ion conduction in our PSC-SPE system can be simply treated as a phenomenon of small molecule diffusion in a composite matrix, which is significantly affected by the presence of the impermeable fillers. In both PSC-SPE systems, the PEO crystalline lamellae can be considered as the filler that is dispersed within the amorphous PEO matrix. Ions act as small molecules diffusing through the amorphous PEO matrix, and the transport property depends on the geometry of the “PEO lamellae filler”.

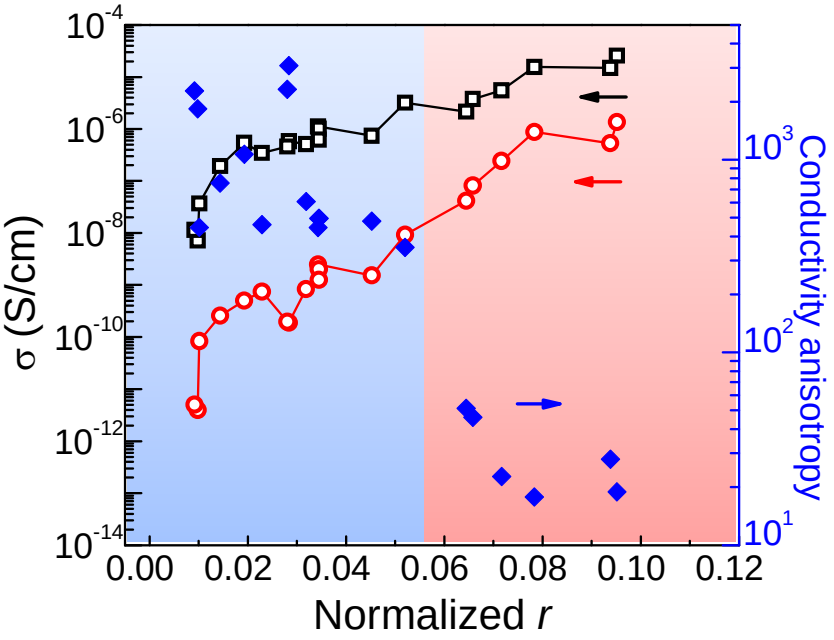

Figure 7.12 In-plane (black open square) and through-plane (red open circle) ionic conductivity of PSC-LiTFSI SPEs and the conductivity anisotropy (blue diamond) as a function of effective Li^+ to [EO] ratio <*r*>.

As expected, PSC-LiTFSI SPEs show improved ionic conductivity from both in-plane and through-plane direction and the enhancement becomes more prominent at higher ion concentrations (Figure 7.12). $\sigma_{//}$ of reaches ~ 0.3 × 10^{-4} S/cm at <*r*> = 0.94, which is comparable with reported conductivity value of 4x10^{-5} for 100% amorphous SPE with low molecular weight PEO (3.9 kDa) [182] and even higher than 0.11x10^{-4} S/cm of the amorphous solution cast SPE with the same PEO (M_w~300kDa) at the same <*r*>. It is noted that $\sigma_{//}$ of PSC-LiTFSI SPEs is nearly two orders of magnitude higher than that of the PSC-$LiClO_4$ SPE at equivalent Li^+ concentration[259]. The enhanced ionic conductivity is due to the plasticizing effect of $TFSI^-$ that results in high polymer chain mobility in the amorphous phase. This is confirmed in Figure 7.13 as PEO remains a

relatively low T_g (~ -40 °C) even at high Li^+ concentrations. Higher degree of ion dissociation and the absence of ion pairs as suggested by Raman spectroscopy study[260] would also be the reason for the observed room temperature conductivity improvement.

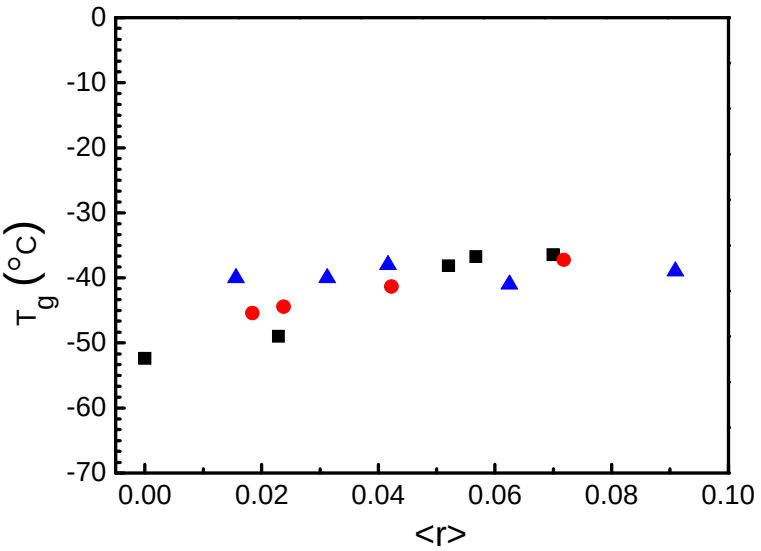

Figure 7.13 Glass transition temperatures of PSC-LiTFSI SPEs (black square); Cross-linked PEO electrolyte with urethane linkage, PEO chain length is 2000 g/mol, replotted from ref. [261](red circle); Semicrystalline PEO (linear) based SPEs prepared by solution casting method, T_g values estimated from ref.[114] (blue triangle).

7.2.6 Temperature dependent ionic conductivities of PSC-LiTFSI SPEs

Two samples representative of dilute and concentrated SPEs were selected for temperature dependent ionic conductivity measurements. Figure 7.14 shows the first heating scans from in-plane and through-plane directions at <*r*> = 0.02 and <*r*> = 0.08. Both in-plane and through-plane curves for the two samples show a typical Arrhenius

behavior, indicating ion hopping is the ion conduction mechanism. Activation energies (E_a) are calculated based on the slope of the curves below 40 °C and are shown in Table 7.1. For both dilute and concentrated SPEs, the E_a calculated from in-plane direction is always slightly higher than its corresponding through-plane direction, suggesting the energy barrier is higher for ions to diffuse perpendicular to the crystal orientation direction. This trend is consistent with that observed in PSC-$LiClO_4$ system discussed in Chapter 6. On the other hand, the through-plane activation energy decreases from 1.35 to 1.13 when <*r*> increases from 0.02 to 0.08, which further supports the perforation of PEO single crystals by excessive lithium salts, resulting in an increase of the amorphous fraction that facilitates ion transport along the through-plane direction with lower activation energy.

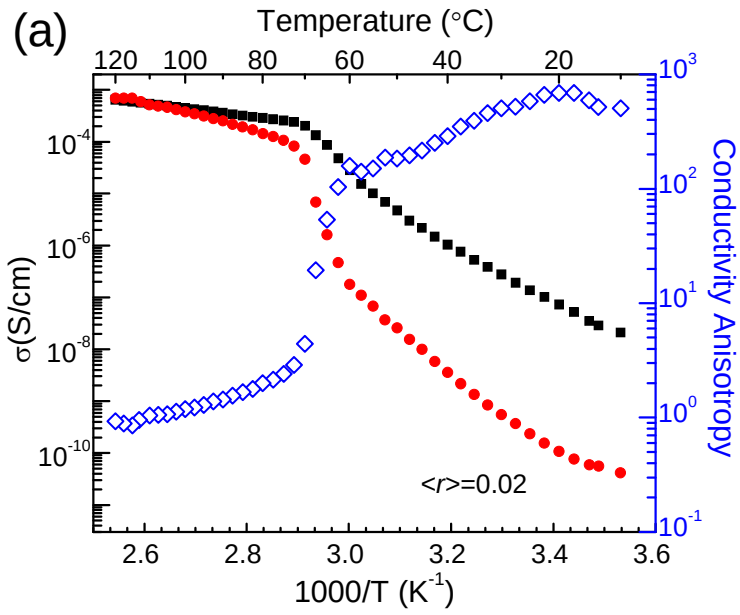

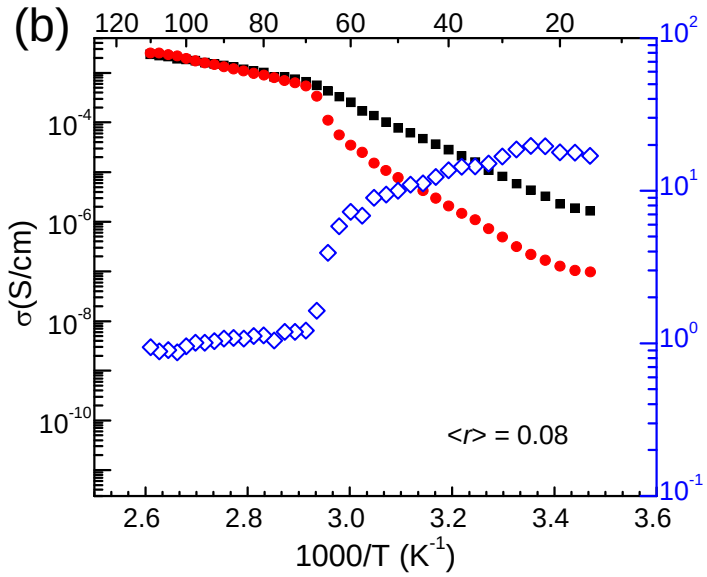

Figure 7.14 First heating scans of PSC-LiTFSI SPEs at (a) <*r*> = 0.02 and (b) <*r*> = 0.08 at 1 °C/min heating rate.

Table 7.1 Activation Energies of PSC-LiTFSI SPEs calculated from the first heating scans.

E_a (eV)	In plane	Through plane
<r> = 0.02	1.19	1.35
<*r*> = 0.08	0.98	1.13

7.2.7 Lithium transference number measurement

The lithium transference number t_+ of PSC-LiTFSI SPEs was measured using electrochemical method. For a binary polymer/salt blend, both cation and anion are mobile and can contribute to the measured ionic conductivity. It is essential to maintain a high cation transference number in order to minimize the development of a concentration polarization across the cell during current flow that would limit the power output of the

battery. In this study t_+ was only measured on a PSC-LiTFSI SPE at <*r*> = 0.08 at room temperature. Measurements on PSC-LiTFSI SPEs with ion concentration <*r*> below 0.08 were not pursued since the impedance of these electrolytes was too high that the current response upon a small d.c. bias was below the signal to noise ratio of the instrument.

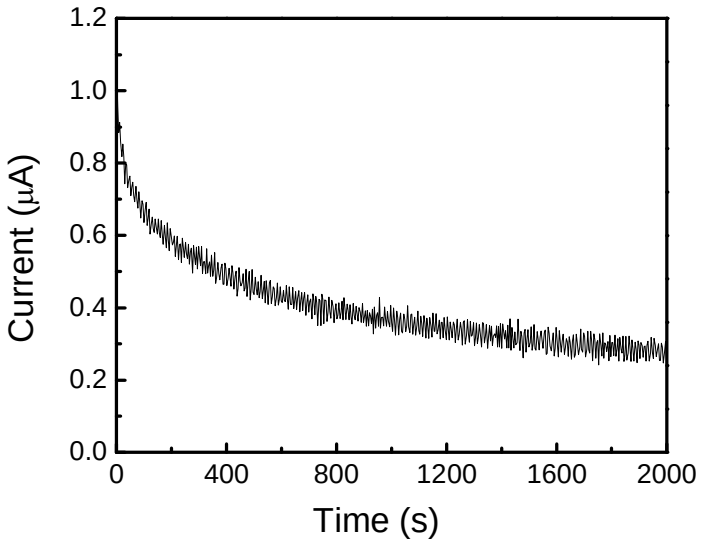

Figure 7.15 Time dependence of the response of the cell current under 50 mV potential polarization at room temperature for PSC-LiTFSI SPE at <r>=0.08.

The electrochemical method to determine t_+ involves a combined a.c. and d.c. measurements that first developed by Vincent and Bruce as discussed earlier in Section 3.3.6.2. The initial (I_0) and steady state (I_s) current can be read from the current profile as shown in Figure 7.15. The a.c. impedance of PSC-LiTFSI SPE at <*r*>=0.08 before and after a small polarization voltage of 50mV are plotted in Figure 7.16. The high frequency semicircle can be assigned to the resistance of the electrolyte (*Re*), and low frequency

semicircle corresponds to the resistance of the passivating layer at the interface (*Ri*)[212, 262]. This is confirmed as the bulk resistance of the electrolyte measured using a normal two-parallel stainless steel-electrode setup nearly overlapps with the high frequency semicircle that measured from the symmetrical Li |electrolyte| Li cell.

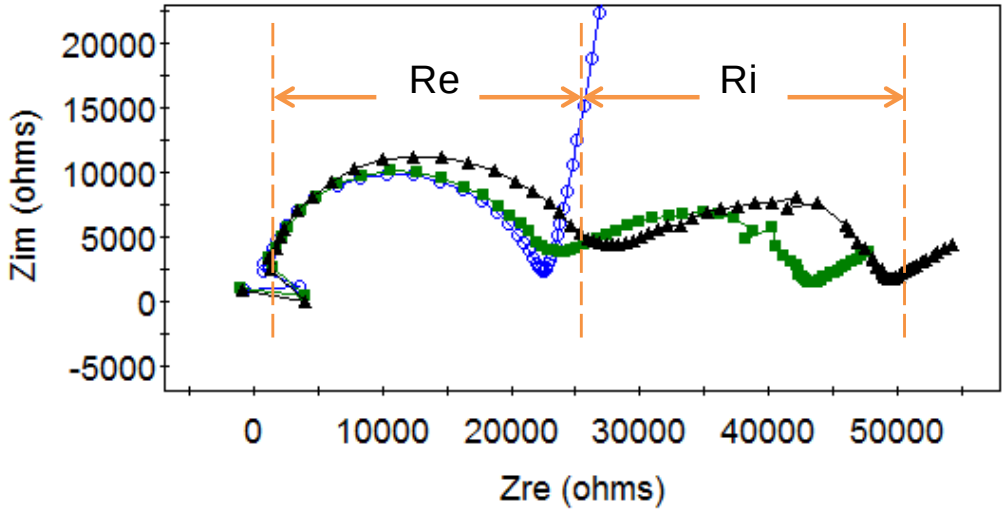

Figure 7.16 The a.c. complex impedance plot of the impedance before d.c. polarization (green solid square) and after d.c. polarization (black solid triangle) on a Li |PSC-LiTFSI SPE| Li cell, measured at room temperature. The blue open circle is the a.c. impedance of the same electrolyte measured on a ss |PSC-LiTFSI SPE| ss cell without Li electrode.

The fitted parameters and calculated results are listed in Table 7.2. The lithium transference number t_+ for PSC-LiTFSI SPE at $<r>=0.08$ was calculated to be 0.25, which is consistent a range of 0.2 ~ 0.4 measured on a plasticized PEO-like electrolyte[215] and PEO-PEG-γ-$LiAlO_2$ electrolyte[263] using the same electrochemical technique. Concentration dependent t_+ on PEO/LiTFSI blends was reported by Edman *et al.*[264] using

a different electrochemical method based on concentrated solution theory; t_+ was found to increase with the increase of ion concentration (from 0.2 to 0.6 when O/Li ratio decreased from 30 to 5) as a results of a decrease in anion mobility with decreasing free volume. The present t_+ result indicates that the crystalline morphology of the single crystal SPE model system does not alter the lithium transport property.

Table 7.2 Summary of lithium transference number measurement results.

	I^0 (μA)	I^s (μA)	R_e^0 (kΩ)	R_e^s (kΩ)	R_i^0 (kΩ)	R_i^s (kΩ)	V (V)	t_+
PSC-LiTFSI SPE at <r>= 0.08	1.0	0.3	24.1	28.4	20.0	22.7	0.05	0.25

7.3 Summary

In this study, PSC-SPEs containing LiTFSI, a lithium salt with large delocalized anion had been prepared, the structure and ionic conductivity were characterized and compared with the PSC-SPE system containing $LiClO_4$ discussed in Chapter 6. A few common features between these two systems have been observed:

- In both PSC-SPE systems, the introduction of lithium salt does not change the PEO crystal structure. But the crystallinity of the PSC-SPEs gradually decreases as salt concentrations increases due to the strong polymer-salt interaction that partially disrupts the crystalline lamellae.

- The scattering peaks in SAXS arise from the electron density fluctuation between crystalline lamellae and amorphous loop-lithium salt complex. Increasing the salt concentration reduces the contrast between crystalline lamellae and amorphous PEO-lithium phase, resulting in a decrease and eventually disappearance of the scattering peak intensities.
- In both PSC-SPE systems, in-plane conductivity is consistently higher than through-plane conductivity throughout the entire Li^+ concentration range that have been investigated in this study. The conductivity anisotropy is on the order of 10^2~10^3 at low Li^+ concentrations and drops one or two magnitude after certain threshold. And this anisotropy is attributed to the tortuosity imposed by the highly oriented PEO single crystals.
- The dynamic effect for both systems is significant in dilute region and seems to be diminished when the Li^+ concentration increases.

There are also quite a few distinct differences between the two salts and are summarized as follows:

- The scattering peaks in SAXS disappear at lower $<r>$ in PSC-LiTFSI SPE compared with PSC-$LiClO_4$ SPE due to higher electron density of the TFSI anion.
- The onset of conductivity anisotropy drop for PSC-LiTFSI SPE shifts to higher $<r>$ compared with PSC-$LiClO_4$ SPE since it's more difficult for the large $TFSI^-$ anion to penetrate into PEO crystals than the ClO_4^- anion.
- PSC-LiTFSI SPEs have higher conductivity than PSC-$LiClO_4$ SPEs at a given $<r>$ and the difference becomes more pronounce at high ion concentrations. The

large delocalized TFSI anions facilitate ion dissociation and act as a plasticizer to maintain a low T_g of PEO as expected, resulting in an enhanced overall ionic conductivity compared with the $LiClO_4$ system.

- At concentrated region, a novel "super-structure" with ~ 30 nm periodicity is observed for the first time in PSC-LiTFSI SPEs and it is likely responsible for the increased through-plane conductivities and decreased anisotropy at high Li^+ concentrations.

At last, it is notable that the in-plane room temperature conductivity of PSC-LiTFSI SPE at $<r>$ =0.094 reaches $0.3x10^{-4}$ S/cm, which is slightly higher than the conductivity value of $0.1x10^{\wedge 4}$ S/cm for its 100% amorphous counterpart while the former consists of ~40% crystalline phase. Compared with the soft and tacky amorphous electrolyte, our PSC SPE appears to be advantageous since the remaining crystallinity would provide adequate mechanical integrity with minimum effect on the ion conduction. The results suggest that semicrystalline polymers can be used for high performance solid polymer electrolyte design if the crystalline morphology is well controlled and appropriate lithium salt is selected.

CHAPTER 8: **CONDUCTION MECHANISM OF PEO SINGLE CRYSTAL SPE MODEL SYSTEMS**

8.1 Introduction

In the previous chapters, a model electrolyte containing stacks of PEO single crystals with precisely controlled shape and orientation, namely PSC-SPE had been developed, and the structure and ionic conductivity of PSC-SPEs containing two distinct types of lithium salts had been studied and compared. The results have brought a clear picture of how crystallization affects ion transport in semicrystalline SPEs. The two factors that restrict ion conduction, tortuosity and chain dynamics, can be fully decoupled by controlling the crystalline morphology.

In this chapter, in-depth analysis on the ion conduction mechanism of these PSC-SPE model systems is further conducted. A modified Nielsen's model has been employed here to quantify the tortuosity/structure effect; while the dynamic effect can be explained from a molecular structure point of view. Finally a generic ionic conductivity expression for well defined semicrystalline SPEs is proposed.

8.2 Quantifying tortuosity/structural effect

In order to quantitatively understand this structural/tortuosity effect in our PSC-SPE systems, a modified Nielsen's model, which is typically used to describe the relative permeability in polymer nanocomposites containing platelet like nanofillers[265-267] is adopted:

$$R_p = \frac{1-\phi_s}{1+\frac{L}{2W}\left(1+\frac{b}{L}\right)^3 \phi_s \left(\frac{2}{3}\right)\left(S+\frac{1}{2}\right)} \tag{8.1}$$

Where b is the edge-to-edge distance between nanofillers and L is the lateral length of the platelet filler, when $b << L$, equation 8.1 can be simplified as follows:

$$R_p = \frac{1-\phi_s}{1+\frac{L}{2W}\phi_s \left(\frac{2}{3}\right)\left(S+\frac{1}{2}\right)} = R_\sigma \tag{8.2}$$

where R_p is the relative permeability of the nanocomposite compared with pristine polymer; ϕ_s is the volume fraction of the filler; L/W is the aspect ratio of the filler; S is order parameter of the filler and is defined as $S = ½\langle 3\cos^2\theta - 1\rangle$, where θ is the angle between the platelet normal and the diffusion direction.

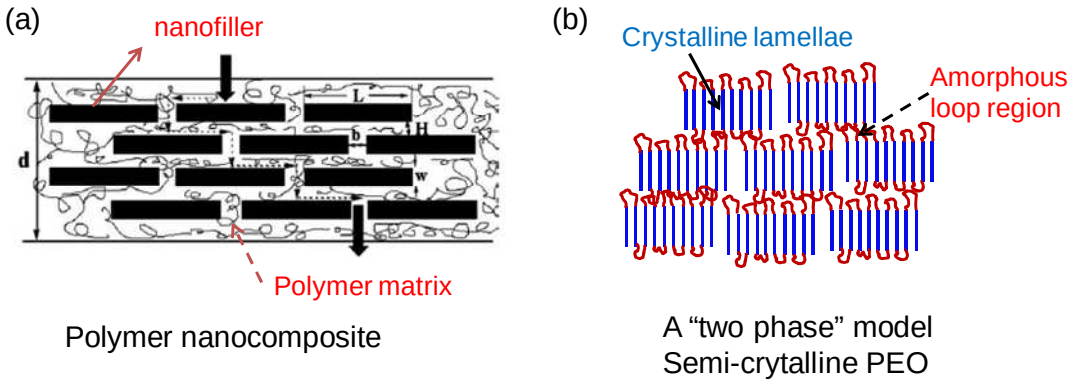

Figure 8.1 Comparison of the morphology between (a) A polymer nanocomposite containing platelet nanofillers, modified from ref.[267]; (b) A "two phase" model consists of stacks of PEO single crystals.

If we treat the crystalline portion of the 2D PEO single crystals as platelet-like nanofillers, and the amorphous fold regions as the matrix, equation (8.2) can be used to describe the relative permeability of lithium ions diffusing through the single crystal SPE compared with an amorphous matrix. In the case of our PSC-SPEs, since the average lateral size of the single crystals used in both Chapter 6 and 7 is ~ 20 μm and the lamellae thickness determined by SAXS is ~ 10 nm, the aspect ratio $L_{\perp}/W_{\perp}$ is 2,000 and $L_{//}/W_{//}$ is 1/2000. The order parameter S determined by the 2D WAXD (Figure 6.7) is 0.8. □s can be treated as the crystallinity X_c determined by WAXD and varies with Li^+ concentrations. The anisotropy factor $\sigma_{//}/\sigma_{\perp}$ equals to $R_{\sigma//}/R_{\sigma\perp}$, where R_{σ} is the tortuosity factor due to PEO crystal orientation, which accounts for the structural effect. Since $L_{//}/W_{//} << 1$, the anisotropy factor $\sigma_{//}/\sigma_{\perp}$ for 20 μm PSC-SPEs can be expressed as follows:

$$\frac{\sigma_{//}}{\sigma_{\perp}} = \frac{R_{\sigma_{//}}}{R_{\sigma_{\perp}}} = 1 + \frac{L_{\perp}}{2W_{\perp}}\phi_s\left(\frac{2}{3}\right)\left(S + \frac{1}{2}\right) = 1 + 866 \times \phi_s \qquad (8.3)$$

The calculated and measured conductivity anisotropy values are listed and compared in Table 8.1. The calculated value fits quite well with the measured anisotropy at lower <r> below 0.02 for PSC-$LiClO_4$ SPEs and <r> below 0.05 for PSC-LiTFSI SPEs with 20 μm single crystal size. A set of control PSC-$LiClO_4$ SPEs consist of 2 μm single crystals (aspect ratio of 200) were also prepared and the conductivity anisotropy was nearly constant at ~ 100 throughout the entire concentration range even at low <r>, confirming that this model is appropriate to describe the ion transport behavior in a semicrystalline model system in dilute region.

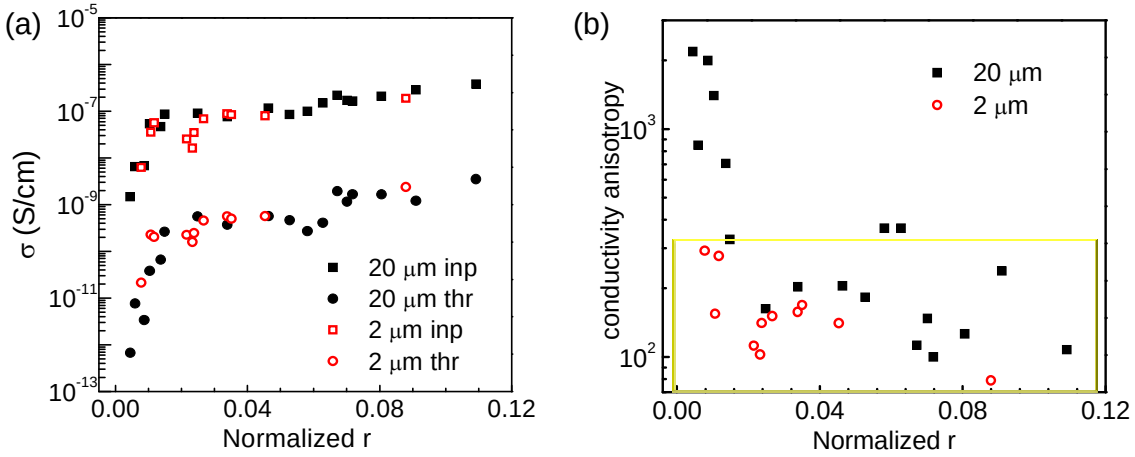

Figure 8.2 (a) In-plane and through-plane ionic conductivities; (b) conductivity anisotropies of PSC-$LiClO_4$ SPEs consists of 20 μm (black square and circle) and 2 μm (red square and circle) single crystals.

On the other hand, significant departure from the model was observed at high ion concentration region for both PSC-SPEs. Perforation of the lamellae at higher ion contents is one possibility that can contribute to the anisotropy drop. The ClO_4^- are much smaller compared with the bulky $TFSI^-$ anions, therefore may tend to penetrate through the PEO crystals at a relatively low concentration. This is consistent with the fact that the critical concentration of anisotropic drop is at $<r> \sim 0.02$ for PEO-$LiClO_4$ SPE system and is at 0.05 for PEO-LiTFSI SPEs. The "super-structure" formation of the latter may also be one reason for the discrepancy of Nielsen's model at high ion concentrations.

In addition, note that Nielsen's model is usually used to describe non-interacting gas molecules diffusing through a composite system and is only valid when the molecule size is much smaller than the nanofiller dimension. The model stands well for the low ion concentration single crystal SPEs, where the small sized Li^+ ions (radius of 0.09 nm) are well solvated and separated by the polymer. However, it is common that for PEO/Li

blend electrolytes, especially PEO/$LiClO_4$ system, ions tend to aggregate into ion pairs/clusters with average size on the order of a few angstroms to a few nanometers when <*r*> increases and ion-ion interactions cannot be neglected at higher <*r*>[80, 268], introducing possible uncertified parameters for Nielsen's model at high <*r*>.

Table 8.1 Comparison of calculated and measured conductivity anisotropy.

	<r>	**□s**	**$L_\perp/W_\perp$**	**S**	**Calculated $\sigma_{//}/\sigma_\perp$**	**Measured $\sigma_{//}/\sigma_\perp$**
PSC-$LiClO_4$ SPEs	0.006	0.75	2000	0.8	650	847
	0.014	0.79	2000	0.8	691	706
	0.05	0.76	2000	0.8	659	182
	0.09	0.60	2000	0.8	514	147
	0.02	0.77	200	0.65	60	112
	0.09	0.65	200	0.65	50	78
PSC-LiTFSI SPEs	0.009	0.78	2000	0.8	676	445
	0.014	0.76	2000	0.8	663	756
	0.05	0.68	2000	0.8	608	350
	0.09	0.54	2000	0.8	472	27

Instead of Nielsen's permeability model, the effective medium theory (EMT) has been widely used to explain ion conductivity in polymer blends and block copolymers[163]. EMT was originally developed to describe conduction in inhomogeneous binary metallic mixtures, and was later applied to different types of transport situations, including thermal conduction and oxygen diffusion[269-270]. It assumes a random, isotropic medium and replaces the heterogeneous medium with a homogeneous effective medium. The

local heterogeneities in conductivity of the actual system are treated as fluctuations in an effective medium with an effective conductivity equal to the measured one. Based on EMT, if one assumes that the ions are only located in one phase, the effective conductivity σ can be written as:

$$\sigma = f\phi_c\sigma_0 \tag{8.4}$$

Where σ_0 and ϕ_c are the intrinsic conductivity and the volume fraction of the conducting phase. *f* is the morphological factor. For lamellar block copolymers, *f* = 2/3, and it is 1/3 for hexagonally packed cylinder structures. Note that this conclusion is based on the following assumptions: (i) the length scale of the heterogeneities is much less than the length scale of the medium; (ii) the orientation of the small-scale domains is uncorrelated; and (iii) the interaction among the domains can be neglected. These assumptions apparently do not apply to our polymer single crystal SPEs systems, whose ion transport phenomenon can be better described by the Nielsen's model.

Nevertheless, of interest is to compare Nielsen's model with EMT for isotropic samples. For the Nielsen's model, if we set *S* = 0 for isotropic sample, equation 8.2 can be written as:

$$R_p = \frac{1-\phi_s}{1+\frac{L}{6W}\phi_s} = R_\sigma \tag{8.5}$$

Comparing equations 8.4 and 8.5, and noting that $R_\sigma = \sigma/\sigma_0$, $\phi_c = 1 - \phi_s$, it can be concluded that the morphological factor from the Nielsen's model is $\frac{1}{1+\frac{L}{6W}\phi_s}$. It is evident that this morphological factor depends on the volume fraction and geometric

shape (aspect ratio) of the insulating phase. Assuming $L=W$, ϕ_s = 50% the morphological factor is calculated to be 0.92, greater than the above mentioned 2/3. This perhaps is because that the Nielsen model assumes isolated insulating fillers in a continuous conductive phase. Experimentally, numerous reports have shown that the morphological factor may be much smaller than the values predicted by both theories, ranging from 0.01 – 0.67[169, 271] and the discrepancies are typically attributed to the poor connectivity between microdomains, which leads to lower measured conductivity for isotropic samples[26, 169]. Also for block copolymers, or polymer blends SPEs, the thickness of the films used for the conductivity measurement may be not significantly greater that individual grains. This might introduce additional errors for applying EMT in these systems.

8.3 Quantifying dynamic effect

The tortuosity effect is straight forward and can be explained quite well by employing Nielsen's relative permeability model at relatively dilute lithium concentration. However, the dynamic effect observed in our system is seemingly contradictory to the prevailing view that crystallization slows down the segmental dynamics of the polymer, which significantly decreases the ionic conductivity. We further interpret this dynamic effect from the polymer molecular structure point of view.

In our single crystal SPEs, the conducting phase consists only of rigid amorphous loops that are attached on the lamellae surface and ion conduction is achieved through hopping from one adjacent site to another. Based on the 7_2 helix conformation of PEO chain, the monoclinic unit cell with c = 1.948 nm (Figure 8.3), and the thickness of the

fold layer, we can estimate that there are ~ 8 EO units per loop. In the dilute ion region, *i.e.* <*r*> = 0.01 and the effective EO to Li ratio is 100:1, there are ~ 12 loops per Li^+ on the crystal surface. Considering Li^+ ions are confined between two fold surfaces, each Li^+ ion therefore has to hop over ~ 2-3 loops, or approximately ~1 nm, to reach another ion as shown in Figure 8.4. It would be more energetically difficult for these tethered segments to adjust their local conformation in order to assist the multiple hopping of each ion compared with amorphous SPEs.

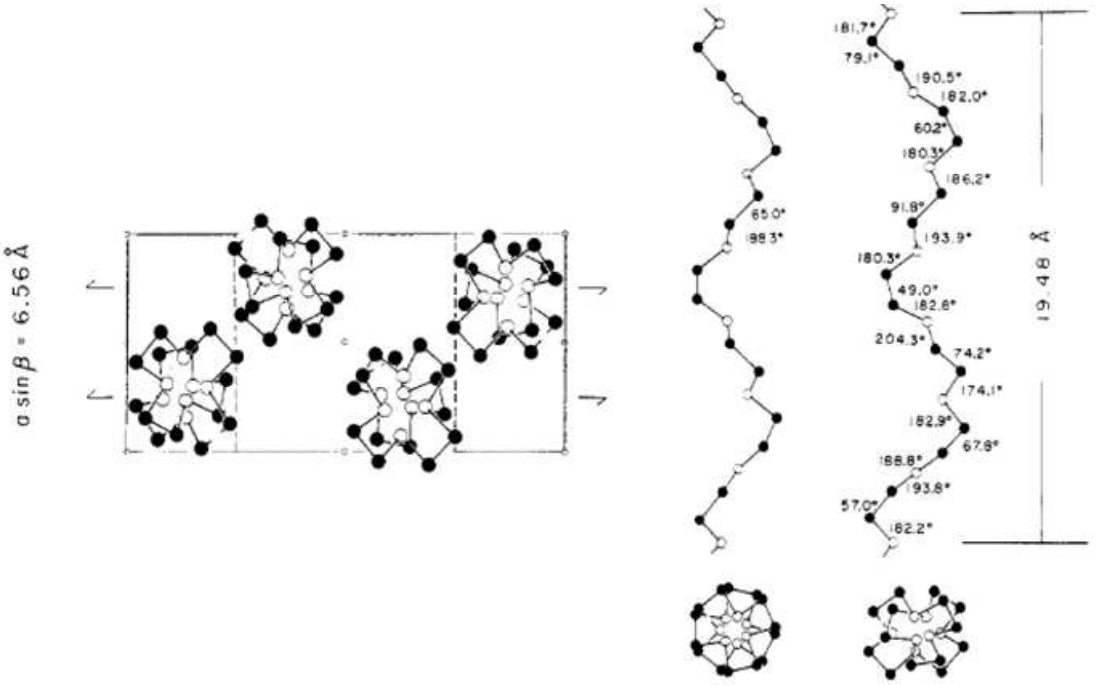

Figure 8.3 Monoclinic unit cell of PEO crystal, cited from ref. [223]

This assumption is also supported by our temperature dependent conductivity measurement for PSC-$LiClO_4$ SPEs as discussed in Chapter 6: the activation energies of

PSC SPEs at <*r*> = 0.01 are 0.86 to 1.06 eV, while only ~ 0.3 eV for amorphous SPE. However, at higher salt concentration, <*r*> = 0.11 for example, there is approximately one Li^+ ion per loop; Li^+ can therefore efficiently hop among PEO loops. The tethered chain effect seems to be overwhelmed by the cross-linking introduced by the Li^+ ions themselves, and the only effect of crystallization on the overall conductivity of SPE is tortuosity. Furthermore, the molecular conformation of the loop and the typically cross linked amorphous PEO are likely different. The loops are well defined and locally pinned between the adjacent crystalline stems, while the linear amorphous PEO, even cross linked, may undergo long semi-long range reptation. Future study will be focused on how these well-defined molecular loops guide ion transport.

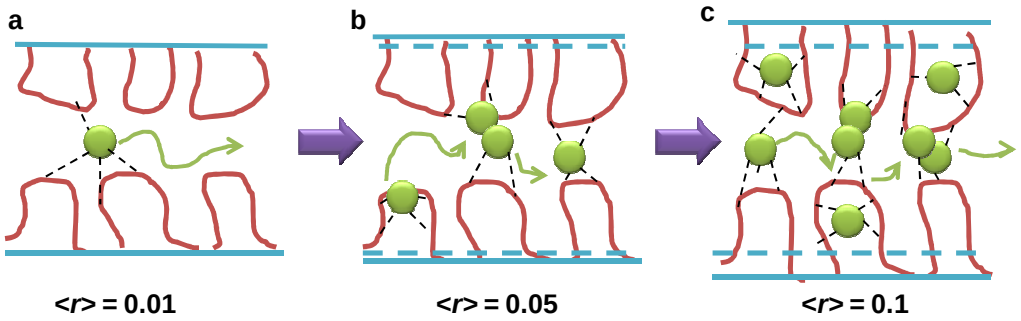

Figure 8.4 Illustration of the ion conduction mechanism within the chain folds between crystalline lamellae at different ion concentrations in PEO single crystal SPEs. (Anions are omitted for clarity.)

8.4 Generic conductivity equations for PSC-SPEs

To this end, a generic expression for ionic conductivity of the semicrystalline SPE is introduced, taking into account both structural and dynamic factors:

$$\sigma = \frac{1}{k} \times \sigma_0 \times R_\sigma = \frac{1}{k} \times \sigma_0 \times \frac{1-\phi_s}{1+\frac{L}{2W}\phi_s\left(\frac{2}{3}\right)\left(S+\frac{1}{2}\right)} \tag{8.6}$$

Where σ, and σ_0 are the ionic conductivities for semicrystalline and the corresponding amorphous SPEs, respectively.

Since the aspect ratio *L/W* for $\sigma_{//}$ for the present system is <<1, $\sigma_{//}$ can be simplified as:

$$\sigma_{//} \approx \frac{1}{k} \times \sigma_0 \times (1-\phi_s) \tag{8.7}$$

Equation 8.7 suggests that for a semicrystalline polymer electrolyte with high degree of crystal orientation, the reduction of conductivity along the crystal surface is attributed to the tethered chain/dynamic effect and the crystallinity. Most of the electrolyte systems only become practically useful in relatively concentrated region, in which considerable conductivity is reached. In this region, the tethered chain/dynamic effect is nearly negligible since the value of calculated coefficient *k* is nearly unity when <*r*> is between 0.09 and 0.1 in the case of both PSC-$LiClO_4$ SPEs and PSC-LiTFSI SPEs. Therefore it can be concluded that the in-plane conductivity is nearly unaffected by crystallization in well-aligned semi-crystalline electrolyte systems. The conclusion based on the present study seems very attractive. If one can design a semicrystalline polymer electrolyte with the crystal orientated parallel to the ion diffusion direction between two electrodes, the same conductivity level as its amorphous counterpart could be reached while the crystallinity provides adequate mechanical support to mitigate the lithium dendrite growth problem commonly seen in Li-metal batteries.

CHAPTER 9: **CONCLUSIONS AND OUTLOOKS**

9.1 Major findings

Crystallization has significant impact on the ion transport in PEO based homopolymer SPEs. We suggest that in addition to the well-known reduction of polymer segmental dynamics due to crystallization, PEO crystal orientation is also a critical factor that affects the overall ionic conductivity. In this thesis, several semicrystalline PEO based solid electrolytes with controlled morphologies have been explored and systematically studied. A solution cast PEO-$LiClO_4$ SPE was first prepared by a slow solvent evaporation method under appropriate temperature and vacuum. Moderate PEO chain alignment was observed and was correlated with the observed conductivity anisotropy between in-plane and through-plane directions. PEO crystal orientation was further improved using a GO/PEO nanocomposite SPE, resulting in an improved conductivity anisotropy. To move forward, a model system consists of well-stacked PEO single crystals with uniform size and large aspect ratio (named PEO single crystal SPEs or PSC SPEs) had been developed in order to gain a more fundamental understanding of ion transport mechanism in semicrystalline PEO electrolyte. The model system allows the quantifying and decoupling of the two factors, namely tortuosity/structural effect and tethered chain/dynamic effect that PEO crystallization had brought to ion conduction in solid polymer electrolyte.

The major findings are listed below:

- In a solution cast linear $P(EO)_{12}$:$LiCO_4$ SPE, PEO crystallizes in the form of spherulite morphology. However, the polymer chain does align perpendicular to the film surface in a moderate degree as suggested by the 2D in-plane WAXD pattern and the Herman's orientation factor f_{120} was calculated to be 0.35. A conductivity anisotropy $\sigma_{//}/\sigma_{\perp}$ of ~10 was observed and can be ascribed to the morphology of the semicrystalline SPE.
- The purpose of adding the two dimensional GO nanofillers into the electrolyte is two-fold: 1) Directly confine ion transport; 2) Confine PEO crystal orientation that further template ion transport. A 10wt% GO-$P(EO)_{12}$:$LiClO_4$ nanocomposite SPE was prepared using a similar solution casting method as the first case. The nanocomposite SPE showed both improved ionic conductivities and conductivity anisotropy (anisotropy factor ~ 70 for nanocomposite SPE compared with 10 of PEO SPE). The enhanced conductivity (especially from in-plane direction) can be attributed to the higher degree of PEO crystal orientation as well as GO orientation that facilitated ion transport along the in-plane direction. In addition, the nanocomposite SPE exhibited slightly lower crystallinity (X_c = 18% compared with X_c = 28% for PEO SPE as determined by DSC) and slower crystallization kinetics as suggested by the isothermal crystallization study, which results in a higher fraction of conducting phase that contributs to the increased in-plane conductivity of the nanocomposite SPE compared with solution cast PEO SPE.
- The two major factors, tortuosity/structural effect and tethered chain/dynamics effect that PEO crystallization imposes on the overall conductivity had been fully decoupled and quantified using a delicately designed PEO single crystal SPEs.

Conductivity anisotropy of 10^2~10^3 was observed at low Li^+ concentrations, demonstrating the directed ion transport by individual lamella. A modified Nielsen's model, which is typically used to describe the relative permeability in polymer nanocomposites containing platelet like nanofillers had been employed to describe the ion transport the highly oriented PSC-SPEs and it fits very well with the observed conductivity anisotropy in dilute SPEs. The tethered chain effect on conductivity due to crystallization had also been quantified by comparing the in-plane conductivity value with that of its amorphous counterpart. In contrary to the prevailing view, the dynamic effect is negligible at relatively high ion content and the conductivity is affected by both strong Li-PEO interaction and Li ion aggregations.

- PSC-SPEs containing two types of salts, $LiClO_4$ and LiTFSI were studied and the anion effect on the structure/conductivity of PSC-SPEs was compared. PSC-LiTFSI SPEs exhibit enhanced ionic conductivity compared with the $LiCO_4$ system and a novel "super-structure" with ~30 nm periodicity was observed at relatively high ion content. The in-plane conductivity of PSC-LiTFSI SPE at $\langle r \rangle$=0.94 reached $0.3x10^{-4}$ S/cm, which is very close to the required value for lithium battery application.

9.2 Recommended future work

To continue with our GO/PEO nanocomposite SPE and PSC-SPEs work, there are a few studies that are not covered in this thesis but are highly recommended to conduct:

9.2.1 Study of polymer dynamics and ion mobility using neutron scattering

In solid polymer electrolyte, the Li^+ diffusion is assisted by the ether oxygen moiety on the PEO backbone and the individual ion jump is estimated to be on a few nanosecond timescale. Quasi-elastic neutron scattering (QENS) measures the polymer chain mobility in nanosecond timescale and therefore can provide very useful information to understand the ion transport in SPEs. The amorphous loops in our PEO single crystal SPEs are covalently tethered to the crystalline lamellae surface and the chain conformation of these loops are very likely to be different from that of the amorphous chains in solution cast PEO SPEs. Obtaining the polymer dynamics information from QENS measurements would be helpful to understand the ion transport within the loop regions in our PSC-SPEs.

9.2.2 Mechanical property characterization of semicrystalline SPEs

Maintaining adequate mechanical integrity of the SPEs is critical to mitigate the lithium dendrite formation problem commonly found in lithium-metal batteries. However, characterizing the mechanical property of the SPEs and acquiring reliable results are challenging due to the hydroscopic nature of the films. Only a limited number of publications have reported the mechanical properties and the most common method is shear modulus measurements at high temperature using rheometer. It is recommended to obtain the modulus information of our nanocomposite and PSC-SPEs and compare with the amorphous SPEs as well as BCP, ceramic nanoparticle systems in order to assess the significance of using semicrystalline PEO for battery applications.

9.3 Outlook

The concept of polymer crystalline lamellae directed ion transport is relatively new and there is a lot of room for further development. In the GO/PEO nanocomposite SPE work, the GO served as a geometric constrain for both ion transport and PEO crystalline lamellae orientation, however, many other functionalities of GO had not been fully utilized. Taking advantage of the rich surface chemistry, the pristine GO can be further functionalized. For example, Fe_3O_4 magnetic nanoparticles can be immobilized onto GO surface and the orientation of GO can be easily controlled to be either parallel or perpendicular to the membrane surface under appropriate magnetic field. Another example is to fix the anion onto GO surface and the nanocomposite SPE would become a single ion conductor.

On the other hand, using the PEO single crystal SPEs as a model system to study ion transport in semicrystalline PEO SPEs is unique and this work can also be extended for more fundamental study. One example is to understand the loop effect on ion transport. A BAB diblock polymer, such as poly(ε-caprolactone)-*b*-poly(ethylene glycol)-*b*-poly(ε-caprolactone) (PCL-*b*-PEG-*b*-PCL) can be used to as a model system. The PCL block can be crystallized into single crystals in dilute solution while the PEG block can be extruded on the lamellae surface under appropriate crystallization temperature. The loop size effect can be evaluated by varying the molecular weight of PEG segment. If PCL-*b*-PEO diblock copolymer is used, the effect of chain conformation (e.g. PEG with one free end vs. PEG loop with two end attached to the crystalline lamellae) can be compared.

List of References

1. Tarascon, J. M.; Armand, M., Issues and challenges facing rechargeable lithium batteries. *Nature* **2001,** *414* (6861), 359-367.

2. Winter, M.; Besenhard, J. O.; Spahr, M. E.; Novák, P., Insertion electrode materials for rechargeable lithium batteries. *Advanced Materials* **1998,** *10* (10), 725-763.

3. Armand, M.; Tarascon, J. M., Building better batteries. *Nature* **2008,** *451* (7179), 652-657.

4. Bruce, P. G.; Scrosati, B.; Tarascon, J. M., Nanomaterials for rechargeable lithium batteries. *Angew. Chem.-Int. Edit.* **2008,** *47* (16), 2930-2946.

5. Brandt, K., Historical development of secondary lithium batteries. *Solid State Ionics* **1994,** *69* (3–4), 173-183.

6. Koksbang, R.; Barker, J.; Shi, H.; Saïdi, M. Y., Cathode materials for lithium rocking chair batteries. *Solid State Ionics* **1996,** *84* (1–2), 1-21.

7. Armand, M., Polymer solid electrolytes - an overview. *Solid State Ionics* **1983,** *9–10, Part 2* (0), 745-754.

8. Armand, M. B., Polymer Electrolytes. *Annual Review of Materials Science* **1986,** *16* (1), 245-261.

9. Armand, M., Polymers with Ionic Conductivity. *Advanced Materials* **1990,** *2* (6-7), 278-286.

10. Hickner, M. A., Ion-containing polymers: new energy & clean water. *Mater. Today* **2010,** *13* (5), 34-41.

11. Di Noto, V.; Lavina, S.; Giffin, G. A.; Negro, E.; Scrosati, B., Polymer electrolytes: Present, past and future. *Electrochimica Acta* **2011,** *57* (0), 4-13.

12. Murata, K.; Izuchi, S.; Yoshihisa, Y., An overview of the research and development of solid polymer electrolyte batteries. *Electrochimica Acta* **2000,** *45* (8–9), 1501-1508.

13. Meyer, W. H., Polymer electrolytes for Lithium-Ion batteries. *Advanced Materials* **1998,** *10* (6), 439-448.

14. Takeoka, S.; Ohno, H.; Tsuchida, E., Recent advancement of ion-conductive polymers. *Polymers for Advanced Technologies* **1993,** *4* (2-3), 53-73.

15. Gray, F. M.; MacCallum, J. R.; Vincent, C. A., Poly(ethylene oxide) - $LiCF_3SO_3$ - polystyrene electrolyte systems. *Solid State Ionics* **1986,** *18–19, Part 1* (0), 282-286.

16. Morita, M.; Ishikawa, M.; Matsuda, Y., Ionic conductivities of polymeric solid electrolyte films containing rare earth ions. *Journal of Alloys and Compounds* **1997,** *250* (1–2), 524-527.

17. Stevens, J. R.; Such, K.; Cho, N.; Wieczorek, W., Polyether-PMMA adhesive electrolytes for electrochromic applications. *Solar Energy Materials and Solar Cells* **1995,** *39* (2–4), 223-237.

18. Such, K.; Stevens, J. R.; Wieczorek, W.; Siekierski, M.; Florjanczyk, Z., Polymer solid electrolytes from the PEG-PMMA-$LiCF_3SO_3$ system. *Journal of Polymer Science Part B: Polymer Physics* **1994,** *32* (13), 2221-2233.

19. Floriańczyk, Z.; Such, K.; Wieczorek, W.; Wasiucionek, M., Highly conductive poly (ethylene oxide)-poly (methyl methacrylate) blends complexed with alkali metal salts. *Polymer* **1991,** *32* (18), 3422-3425.

20. Wieczorek, W.; Such, K.; Florjanczyk, Z.; Przyluski, J., Application of acrylic polymers in blend-based polymeric electrolytes. *Electrochimica Acta* **1992,** *37* (9), 1565-1567.

21. Wieczorek, W.; Such, K.; Florjanczyk, Z.; Stevens, J. R., Polyether, polyacrylamide, $LiClO_4$ composite electrolytes with enhanced conductivity. *The Journal of Physical Chemistry* **1994,** *98* (27), 6840-6850.

22. Singh, M.; Odusanya, O.; Wilmes, G. M.; Eitouni, H. B.; Gomez, E. D.; Patel, A. J.; Chen, V. L.; Park, M. J.; Fragouli, P.; Iatrou, H.; Hadjichristidis, N.; Cookson, D.; Balsara, N. P., Effect of Molecular Weight on the Mechanical and Electrical Properties of Block Copolymer Electrolytes. *Macromolecules* **2007,** *40* (13), 4578-4585.

23. Panday, A.; Mullin, S.; Gomez, E. D.; Wanakule, N.; Chen, V. L.; Hexemer, A.; Pople, J.; Balsara, N. P., Effect of Molecular Weight and Salt Concentration on Conductivity of Block Copolymer Electrolytes. *Macromolecules* **2009,** *42* (13), 4632-4637.

24. Gomez, E. D.; Panday, A.; Feng, E. H.; Chen, V.; Stone, G. M.; Minor, A. M.; Kisielowski, C.; Downing, K. H.; Borodin, O.; Smith, G. D.; Balsara, N. P., Effect of Ion Distribution on Conductivity of Block Copolymer Electrolytes. *Nano Letters* **2009,** *9* (3), 1212-1216.

25. Wanakule, N. S.; Panday, A.; Mullin, S. A.; Gann, E.; Hexemer, A.; Balsara, N. P., Ionic conductivity of block copolymer electrolytes in the vicinity of order-disorder and order-order transitions. *Macromolecules* **2009,** *42* (15), 5642-5651.

26. Park, M. J.; Balsara, N. P., Anisotropic proton conduction in aligned block copolymer electrolyte membranes at equilibrium with humid air. *Macromolecules* **2010,** *43* (1), 292-298.

27. Javier, A. E.; Patel, S. N.; Hallinan Jr, D. T.; Srinivasan, V.; Balsara, N. P., Simultaneous electronic and ionic conduction in a block copolymer: Application in lithium battery electrodes. *Angewandte Chemie International Edition* **2011,** *50* (42), 9848-9851.

28. Mullin, S. A.; Stone, G. M.; Panday, A.; Balsara, N. P., Salt diffusion coefficients in block copolymer electrolytes. *Journal of The Electrochemical Society* **2011,** *158* (6), A619-A627.

29. Nakamura, I.; Balsara, N. P.; Wang, Z.-G., Thermodynamics of Ion-Containing Polymer Blends and Block Copolymers. *Physical Review Letters* **2011,** *107* (19), 198301.

30. Stone, G. M.; Mullin, S. A.; Teran, A. A.; Hallinan, D. T.; Minor, A. M.; Hexemer, A.; Balsara, N. P., Resolution of the modulus versus adhesion dilemma in solid polymer electrolytes for rechargeable lithium metal batteries. *Journal of The Electrochemical Society* **2012,** *159* (3), A222-A227.

31. Elabd, Y. A.; Walker, C. W.; Beyer, F. L., Triblock copolymer ionomer membranes Part II. Structure characterization and its effects on transport properties and direct methanol fuel cell performance. *Journal of Membrane Science* **2004,** *231* (1-2), 181-188.

32. Elabd, Y. A.; Napadensky, E.; Walker, C. W.; Winey, K. I., Transport properties of sulfonated poly (styrene-b-isobutylene-b-styrene) triblock copolymers at high ion-exchange capacities. *Macromolecules* **2006,** *39* (1), 399-407.

33. Ionescu-Vasii, L. L.; Garcia, B.; Armand, M., Conductivities of electrolytes based on PEI-b-PEO- b-PEI triblock copolymers with lithium and copper TFSI salts. *Solid State Ionics* **2006,** *177* (9), 885-892.

34. Simone, P. M.; Lodge, T. P., Phase behavior and ionic conductivity of concentrated solutions of polystyrene-poly (ethylene oxide) diblock copolymers in an ionic liquid. *ACS applied materials & interfaces* **2009,** *1* (12), 2812-2820.

35. Ji, J.; Li, B.; Zhong, W.-H., Effects of a block copolymer as multifunctional fillers on ionic conductivity, mechanical properties, and dimensional stability of solid polymer electrolytes. *The Journal of Physical Chemistry B* **2010,** *114* (43), 13637-13643.

36. Elabd, Y. A.; Hickner, M. A., Block copolymers for fuel cells. *Macromolecules* **2011,** *44* (1), 1-11.

37. Giles, J.; Gray, F.; MacCallum, J.; Vincent, C., Synthesis and characterization of ABA block copolymer-based polymer electrolytes. *Polymer* **1987,** *28* (11), 1977-1981.

38. Niitani, T.; Shimada, M.; Kawamura, K.; Kanamura, K., Characteristics of new-type solid polymer electrolyte controlling nano-structure. *Journal of Power Sources* **2005,** *146* (1–2), 386-390.

39. Ruzette, A.-V. G.; Soo, P. P.; Sadoway, D. R.; Mayes, A. M., Melt-Formable Block Copolymer Electrolytes for Lithium Rechargeable Batteries. *Journal of The Electrochemical Society* **2001,** *148* (6), A537-A543.

40. Gray, F. M.; MacCallum, J. R.; Vincent, C. A.; Giles, J. R. M., Novel polymer electrolytes based on ABA block copolymers. *Macromolecules* **1988,** *21* (2), 392-397.

41. Soo, P. P.; Huang, B.; Jang, Y.-I.; Chiang, Y.-M.; Sadoway, D. R.; Mayes, A. M., Rubbery block copolymer electrolytes for solid-State rechargeable lithium batteries. *Journal of The Electrochemical Society* **1999,** *146* (1), 32-37.

42. Teran, A. A.; Balsara, N. P., Effect of lithium polysulfides on the morphology of block copolymer electrolytes. *Macromolecules* **2011,** *44* (23), 9267-9275.

43. Gomez, E. D.; Ruegg, M. L.; Minor, A. M.; Kisielowski, C.; Downing, K. H.; Glaeser, R. M.; Balsara, N. P., Interfacial concentration profiles of rubbery polyolefin lamellae determined by quantitative electron microscopy. *Macromolecules* **2008,** *41* (1), 156-162.

44. Wanakule, N. S.; Panday, A.; Mullin, S. A.; Gann, E.; Hexemer, A.; Balsara, N. P., Ionic Conductivity of Block Copolymer Electrolytes in the Vicinity of Order−Disorder and Order−Order Transitions. *Macromolecules* **2009,** *42* (15), 5642-5651.

45. Wanakule, N. S.; Virgili, J. M.; Teran, A. A.; Wang, Z.-G.; Balsara, N. P., Thermodynamic properties of block copolymer electrolytes containing imidazolium and lithium salts. *Macromolecules* **2010,** *43* (19), 8282-8289.

46. Young, W. S.; Kuan, W. F.; Epps, T. H., Block copolymer electrolytes for rechargeable lithium batteries. *J. Polym. Sci. Pt. B-Polym. Phys.* **2014,** *52* (1), 1-16.

47. Quartarone, E.; Mustarelli, P., Electrolytes for solid-state lithium rechargeable batteries: recent advances and perspectives. *Chemical Society Reviews* **2011,** *40* (5), 2525-2540.

48. Croce, F.; Persi, L.; Ronci, F.; Scrosati, B., Nanocomposite polymer electrolytes and their impact on the lithium battery technology. *Solid State Ionics* **2000,** *135* (1), 47-52.

49. Croce, F.; Appetecchi, G. B.; Persi, L.; Scrosati, B., Nanocomposite polymer electrolytes for lithium batteries. *Nature* **1998,** *394* (6692), 456-458.

50. Croce, F.; Curini, R.; Martinelli, A.; Persi, L.; Ronci, F.; Scrosati, B.; Caminiti, R., Physical and chemical properties of nanocomposite polymer electrolytes. *The Journal of Physical Chemistry B* **1999,** *103* (48), 10632-10638.

51. Best, A. S.; Adebahr, J.; Jacobsson, P.; MacFarlane, D. R.; Forsyth, M., Microscopic interactions in nanocomposite electrolytes. *Macromolecules* **2001,** *34* (13), 4549-4555.

52. Marcinek, M.; Bac, A.; Lipka, P.; Zalewska, A.; Żukowska, G.; Borkowska, R.; Wieczorek, W., Effect of filler surface group on ionic interactions in PEG−$LiClO_4$−Al_2O_3 composite polyether electrolytes. *The Journal of Physical Chemistry B* **2000,** *104* (47), 11088-11093.

53. Jayathilaka, P. A. R. D.; Dissanayake, M. A. K. L.; Albinsson, I.; Mellander, B. E., Effect of nano-porous Al_2O_3 on thermal, dielectric and transport properties of the $(PEO)_9$LiTFSI polymer electrolyte system. *Electrochimica Acta* **2002,** *47* (20), 3257-3268.

54. Johansson, P.; Ratner, M. A.; Shriver, D. F., The influence of inert oxide fillers on poly(ethylene oxide) and amorphous poly(ethylene oxide) based polymer electrolytes. *The Journal of Physical Chemistry B* **2001,** *105* (37), 9016-9021.

55. Xie, J.; Duan, R. G.; Han, Y.; Kerr, J. B., Morphological, rheological and electrochemical studies of Poly(ethylene oxide) electrolytes containing fumed silica nanoparticles. *Solid State Ionics* **2004,** *175* (1–4), 755-758.

56. Zhou, D.; Mei, X.; Ouyang, J., Ionic conductivity enhancement of oolyethylene oxide-$LiClO_4$ electrolyte by adding functionalized multi-walled carbon nanotubes. *The Journal of Physical Chemistry C* **2011,** *115* (33), 16688-16694.

57. Loyens, W.; Maurer, F. H. J.; Jannasch, P., Melt-compounded salt-containing poly(ethylene oxide)/clay nanocomposites for polymer electrolyte membranes. *Polymer* **2005,** *46* (18), 7334-7345.

58. Choudhary, S.; Sengwa, R. J., Effect of different anions of lithium salt and MMT nanofiller on ion conduction in melt-compounded PEO–LiX–MMT electrolytes. *Ionics* **2012,** *18* (4), 379-384.

59. Gadjourova, Z.; Andreev, Y. G.; Tunstall, D. P.; Bruce, P. G., Ionic conductivity in crystalline polymer electrolytes. *Nature* **2001,** *412* (6846), 520-523.

60. Stoeva, Z.; Martin-Litas, I.; Staunton, E.; Andreev, Y. G.; Bruce, P. G., Ionic conductivity in the crystalline polymer electrolytes PEO_6: $LiXF_6$, X= P, As, Sb. *Journal of the American Chemical Society* **2003,** *125* (15), 4619-4626.

61. Christie, A. M.; Lilley, S. J.; Staunton, E.; Andreev, Y. G.; Bruce, P. G., Increasing the conductivity of crystalline polymer electrolytes. *Nature* **2005,** *433* (7021), 50-53.

62. Fullerton-Shirey, S. K.; Maranas, J. K., Effect of $LiClO_4$ on the structure and mobility of PEO-based solid polymer electrolytes. *Macromolecules* **2009,** *42* (6), 2142-2156.

63. Marzantowicz, M.; Dygas, J. R.; Krok, F.; Nowiński, J. L.; Tomaszewska, A.; Florjańczyk, Z.; Zygadło-Monikowska, E., Crystalline phases, morphology and conductivity of PEO:LiTFSI electrolytes in the eutectic region. *Journal of Power Sources* **2006,** *159* (1), 420-430.

64. Marzantowicz, M.; Dygas, J. R.; Krok, F.; Łasińska, A.; Florjańczyk, Z.; Zygadło-Monikowska, E.; Affek, A., Crystallization and melting of PEO:LiTFSI polymer electrolytes investigated simultaneously by impedance spectroscopy and polarizing microscopy. *Electrochimica Acta* **2005,** *50* (19), 3969-3977.

65. Dygas, J. R.; Misztal-Faraj, B.; Florjańczyk, Z.; Krok, F.; Marzantowicz, M.; Zygadło-Monikowska, E., Effects of inhomogeneity on ionic conductivity and relaxations in PEO and PEO–salt complexes. *Solid State Ionics* **2003,** *157* (1–4), 249-256.

66. Choi, B.-K., Optical microscopy study on the crystallization in PEO-salt polymer electrolytes. *Solid State Ionics* **2004,** *168* (1–2), 123-129.

67. Marzantowicz, M.; Dygas, J. R.; Krok, F.; Florjańczyk, Z.; Zygadło-Monikowska, E., Influence of crystalline complexes on electrical properties of PEO:LiTFSI electrolyte. *Electrochimica Acta* **2007,** *53* (4), 1518-1526.

68. Fenton, D. E.; Parker, J. M.; Wright, P. V., Complexes of alkali metal ions with poly(ethylene oxide). *Polymer* **1973,** *14* (11), 589-589.

69. Wright, P. V., Electrical conductivity in ionic complexes of poly(ethylene oxide). *British Polymer Journal* **1975,** *7* (5), 319-327.

70. Wright, P. V., An anomalous transition to a lower activation energy for dc electrical conduction above the glass-transition temperature. *Journal of Polymer Science: Polymer Physics Edition* **1976,** *14* (5), 955-957.

71. Armand, M. B., Chabagno, J. M., and Duclot, M. J. Fast Ion Transport in Solids, North Holland, New York, Vashisha, P.; Mundy, J. N.; Shenoy, G. K., Eds. North Holland, New York, 1979; pp 131–136.

72. Killis, A.; Le Nest, J.-F.; Cheradame, H., Mise en évidence expérimentale de l'importance de la température de transition vitreuse sur la conductivité ionique des réseaux macromoléculaires. *Die Makromolekulare Chemie, Rapid Communications* **1980,** *1* (9), 595-598.

73. Lee, C. C.; Wright, P. V., Morphology and ionic conductivity of complexes of sodium iodide and sodium thiocyanate with poly(ethylene oxide). *Polymer* **1982,** *23* (5), 681-689.

74. Payne, D. R.; Wright, P. V., Morphology and ionic conductivity of some lithium ion complexes with poly(ethylene oxide). *Polymer* **1982,** *23* (5), 690-693.

75. Berthier, C.; Gorecki, W.; Minier, M.; Armand, M. B.; Chabagno, J. M.; Rigaud, P., Microscopic investigation of ionic conductivity in alkali metal salts-poly(ethylene oxide) adducts. *Solid State Ionics* **1983,** *11* (1), 91-95.

76. Ratner, M. A.; Shriver, D. F., Ion transport in solvent-free polymers. *Chemical Reviews* **1988,** *88* (1), 109-124.

77. Quartarone, E.; Mustarelli, P.; Magistris, A., PEO-based composite polymer electrolytes. *Solid State Ionics* **1998,** *110* (1–2), 1-14.

78. Chatani, Y.; Okamura, S., Crystal structure of poly(ethylene oxide)—sodium iodide complex. *Polymer* **1987,** *28* (11), 1815-1820.

79. Angell, C. A., Fast ion motion in glassy and amorphous materials. *Solid State Ionics* **1983,** *9–10, Part 1* (0), 3-16.

80. MacCallum, J. R.; Tomlin, A. S.; Vincent, C. A., An investigation of the conducting species in polymer electrolytes. *European Polymer Journal* **1986,** *22* (10), 787-791.

81. Torell, L. M.; Angell, C. A., Ion-matrix coupling in polymer electrolytes from relaxation time studies. *British Polymer Journal* **1988,** *20* (3), 173-179.

82. Bruce, P. G.; Vincent, C. A., Effect of ion association on transport in polymer electrolytes. *Faraday Discussions of the Chemical Society* **1989,** *88* (0), 43-54.

83. Cameron, G. G.; Ingram, M. D.; Harvie, J. L., Ion transport in polymer electrolytes. *Faraday Discussions of the Chemical Society* **1989,** *88* (0), 55-63.

84. Ratner, M. A.; Nitzan, A., Conductivity in polymer ionics. Dynamic disorder and correlation. *Faraday Discussions of the Chemical Society* **1989,** *88* (0), 19-42.

85. Xie, L.; Farrington, G. C., Application of molecular modeling to the study of polymer electrolytes. *Solid State Ionics* **1993,** *60* (1–3), 19-28.

86. Angell, C. A.; Liu, C.; Sanchez, E., Rubbery solid electrolytes with dominant cationic transport and high ambient conductivity. *Nature* **1993,** *362* (6416), 137-139.

87. Chung, S.; Wang, Y.; Persi, L.; Croce, F.; Greenbaum, S.; Scrosati, B.; Plichta, E., Enhancement of ion transport in polymer electrolytes by addition of nanoscale inorganic oxides. *Journal of Power Sources* **2001,** *97*, 644-648.

88. Agapov, A. L.; Sokolov, A. P., Decoupling ionic conductivity from structural relaxation: A way to solid polymer electrolytes? *Macromolecules* **2011,** *44* (11), 4410-4414.

89. Wang, Y.; Agapov, A. L.; Fan, F.; Hong, K.; Yu, X.; Mays, J.; Sokolov, A. P., Decoupling of ionic transport from segmental relaxation in polymer electrolytes. *Physical Review Letters* **2012,** *108* (8), 088303.

90. Sinha, K.; Maranas, J. K., Segmental dynamics and ion association in PEO-based single ion conductors. *Macromolecules* **2011,** *44* (13), 5381-5391.

91. Sinha, K.; Wang, W.; Winey, K. I.; Maranas, J. K., Dynamic patterning in PEO-based single ion conductors for Li ion batteries. *Macromolecules* **2012,** *45* (10), 4354-4362.

92. Tudryn, G. J.; Liu, W.; Wang, S.-W.; Colby, R. H., Counterion dynamics in polyester−sulfonate ionomers with ionic liquid counterions. *Macromolecules* **2011,** *44* (9), 3572-3582.

93. Lin, K.-J.; Li, K.; Maranas, J. K., Differences between polymer/salt and single ion conductor solid polymer electrolytes. *RSC Advances* **2013,** *3* (5), 1564-1571.

94. Dou, S.; Zhang, S.; Klein, R. J.; Runt, J.; Colby, R. H., Synthesis and characterization of poly(ethylene glycol)-based single-ion conductors. *Chemistry of Materials* **2006,** *18* (18), 4288-4295.

95. Wang, W.; Tudryn, G. J.; Colby, R. H.; Winey, K. I., Thermally driven ionic aggregation in poly(ethylene oxide)-based sulfonate ionomers. *Journal of the American Chemical Society* **2011,** *133* (28), 10826-10831.

96. Fragiadakis, D.; Dou, S.; Colby, R. H.; Runt, J., Molecular mobility and Li+ conduction in polyester copolymer ionomers based on poly(ethylene oxide). *The Journal of Chemical Physics* **2009,** *130* (6), -.

97. Lin, K.-J.; Maranas, J. K., Cation coordination and motion in a poly(ethylene oxide)-based single ion conductor. *Macromolecules* **2012,** *45* (15), 6230-6240.

98. Vögtle, F.; Weber, E., Crown ethers and analogs. Patai, S.; Rappoport, Z., Eds. Wiley: New York, 1989, Ch. 4.

99. Pedersen, C. J., The discovery of crown ethers (Noble Lecture). *Angewandte Chemie International Edition in English* **1988,** *27* (8), 1021-1027.

100. Baril, D.; Michot, C.; Armand, M., Electrochemistry of liquids vs. solids: Polymer electrolytes. *Solid State Ionics* **1997,** *94* (1–4), 35-47.

101. Xu, K., Nonaqueous liquid electrolytes for lithium-based rechargeable batteries. *Chemical Reviews* **2004,** *104* (10), 4303-4418.

102. Ue, M., Mobility and ionic association of lithium and quaternary ammonium salts in propylene carbonate and γ-butyrolactone. *Journal of The Electrochemical Society* **1994,** *141* (12), 3336-3342.

103. Park, M.; Zhang, X.; Chung, M.; Less, G. B.; Sastry, A. M., A review of conduction phenomena in Li-ion batteries. *Journal of Power Sources* **2010,** *195* (24), 7904-7929.

104. Vogel, H., The law of the relation between the viscosity of liquids and the temperature. *Physikalische Zeitschrift* **1921,** *22*, 645.

105. Fulcher, G. S., Analysis of recent measurements of the viscosity of glasses *Journal of the American Ceramic Society* **1925,** *8* (6), 339-355.

106. Tammann, G.; Hesse, W., Die Abhängigkeit der Viscosität von der Temperatur bie unterkühlten Flüssigkeiten. *Zeitschrift für anorganische und allgemeine Chemie* **1926,** *156* (1), 245-257.

107. Cohen, M. H.; Turnbull, D., Molecular transport in liquids and glasses. *The Journal of Chemical Physics* **1959,** *31* (5), 1164-1169.

108. Chow, T. S., Molecular interpretation of the glass transition temperature of polymer-diluent systems. *Macromolecules* **1980,** *13* (2), 362-364.

109. Williams, M.; Landel, R.; Ferry, J., The temperature dependence of relaxation mechanisms in amorphous polymers and other glass-forming liquids. *Journal of the American Chemical Society* **1955,** *77* (14), 3701-3707.

110. Armand, M., The history of polymer electrolytes. *Solid State Ionics* **1994,** *69* (3–4), 309-319.

111. Robitaille, C. D.; Fauteux, D., Phase diagrams and conductivity characterization of some PEO-LiX electrolytes. *Journal of The Electrochemical Society* **1986,** *133* (2), 315-325.

112. Neat, R.; Glasse, M.; Linford, R.; Hooper, A., Thermal history and polymer electrolyte structure: Implications for solid-state battery design. *Solid State Ionics* **1986,** *18–19, Part 2* (0), 1088-1092.

113. Marzantowicz, M.; Krok, F.; Dygas, J. R.; Florjańczyk, Z.; Zygadło-Monikowska, E., The influence of phase segregation on properties of semicrystalline PEO:LiTFSI electrolytes. *Solid State Ionics* **2008,** *179* (27–32), 1670-1678.

114. Lascaud, S.; Perrier, M.; Vallee, A.; Besner, S.; Prud'homme, J.; Armand, M., Phase diagrams and conductivity behavior of poly(ethylene oxide)-molten salt rubbery electrolytes. *Macromolecules* **1994,** *27* (25), 7469-7477.

115. Marzantowicz, M.; Dygas, J. R.; Krok, F.; Łasińska, A.; Florjańczyk, Z.; Zygadło-Monikowska, E., In situ microscope and impedance study of polymer electrolytes. *Electrochimica Acta* **2006,** *51* (8–9), 1713-1727.

116. Zhang, Y.; Li, J.; Huo, H.; Jiang, S., Effects of lithium perchlorate on poly(ethylene oxide) spherulite morphology and spherulite growth kinetics. *Journal of Applied Polymer Science* **2012,** *123* (4), 1935-1943.

117. Minier, M.; Berthier, C.; Gorecki, W., Thermal analysis and NMR study of a poly(ethylene oxide) complex electrolyte - PEO($LiCF_3SO_3$)$_x$. *Journal De Physique* **1984,** *45* (4), 739-744.

118. MacGlashan, G. S.; Andreev, Y. G.; Bruce, P. G., Structure of the polymer electrolyte poly(ethylene oxide)$_6$:$LiAsF_6$. *Nature* **1999,** *398* (6730), 792-794.

119. Stoeva, Z.; Martin-Litas, I.; Staunton, E.; Andreev, Y. G.; Bruce, P. G., Ionic Conductivity in the Crystalline Polymer Electrolytes PEO6:LiXF6, X = P, As, Sb. *Journal of the American Chemical Society* **2003,** *125* (15), 4619-4626.

120. Gadjourova, Z.; Martín y Marero, D.; Andersen, K. H.; Andreev, Y. G.; Bruce, P. G., Structures of the polymer electrolyte complexes PEO_6: $LiXF_6$ (X= P, Sb), determined from neutron powder diffraction data. *Chemistry of Materials* **2001,** *13* (4), 1282-1285.

121. MacGlashan, G. S.; Andreev, Y. G.; Bruce, P. G., Structure of the polymer electrolyte poly (ethylene oxide) 6: LiAsF6. *Nature* **1999,** *398* (6730), 792-794.

122. Staunton, E.; Andreev, Y. G.; Bruce, P. G., Factors influencing the conductivity of crystalline polymer electrolytes. *Faraday Discussions* **2007,** *134* (0), 143-156.

123. Fox, T. G.; Flory, P. J., The glass temperature and related properties of polystyrene. Influence of molecular weight. *Journal of Polymer Science* **1954,** *14* (75), 315-319.

124. Shi, J.; Vincent, C. A., The effect of molecular weight on cation mobility in polymer electrolytes. *Solid State Ionics* **1993,** *60* (1–3), 11-17.

125. Devaux, D.; Bouchet, R.; Glé, D.; Denoyel, R., Mechanism of ion transport in PEO/LiTFSI complexes: Effect of temperature, molecular weight and end groups. *Solid State Ionics* **2012,** *227* (0), 119-127.

126. Monroe, C.; Newman, J., The impact of elastic deformation on deposition kinetics at lithium/polymer interfaces. *Journal of The Electrochemical Society* **2005,** *152* (2), A396-A404.

127. Wang, C.; Sakai, T.; Watanabe, O.; Hirahara, K.; Nakanishi, T., All solid-state lithium-polymer battery using a self-cross-linking polymer electrolyte. *Journal of The Electrochemical Society* **2003,** *150* (9), A1166-A1170.

128. Majewski, P. W.; Gopinadhan, M.; Jang, W.-S.; Lutkenhaus, J. L.; Osuji, C. O., Anisotropic ionic conductivity in block copolymer membranes by magnetic field alignment. *Journal of the American Chemical Society* **2010,** *132* (49), 17516-17522.

129. Kishimoto, K.; Yoshio, M.; Mukai, T.; Yoshizawa, M.; Ohno, H.; Kato, T., Nanostructured anisotropic ion-conductive films. *Journal of the American Chemical Society* **2003,** *125* (11), 3196-3197.

130. Walls, H. J.; Zhou, J.; Yerian, J. A.; Fedkiw, P. S.; Khan, S. A.; Stowe, M. K.; Baker, G. L., Fumed silica-based composite polymer electrolytes: synthesis, rheology, and electrochemistry. *Journal of Power Sources* **2000,** *89* (2), 156-162.

131. Golodnitsky, D.; Livshits, E.; Ulus, A.; Barkay, Z.; Lapides, I.; Peled, E.; Chung, S. H.; Greenbaum, S., Fast ion transport phenomena in oriented semicrystalline LiI−P(EO)n-based polymer electrolytes. *The Journal of Physical Chemistry A* **2001,** *105* (44), 10098-10106.

132. Smith, D. M.; Dong, B.; Marron, R. W.; Birnkrant, M. J.; Elabd, Y. A.; Natarajan, L. V.; Tondiglia, V. P.; Bunning, T. J.; Li, C. Y., Tuning ion conducting pathways using holographic polymerization. *Nano Letters* **2011,** *12* (1), 310-314.

133. Bannister, D. J.; Davies, G. R.; Ward, I. M.; McIntyre, J. E., Ionic conductivities for poly(ethylene oxide) complexes with lithium salts of monobasic and dibasic acids and blends of poly(ethylene oxide) with lithium salts of anionic polymers. *Polymer* **1984,** *25* (9), 1291-1296.

134. Kobayashi, N.; Uchiyama, M.; Tsuchida, E., Poly[lithium methacrylate-co-oligo(oxyethylene)methacrylate] as a solid electrolyte with high ionic conductivity. *Solid State Ionics* **1985,** *17* (4), 307-311.

135. Bouchet, R.; Maria, S.; Meziane, R.; Aboulaich, A.; Lienafa, L.; Bonnet, J.-P.; Phan, T. N. T.; Bertin, D.; Gigmes, D.; Devaux, D.; Denoyel, R.; Armand, M., Single-ion BAB triblock copolymers as highly efficient electrolytes for lithium-metal batteries. *Nat Mater* **2013,** *12* (5), 452-457.

136. Bates, F. S.; Fredrickson, G. H., Block copolymers—Designer soft materials. *Print edition* **1999,** *52* (2), 32-38.

137. Meuler, A. J.; Hillmyer, M. A.; Bates, F. S., Ordered network mesostructures in block polymer materials. *Macromolecules* **2009,** *42* (19), 7221-7250.

138. Epps, T. H.; Bailey, T. S.; Pham, H. D.; Bates, F. S., Phase behavior of lithium perchlorate-doped poly(styrene-b-isoprene-b-ethylene oxide) triblock copolymers. *Chemistry of Materials* **2002,** *14* (4), 1706-1714.

139. Cho, B.-K.; Jain, A.; Gruner, S. M.; Wiesner, U., Mesophase structure-mechanical and ionic transport correlations in extended amphiphilic dendrons. *Science* **2004,** *305* (5690), 1598-1601.

140. Young, W.-S.; Brigandi, P. J.; Epps, T. H., Crystallization-induced lamellar-to-lamellar thermal transition in salt-containing block copolymer electrolytes. *Macromolecules* **2008,** *41* (17), 6276-6279.

141. Epps, T. H.; Bailey, T. S.; Waletzko, R.; Bates, F. S., Phase behavior and block sequence effects in lithium perchlorate-doped poly(isoprene-b-styrene-b-ethylene oxide) and poly(styrene-b-isoprene-b-ethylene oxide) triblock copolymers. *Macromolecules* **2003,** *36* (8), 2873-2881.

142. Niitani, T.; Shimada, M.; Kawamura, K.; Dokko, K.; Rho, Y.-H.; Kanamura, K., Synthesis of Li□+□ Ion conductive PEO-PSt block copolymer electrolyte with microphase separation structure. *Electrochemical and Solid-State Letters* **2005,** *8* (8), A385-A388.

143. Kim, S. H.; Misner, M. J.; Yang, L.; Gang, O.; Ocko, B. M.; Russell, T. P., Salt complexation in block copolymer thin films. *Macromolecules* **2006,** *39* (24), 8473-8479.

144. Young, W.-S.; Epps, T. H., Salt doping in PEO-containing block copolymers: Counterion and concentration effects. *Macromolecules* **2009,** *42* (7), 2672-2678.

145. Patel, S. N.; Javier, A. E.; Beers, K. M.; Pople, J. A.; Ho, V.; Segalman, R. A.; Balsara, N. P., Morphology and thermodynamic properties of a copolymer with an electronically conducting block: poly(3-ethylhexylthiophene)-block-poly(ethylene oxide). *Nano Letters* **2012,** *12* (9), 4901-4906.

146. Nakamura, I.; Wang, Z.-G., Salt-doped block copolymers: ion distribution, domain spacing and effective [small chi] parameter. *Soft Matter* **2012,** *8* (36), 9356-9367.

147. Gunkel, I.; Thurn-Albrecht, T., Thermodynamic and structural changes in ion-containing symmetric diblock copolymers: A small-angle X-ray scattering study. *Macromolecules* **2011,** *45* (1), 283-291.

148. Yuan, R.; Teran, A. A.; Gurevitch, I.; Mullin, S. A.; Wanakule, N. S.; Balsara, N. P., Ionic conductivity of low molecular weight block copolymer electrolytes. *Macromolecules* **2013,** *46* (3), 914-921.

149. Hallinan, D. T.; Mullin, S. A.; Stone, G. M.; Balsara, N. P., Lithium metal stability in batteries with block copolymer electrolytes. *Journal of The Electrochemical Society* **2013,** *160* (3), A464-A470.

150. Capuano, F.; Croce, F.; Scrosati, B., Composite polymer electrolytes. *Journal of The Electrochemical Society* **1991,** *138* (7), 1918-1922.

151. Krawiec, W.; Scanlon Jr, L. G.; Fellner, J. P.; Vaia, R. A.; Vasudevan, S.; Giannelis, E. P., Polymer nanocomposites: a new strategy for synthesizing solid electrolytes for rechargeable lithium batteries. *Journal of Power Sources* **1995,** *54* (2), 310-315.

152. Wieczorek, W.; Lipka, P.; Żukowska, G.; Wyciślik, H., Ionic interactions in polymeric electrolytes based on low molecular weight poly(ethylene glycol)s. *The Journal of Physical Chemistry B* **1998,** *102* (36), 6968-6974.

153. Capiglia, C.; Mustarelli, P.; Quartarone, E.; Tomasi, C.; Magistris, A., Effects of nanoscale SiO_2 on the thermal and transport properties of solvent-free, poly(ethylene oxide) (PEO)-based polymer electrolytes. *Solid State Ionics* **1999,** *118* (1–2), 73-79.

154. Kumar, B.; Scanlon, L. G., Polymer–ceramic composite electrolytes: conductivity and thermal history effects. *Solid State Ionics* **1999,** *124* (3–4), 239-254.

155. Appetecchi, G. B.; Croce, F.; Persi, L.; Ronci, F.; Scrosati, B., Transport and interfacial properties of composite polymer electrolytes. *Electrochimica Acta* **2000,** *45* (8–9), 1481-1490.

156. Scrosati, B.; Croce, F.; Persi, L., Impedance spectroscopy study of PEO - based nanocomposite polymer electrolytes. *Journal of The Electrochemical Society* **2000,** *147* (5), 1718-1721.

157. Croce, F.; Persi, L.; Scrosati, B.; Serraino-Fiory, F.; Plichta, E.; Hendrickson, M. A., Role of the ceramic fillers in enhancing the transport properties of composite polymer electrolytes. *Electrochimica Acta* **2001,** *46* (16), 2457-2461.

158. Wieczorek, W.; Florjanczyk, Z.; Stevens, J. R., Composite polyether based solid electrolytes. *Electrochimica Acta* **1995,** *40* (13–14), 2251-2258.

159. Siekierski, M.; Wieczorek, W.; Przyłuski, J., AC conductivity studies of composite polymeric electrolytes. *Electrochimica Acta* **1998,** *43* (10–11), 1339-1342.

160. Kim, Y. W.; Lee, W.; Choi, B. K., Relation between glass transition and melting of PEO–salt complexes. *Electrochimica Acta* **2000,** *45* (8–9), 1473-1477.

161. Choi, B.-K.; Kim, Y.-W.; Shin, K.-H., Effects of ceramic fillers on the electrical properties of $(PEO)_{16}LiClO_4$ electrolytes. *Journal of Power Sources* **1997,** *68* (2), 357-360.

162. Best, A. S.; Ferry, A.; MacFarlane, D. R.; Forsyth, M., Conductivity in amorphous polyether nanocomposite materials. *Solid State Ionics* **1999,** *126* (3–4), 269-276.

163. Sax, J.; Ottino, J. M., Modeling of transport of small molecules in polymer blends-application of effective medium theory *Polym. Eng. Sci.* **1983,** *23* (3), 165-176.

164. Park, M. J.; Balsara, N. P., Anisotropic proton conduction in aligned block copolymer electrolyte membranes at equilibrium with humid air. *Macromolecules* **2009,** *43* (1), 292-298.

165. Ohtake, T.; Ogasawara, M.; Ito-Akita, K.; Nishina, N.; Ujiie, S.; Ohno, H.; Kato, T., Liquid-crystalline complexes of mesogenic dimers containing oxyethylene moieties with $LiCF_3SO_3$: self-organized ion conductive materials. *Chemistry of Materials* **2000,** *12* (3), 782-789.

166. Li, J.; Kamata, K.; Komura, M.; Yamada, T.; Yoshida, H.; Iyoda, T., Anisotropic ion conductivity in liquid crystalline diblock copolymer membranes with perpendicularly oriented PEO cylindrical domains. *Macromolecules* **2007,** *40* (23), 8125-8128.

167. Zhou, Y.; Ahn, S.-k.; Lakhman, R. K.; Gopinadhan, M.; Osuji, C. O.; Kasi, R. M., Tailoring crystallization behavior of PEO-based liquid crystalline block copolymers through variation in liquid crystalline content. *Macromolecules* **2011,** *44* (10), 3924-3934.

168. Gopinadhan, M.; Majewski, P. W.; Osuji, C. O., Facile alignment of amorphous poly(ethylene oxide) microdomains in a liquid crystalline block copolymer using magnetic fields: Toward ordered electrolyte membranes. *Macromolecules* **2010,** *43* (7), 3286-3293.

169. Majewski, P. W.; Gopinadhan, M.; Osuji, C. O., Understanding anisotropic transport in self-assembled membranes and maximizing ionic conductivity by microstructure alignment. *Soft Matter* **2013,** *9* (29), 7106-7116.

170. Gopinadhan, M.; Majewski, P. W.; Choo, Y.; Osuji, C. O., Order-disorder transition and alignment dynamics of a block copolymer under high magnetic fields by in situ X-Ray scattering. *Physical Review Letters* **2013,** *110* (7), 078301.

171. Gopinadhan, M.; Majewski, P. W.; Beach, E. S.; Osuji, C. O., Magnetic field alignment of a diblock copolymer using a supramolecular route. *ACS Macro Letters* **2011,** *1* (1), 184-189.

172. Hu, H.; Gopinadhan, M.; Osuji, C. O., Directed self-assembly of block copolymers: a tutorial review of strategies for enabling nanotechnology with soft matter. *Soft Matter* **2014,** *10* (22), 3867-3889.

173. Smith, D. M.; Li, C. Y.; Bunning, T. J., Light-directed mesoscale phase separation via holographic polymerization. *Journal of Polymer Science Part B: Polymer Physics* **2014,** *52* (3), 232-250.

174. Golodnitsky, D.; Livshits, E.; Rosenberg, Y.; Peled, E.; Chung, S. H.; Wang, Y.; Bajue, S.; Greenbaum, S. G., A new approach to the understanding of ion transport in semicrystalline polymer electrolytes. *Journal of Electroanalytical Chemistry* **2000,** *491* (1–2), 203-210.

175. Golodnitsky, D.; Livshits, E.; Rosenberg, Y.; Lapides, I.; Peled, E., Stretching-induced changes in ion–polymer interactions in semicrystalline LiI–P(EO)n polymer electrolytes. *Solid State Ionics* **2002,** *147* (3–4), 265-273.

176. Golodnitsky, D.; Livshits, E.; Peled, E., Highly conductive oriented PEO-based polymer electrolytes. *Macromolecular Symposia* **2003,** *203* (1), 27-46.

177. Golodnitsky, D.; Livshits, E.; Kovarsky, R.; Peled, E.; Chung, S. H.; Suarez, S.; Greenbaum, S. G., New generation of ordered polymer electrolytes for lithium batteries. *Electrochemical and Solid-State Letters* **2004,** *7* (11), A412-A415.

178. Burba, C. M.; Frech, R.; Grady, B., Stretched PEO–$LiCF_3SO_3$ films: Polarized IR spectroscopy and X-ray diffraction. *Electrochimica Acta* **2007,** *53* (4), 1548-1555.

179. Gitelman, L.; Israeli, M.; Averbuch, A.; Nathan, M.; Schuss, Z.; Golodnitsky, D., Polymer geometry and Li+ conduction in poly(ethylene oxide). *Journal of Computational Physics* **2008,** *227* (18), 8437-8447.

180. Burba, C. M.; Woods, L.; Millar, S. Y.; Pallie, J., Polymer chain organization in tensile-stretched poly(ethylene oxide)-based polymer electrolytes. *Electrochimica Acta* **2011,** *57* (0), 165-171.

181. Golodnitsky, D.; Peled, E., Stretching-induced conductivity enhancement of LiI □ (PEO)-polymer electrolyte. *Electrochimica Acta* **2000,** *45* (8–9), 1431-1436.

182. Vallée, A.; Besner, S.; Prud'Homme, J., Comparative study of poly(ethylene oxide) electrolytes made with $LiN(CF_3SO_2)_2$, $LiCF_3SO_3$ and $LiClO_4$: Thermal properties and conductivity behaviour. *Electrochimica Acta* **1992,** *37* (9), 1579-1583.

183. Hardy, L. C.; Shriver, D. F., Preparation and electrical response of solid polymer electrolytes with only one mobile species. *Journal of the American Chemical Society* **1985,** *107* (13), 3823-3828.

184. Doyle, R. P.; Chen, X.; Macrae, M.; Srungavarapu, A.; Smith, L. J.; Gopinadhan, M.; Osuji, C. O.; Granados-Focil, S., Poly(ethylenimine)-based polymer blends as single-ion lithium conductors. *Macromolecules* **2014,** *47* (10), 3401-3408.

185. Tsuchida, E.; Ohno, H.; Kobayashi, N., Single-ion conduction in poly[(oligo(oxyethylene)methacrylate)-co-(alkali-metal methacrylates)]. *Macromolecules* **1988,** *21* (1), 96-100.

186. Ganapathiappan, S.; Chen, K.; Shriver, D. F., A new class of cation conductors: polyphosphazene sulfonates. *Macromolecules* **1988,** *21* (7), 2299-2301.

187. Zhou, G. B.; Khan, I. M.; Smid, J., Cation transport polymer electrolytes - siloxane comb polymers with pendant oligo-oxyethylene chains and sulfonate groups *Polymer Communications* **1989,** *30* (2), 52-55.

188. Rawsky, G. C.; Fujinami, T.; Shriver, D. F., Aluminosilicate/poly(ethylene glycol) copolymers: A new class of polyelectrolytes. *Chemistry of Materials* **1994,** *6* (12), 2208-2209.

189. Fujinami, T.; Tokimune, A.; Mehta, M. A.; Shriver, D. F.; Rawsky, G. C., Siloxyaluminate polymers with high Li+ ion conductivity. *Chemistry of Materials* **1997,** *9* (10), 2236-2239.

190. Watanabe, M.; Nagano, S.; Sanui, K.; Ogata, N., Estimation of Li+ transport number in polymer electrolytes by the combination of complex impedance and potentiostatic polarization measurements. *Solid State Ionics* **1988,** *28–30, Part 2* (0), 911-917.

191. Benrabah, D.; Sylla, S.; Alloin, F.; Sanchez, J. Y.; Armand, M., Perfluorosulfonate-polyether based single ion conductors. *Electrochimica Acta* **1995,** *40* (13–14), 2259-2264.

192. Sun, X.-G.; Reeder, C. L.; Kerr, J. B., Synthesis and characterization of network type single ion conductors. *Macromolecules* **2004,** *37* (6), 2219-2227.

193. Tsuchida, E.; Ohno, H.; Kobayashi, N.; Ishizaka, H., Poly[(ι-carboxy)oligo(oxyethylene) methacrylate] as a new type of polymeric solid electrolyte for alkali-metal ion transport. *Macromolecules* **1989,** *22* (4), 1771-1775.

194. Takeoka, S.; Maeda, Y.; Tsuchida, E.; Ohno, H., Synthesis, polymerization and cation conductive properties of (ω-carboxy)-oligo(oxyethylene) methacrylate. *Polymers for Advanced Technologies* **1990,** *1* (3-4), 201-205.

195. Feng, S.; Shi, D.; Liu, F.; Zheng, L.; Nie, J.; Feng, W.; Huang, X.; Armand, M.; Zhou, Z., Single lithium-ion conducting polymer electrolytes based on poly[(4-styrenesulfonyl)(trifluoromethanesulfonyl)imide] anions. *Electrochimica Acta* **2013,** *93* (0), 254-263.

196. Hummers, W. S.; Offerman, R. E., Preparation of graphite oxide. *Journal of the American Chemical Society* **1958,** *80*, 1339.

197. Steurer, P.; Wissert, R.; Thomann, R.; Mulhaupt, R., Functionalized graphenes and thermoplastic nanocomposites based upon expanded graphite oxide. *Macromol. Rapid Commun.* **2009,** *30* (4-5), 316-327.

198. Blundell, D.; Keller, A.; Kovacs, A., A new self-nucleation phenomenon and its application to the growing of polymer crystals from solution. *J. Polym. Sci. B: Polym. Lett.* **1966,** *4*, 481-486.

199. Li, B.; Li, C. Y., Immobilizing Au nanoparticles with polymer single crystals, patterning and asymmetric functionalization. *Journal of the American Chemical Society* **2007,** *129* (1), 12-13.

200. Wang, B. B.; Li, B.; Zhao, B.; Li, C. Y., Amphiphilic Janus gold nanoparticles via combining "Solid-State Grafting-to" and "Grafting-from" methods. *Journal of the American Chemical Society* **2008,** *130* (35), 11594-11595.

201. Li, C. Y., Polymer single crystal meets nanoparticles. *J. Poly. Sci. Poly. Phys.* **2009,** *47*, 2436-2440.

202. Geil, P., *Polymer single crystal*. Interscience New York, 1963.

203. Li, B.; Ni, C.; Li, C. Y., Poly(ethylene oxide) single crystals as templates for Au nanoparticle patterning and asymmetrical functionalization. *Macromolecules* **2008,** *41* (1), 149-155.

204. Li, B.; Wang, B. B.; Ferrier, R. C. M.; Li, C. Y., Programmable nanoparticle assembly via polymer single crystals. *Macromolecules* **2009,** *42* (24), 9394-9399.

205. Dillon, D. R.; Tenneti, K. K.; Li, C. Y.; Ko, F. K.; Sics, I.; Hsiao, B. S., On the structure and morphology of polyvinylidene fluoride-nanoclay nanocomposites. *Polymer* **2006,** *47* (5), 1678-1688.

206. Li, C. Y.; Tenneti, K. K.; Zhang, D.; Zhang, H.; Wan, X.; Chen, E.; Zhou, Q.; Avila-Orta, C.; Sics, I.; Hsiao, B., Hierarchical assembly of a series of rod-coil block copolymers: supramolecular LC phase in nanoenvironment *Macromolecules* **2004,** *37*, 2854-2860.

207. Tenneti, K. K.; Chen, X. F.; Li, C. Y.; Tu, Y. F.; Wan, X. H.; Zhou, Q. F.; Sics, I.; Hsiao, B. S., Perforated layer structures in liquid crystalline rod-coil block copolymers. *Journal of the American Chemical Society* **2005,** *127* (44), 15481-15490.

208. Tenneti, K. K.; Chen, X. F.; Li, C. Y.; Wan, X. H.; Fan, X. H.; Zhou, Q. F.; Rong, L. X.; Hsiao, B. S., Competition between liquid crystallinity and block copolymer self-assembly in core-shell rod-coil block copolymers. *Soft Matter* **2008,** *4* (3), 458-461.

209. Menczel, J. D. P., R. Bruce, *Thermal analysis of polymers: fundamentals and applications*. Wiley: New Jersey, 2009; p 60.

210. Spiro, M., *Techniques of Chemistry*. Wiley: New York, 1970; Vol. I, Part IIA.

211. Evans, J.; Vincent, C. A.; Bruce, P. G., Electrochemical measurement of transference numbers in polymer electrolytes. *Polymer* **1987,** *28* (13), 2324-2328.

212. Bruce, P. G.; Vincent, C. A., Steady state current flow in solid binary electrolyte cells. *Journal of Electroanalytical Chemistry and Interfacial Electrochemistry* **1987,** *225* (1–2), 1-17.

213. Bruce, P. G.; Evans, J.; Vincent, C. A., Conductivity and transference number measurements on polymer electrolytes. *Solid State Ionics* **1988,** *28*, 918-922.

214. Kim, Y.-T.; Smotkin, E. S., The effect of plasticizers on transport and electrochemical properties of PEO-based electrolytes for lithium rechargeable batteries. *Solid State Ionics* **2002,** *149* (1–2), 29-37.

215. Abraham, K. M.; Jiang, Z.; Carroll, B., Highly conductive PEO-like polymer electrolytes. *Chemistry of Materials* **1997,** *9* (9), 1978-1988.

216. Marzantowicz, M.; Dygas, J.; Jenninger, W.; Alig, I., Equivalent circuit analysis of impedance spectra of semicrystalline polymer. *Solid State Ionics* **2005,** *176* (25), 2115-2121.

217. Zhou, X.; Yin, Y.; Wang, Z.; Zhou, J.; Huang, H.; Mansour, A. N.; Zaykoski, J. A.; Fedderly, J. J.; Balizer, E., Effect of hot pressing on the ionic conductivity of the PEO/$LiCF_3SO_3$ based electrolyte membranes. *Solid State Ionics* **2011,** *196* (1), 18-24.

218. Chen, H.; Choi, J.-H.; Salas-de la Cruz, D.; Winey, K. I.; Elabd, Y. A., Polymerized ionic liquids: The effect of random copolymer composition on ion conduction. *Macromolecules* **2009,** *42* (13), 4809-4816.

219. Weber, R. L.; Ye, Y.; Schmitt, A. L.; Banik, S. M.; Elabd, Y. A.; Mahanthappa, M. K., Effect of nanoscale morphology on the conductivity of polymerized ionic liquid block copolymers. *Macromolecules* **2011,** *44* (14), 5727-5735.

220. Ye, Y.; Elabd, Y. A., Anion exchanged polymerized ionic liquids: High free volume single ion conductors. *Polymer* **2011,** *52* (5), 1309-1317.

221. Ye, Y.; Choi, J.-H.; Winey, K. I.; Elabd, Y. A., Polymerized ionic liquid block and random copolymers: Effect of weak microphase separation on ion transport. *Macromolecules* **2012,** *45* (17), 7027-7035.

222. Choi, J.-H.; Ye, Y.; Elabd, Y. A.; Winey, K. I., Network structure and strong microphase separation for high ion conductivity in polymerized ionic liquid block copolymers. *Macromolecules* **2013,** *46* (13), 5290-5300.

223. Takahashi, Y.; Tadokoro, H., Structural studies of polyethers, $(-(CH_2)_m-O-)_n$. X. Crystal structure of poly(ethylene oxide). *Macromolecules* **1973,** *6* (5), 672-675.

224. Wang, Y.; Travas-Sejdic, J.; Steiner, R., Polymer gel electrolyte supported with microporous polyolefin membranes for lithium ion polymer battery. *Solid State Ionics* **2002,** *148* (3–4), 443-449.

225. Zhang, S. S.; Xu, K.; Foster, D. L.; Ervin, M. H.; Jow, T. R., Microporous gel electrolyte Li-ion battery. *Journal of Power Sources* **2004,** *125* (1), 114-118.

226. Stankovich, S.; Dikin, D. A.; Dommett, G. H. B.; Kohlhaas, K. M.; Zimney, E. J.; Stach, E. A.; Piner, R. D.; Nguyen, S. T.; Ruoff, R. S., Graphene-based composite materials. *Nature* **2006,** *442* (7100), 282-286.

227. Dikin, D. A.; Stankovich, S.; Zimney, E. J.; Piner, R. D.; Dommett, G. H. B.; Evmenenko, G.; Nguyen, S. T.; Ruoff, R. S., Preparation and characterization of graphene oxide paper. *Nature* **2007,** *448* (7152), 457-460.

228. Stankovich, S.; Dikin, D. A.; Piner, R. D.; Kohlhaas, K. A.; Kleinhammes, A.; Jia, Y.; Wu, Y.; Nguyen, S. T.; Ruoff, R. S., Synthesis of graphene-based nanosheets via chemical reduction of exfoliated graphite oxide. *Carbon* **2007,** *45* (7), 1558-1565.

229. Park, S.; An, J. H.; Jung, I. W.; Piner, R. D.; An, S. J.; Li, X. S.; Velamakanni, A.; Ruoff, R. S., Colloidal suspensions of highly reduced graphene oxide in a wide variety of organic solvents. *Nano Letters* **2009,** *9* (4), 1593-1597.

230. Zhu, Y. W.; Murali, S.; Cai, W. W.; Li, X. S.; Suk, J. W.; Potts, J. R.; Ruoff, R. S., Graphene and graphene Oxide: Synthesis, properties, and applications. *Advanced Materials* **2010,** *22* (35), 3906-3924.

231. Zhu, L.; Cheng, S. Z. D.; Calhoun, B. H.; Ge, Q.; Quirk, R. P.; Thomas, E. L.; Hsiao, B. S.; Yeh, F.; Lotz, B., Crystallization temperature-dependent crystal orientations within nanoscale confined lamellae of a self-assembled crystalline−amorphous diblock copolymer. *Journal of the American Chemical Society* **2000,** *122* (25), 5957-5967.

232. Zhu, L.; Cheng, S. Z. D.; Calhoun, B. H.; Ge, Q.; Quirk, R. P.; Thomas, E. L.; Hsiao, B. S.; Yeh, F.; Lotz, B., Phase structures and morphologies determined by self-organization,

vitrification, and crystallization: confined crystallization in an ordered lamellar phase of PEO-b-PS diblock copolymer. *Polymer* **2001,** *42* (13), 5829-5839.

233. Wang, H.; Keum, J. K.; Hiltner, A.; Baer, E.; Freeman, B.; Rozanski, A.; Galeski, A., Confined crystallization of polyethylene oxide in nanolayer assemblies. *Science* **2009,** *323* (5915), 757-760.

234. Wang, H.; Keum, J. K.; Hiltner, A.; Baer, E., Impact of nanoscale confinement on crystal orientation of poly(ethylene oxide). *Macromol. Rapid Commun.* **2010,** *31* (4), 356-361.

235. Wang, H.; Keum, J. K.; Hiltner, A.; Baer, E., Confined crystallization of PEO in nanolayered films impacting structure and oxygen permeability. *Macromolecules* **2009,** *42* (18), 7055-7066.

236. Hummers, W. S.; Offerman, R. E., Preparation of graphite oxide. *J. Am. Chem. Soc.* **1958,** *80*, 1339.

237. Dreyer, D. R.; Park, S.; Bielawski, C. W.; Ruoff, R. S., The chemistry of graphene oxide. *Chemical Society Reviews* **2010,** *39* (1).

238. Chatterjee, T.; Lorenzo, A. T.; Krishnamoorti, R., Poly(ethylene oxide) crystallization in single walled carbon nanotube based nanocomposites: Kinetics and structural consequences. *Polymer* **2011,** *52* (21), 4938-4946.

239. Edman, L.; Ferry, A.; Jacobsson, P., Effect of C_{60} as a filler on the morphology of polymer−salt complexes based on poly(ethylene oxide) and $LiCF_3SO_3$. *Macromolecules* **1999,** *32* (12), 4130-4133.

240. Chatterjee, T.; Yurekli, K.; Hadjiev, V. G.; Krishnamoorti, R., Single-walled carbon nanotube dispersions in poly(ethylene oxide). *Advanced Functional Materials* **2005,** *15* (11), 1832-1838.

241. Avarami, M., *Journal of Chemical Physics* **1939,** *7*, 1103-1112.

242. Wunderlich, B., Macromolecular physics. In *Macromolecular physics*, Academic Press: New York, 1976; Vol. II, pp 132-147.

243. Keller, A., A note on single crystals in polymers: Evidence for a folded chain configuration. *Philosophical Magazine* **1957,** *2* (21), 1171-1175.

244. Bassett, D. C.; Frank, F. C.; Keller, A., Evidence for distinct sectors in polymer single crystals. *Nature* **1959,** *184* (4689), 810-811.

245. Keller, A., Polymer single crystals. *Polymer* **1962,** *3* (0), 393-421.

246. Dong, B.; Zhou, T.; Zhang, H.; Li, C. Y., Directed self-assembly of nanoparticles for nanomotors. *ACS Nano* **2013,** *7* (6), 5192-5198.

247. Dong, B.; Wang, W.; Miller, D. L.; Li, C. Y., Polymer-single-crystal@ nanoparticle nanosandwich for surface enhanced Raman spectroscopy. *J. Mater. Chem.* **2012,** *22* (31), 15526-15529.

248. Dong, B.; Miller, D. L.; Li, C. Y., Polymer single crystal as magnetically recoverable support for nanocatalysts. *The Journal of Physical Chemistry Letters* **2012,** *3* (10), 1346-1350.

249. Zhou, T.; Dong, B.; Qi, H.; Lau, H. K.; Li, C. Y., One-step formation of responsive "dumbbell" nanoparticle dimers via quasi-two-dimensional polymer single crystals. *Nanoscale* **2014,** *6* (9), 4551-4554.

250. Lotz, B.; Kovacs, A. J.; Bassett, G. A.; Keller, A., Properties of copolymers composed of one poly-ethylene-oxide and one polystyrene block. *Kolloid-Z.u.Z.Polymere* **1966,** *209* (2), 115-128.

251. Tadokoro, H.; Chatani, Y.; Yoshihara, T.; Tahara, S.; Murahashi, S., Structural studies on polyethers, $[-(CH_2)_m-O-]_n$. II. Molecular structure of polyethylene oxide. *Die Makromolekulare Chemie* **1964,** *73* (1), 109-127.

252. Cable, K. M.; Maurtiz, K. A.; Moore, R. B., Anisotropic ionic conductivity in uniaxially oriented perfluorosulfonate ionomers. *Chemistry of Materials* **1995,** *7* (9), 1601-1603.

253. Elabd, Y. A.; Walker, C. W.; Beyer, F. L., Triblock copolymer ionomer membranes Part II. Structure characterization and its effects on transport properties and direct methanol fuel cell performance. *J. Membr. Sci.* **2004,** *231* (1-2), 181-188.

254. Young, W.-S.; Epps, T. H., Ionic conductivities of block copolymer electrolytes with various conducting pathways: Sample preparation and processing considerations. *Macromolecules* **2012,** *45* (11), 4689-4697.

255. Watanabe, M.; Nagano, S.; Sanui, K.; Ogata, N., Ionic conductivity of network polymers from poly(ethylene oxide) containing lithium perchlorate. *Polymer Journal* **1986,** *18* (11), 809-817.

256. Armand, M.; Gorecki, W.; Andréani, R. Second Internal Symp. on Polymer Electrolytes, New York, Scrosati, B., Ed. Elsevier Applied Science: New York, 1990; p 91.

257. Labrèche, C.; Lévesque, I.; Prud'homme, J., An appraisal of tetraethylsulfamide as plasticizer for poly(ethylene oxide)−$LiN(CF_3SO_2)_2$ rubbery electrolytes. *Macromolecules* **1996,** *29* (24), 7795-7801.

258. Perrier, M.; Besner, S.; Paquette, C.; Vallée, A.; Lascaud, S.; Prud'homme, J., Mixed-alkali effect and short-range interactions in amorphous poly(ethylene oxide) electrolytes. *Electrochimica Acta* **1995,** *40* (13–14), 2123-2129.

259. Cheng, S.; Smith, D. M.; Li, C. Y., How does nanoscale crystalline structure affect ion transport in solid polymer electrolytes? *Macromolecules* **2014,** *47* (12), 3978-3986.

260. Edman, L., Ion association and ion solvation effects at the crystalline−amorphous phase transition in PEO−LiTFSI. *The Journal of Physical Chemistry B* **2000,** *104* (31), 7254-7258.

261. Carvalho, L. M.; Guégan, P.; Cheradame, H.; Gomes, A. S., Variation of the mesh size of PEO-based networks filled with TFSILi: from an Arrhenius to WLF type conductivity behavior. *European Polymer Journal* **2000,** *36* (2), 401-409.

262. Fauteux, D., Formation of a passivating film at the lithium-PEO-$LiCF_3SO_3$ interface. *Solid State Ionics* **1985,** *17* (2), 133-138.

263. Appetecchi, G. B.; Dautzenberg, G.; Scrosati, B., A new class of advanced polymer electrolytes and their relevance in plastic-like, rechargeable lithium batteries. *Journal of The Electrochemical Society* **1996,** *143* (1), 6-12.

264. Edman, L.; Doeff, M. M.; Ferry, A.; Kerr, J.; De Jonghe, L. C., Transport properties of the solid polymer electrolyte system P(EO)nLiTFSI. *The Journal of Physical Chemistry B* **2000,** *104* (15), 3476-3480.

265. Nielsen, L. E., Models for the permeability of filled polymer systems. *Journal of Macromolecular Science: Part A - Chemistry* **1967,** *1* (5), 929-942.

266. Bharadwaj, R. K., Modeling the barrier properties of polymer-layered silicate nanocomposites. *Macromolecules* **2001,** *34* (26), 9189-9192.

267. Xu, B.; Zheng, Q.; Song, Y.; Shangguan, Y., Calculating barrier properties of polymer/clay nanocomposites: Effects of clay layers. *Polymer* **2006,** *47* (8), 2904-2910.

268. Bruce, P. G.; Vincent, C. A., Polymer electrolytes. *Journal of the Chemical Society, Faraday Transactions* **1993,** *89* (17), 3187-3203.

269. Landauer, R., Electrical resistance of binary metallic mixtures. *Journal of Applied Physics* **1952,** *23* (7), 779-784.

270. Davis, H. T., The effective medium theory of diffusion in composite media. *J. Am. Cer. Soc.* **1977,** *60* (11-12), 499-501.

271. Ramon-Gimenez, L.; Storz, R.; Haberl, J.; Finkelmann, H.; Hoffmann, A., Anisotropic ionic mobility of lithium salts in lamellar liquid crystalline polymer networks. *Macromol. Rapid Commun.* **2012,** *33* (5), 386-391.

Appendix: Frequently Used Abbreviations and Nomenclatures

PEO	Polyethylene oxide
GO	Graphene oxide
SPE	Solid polymer electrolyte
PSC	Polymer single crystal
TFSI	bis(trifluoromethylsulfonyl) imide
$<r>$	Normalized molar ratio of Li^+ to ethylene oxide unit
$\sigma_{//}$	In-plane ionic conductivity
$\sigma_{\perp}$	Through-plane ionic conductivity
$\sigma_{//}/\sigma_{\perp}$	Conductivity anisotropy
σ_0	Ionic conductivity of 100% amorphous SPE

Vita

Shan Cheng was born in Hanzhong, Shaanxi China in 1987. She received her Bachelor's degree in Polymer Science and Engineering in Jilin University, Changchun, China in 2009. With a strong interest in the structure-property relations of polymeric materials, she started the Ph.D. program in Materials Science and Engineering at Drexel University, Philadelphia PA in September, 2009. She's been involved in multiple projects in graduate school for the first three years and decided to focus on the research of solid polymer electrolyte for energy related applications as her dissertation topic. She is currently working at BD Diagnostics-Preanalytical Systems in Franklin Lakes, NJ as a Sr. Materials Scientist.

PROFESSIONAL MEMBERSHIPS:

- American Physical Society (APS)
- North American Thermal Analysis Society (NATAS)

HONORS AND AWARDS:

- Harry Brown Fellowship, Drexel University, **2013**
- Outstanding Thesis Award, Jilin University, **2009**

SELECTED PUBLICATIONS:

- **Cheng, S.**; Smith, D. M.; Li, C.Y. How Does Nanoscale Crystalline Structure Affect Ion Conductivity in Solid Polymer Electrolyte? *Macromolecules* **2014**, 47, 3978-3986.
- **Cheng, S.**; Cairncross, R.; Hsuan, Y. G.; Li, C. Y. Correlation between Clay Orientation and Thermo Stability of PE-Clay Nanocomposites, *Polymer,* **2013**, 54 (18), 5016-5023.
- **Cheng, S.**; Chen, X.; Hsuan, Y. G.; Li, C. Y. Reduced Graphene Oxide-Induced Polyethylene Crystallization in Solution and Nanocomposites. *Macromolecules*, **2012**, 45 (2), 993-1000.